A Systems Biology Approach to Modeling Signaling Crosstalk in Cell Fate Decisions

By

Geena Victoria Ildefonso

Dissertation

Submitted to the Faculty of the

Graduate School of Vanderbilt University

in partial fulfillment of the requirements

for the degree of

DOCTOR OF PHILOSOPHY

in

Chemical and Physical Biology

May 13, 2022

Nashville, Tennessee

Approved:

Vito Quaranta, Ph.D.

Leonard Harris, Ph.D.

Jacob Hughey, Ph.D.

Jeffrey Rathmell, Ph.D.

Julie Rhoades, Ph.D.

Marija Zanic, Ph.D.

DEDICATION

To Papi, Bebí, Mima, Melaine, Michelle, and everyone who is no longer with us. You will always be loved and missed.

ACKNOWLEDGEMENTS

The work presented in this dissertation was made possible by the financial support of the Initiative for Maximizing Student Diversity (IMSD) program, the Molecular Physiology and Biophysics Training Grant Program (MBTP), and the National Science Foundation Graduate Research Fellowship (NSFGRFP).

I am so grateful and humbled by the fact that I am the first in my family to have pursued a doctoral degree. There is not enough space here to truly thank everyone who has impacted my life and supported me through this entire journey to get to where I am today. I would like to first thank Michelle Harding, the first woman of color I had the pleasure of learning mathematics from in high school. Michelle saw something in me before I knew who I was, and her excitement and love for mathematics had such an impact on me, I chose to study mathematics in college at the University of Central Florida (UCF). In college, several mentors contributed significantly to my career trajectory. Dr. Shivamoggi approached me about conducting research in his lab, I remember having no idea what he was talking about and had never heard of “research” before. He walked me to the research office and told me “we were going to get some funding” so I could get paid to do research. This is where I met the three most remarkable people on the road to my PhD. Since I did not know what research was, I also did not know what a “PhD” was. There are not enough words to express my appreciation to Michael Aldarondo-Jeffries, Natalia Toro, and Arlene Ollivierre for giving me the opportunity to become a McNair Scholar and conduct research for the first time. They told me I was going to get paid, it seemed too good to be true. With their guidance and support, I started conducting research, and was introduced to Dr. Don Brunson at Vanderbilt University. Thank you,

Dr. Brunson for coming to visit UCF, and connecting me with Dr. Carlos Lopez. I remember a distinct phone call from Carlos, asking me how much I knew about biology. I had never taken a biology course before. He was convinced because I was from Miami where he got his PhD, that I could learn biology, and that was my first opportunity to conduct research at the interface of mathematics and biology. I was fascinated. Thank you for taking a chance on me and supporting me on my journey through my PhD. My dad was diagnosed with cancer when I first started college, and I remember not understanding what the doctors were saying and being very frustrated. My summer at Vanderbilt opened my eyes to see how I could be a part of research that was so impactful. Michael and Natalia ultimately convinced me that I should apply to graduate school. I am forever grateful for all the time I spent sitting in their offices laughing and crying through college, I would not be where I am today without them.

I would like to thank my mentor, Vito Quaranta for providing such a supportive environment in which students can freely pursue their ideas and projects. You have consistently advocated for me and provided an environment in which students can freely pursue ideas and projects. Your support and mentoring allowed me to become the scientist I am today. I am also eternally grateful to Bruce Damon and Patty Mueller for always advocating for and supporting us students. I want to thank the members of my thesis committee: Dr. Jeffrey Rathmell, Dr. Leonard Harris, Dr, Marija Zanic, Dr. Julie Rhoades, and Dr. Jacob Hughey. Thank you for challenging me to become the scientist I am today, and for all your feedback and guidance throughout my graduate career. I sincerely enjoyed the opportunity to work with peer scientists from the Quaranta and Lopez labs, I am grateful for your support and feedback. I would like to specifically thank

Leonard Harris, who served as my secondary mentor and friend. Thank you for the innumerable amount of support and personal time you gave to help me cross the finish line. Your unwavering guidance and encouragement truly knows no bounds. Thank you for helping me become the scientist I am today, and always advocating for students. To James Pino, Michael Irvin, Sam Beik, Oscar Ortega, Alex Lubbock, thank you for always taking the time to answer my questions and work out challenges I faced with my work, it has been an honor to work beside you all. To Corey Hayford, thank you for being an amazing friend and lab mate, you made graduate school way more enjoyable and memorable. To Sarah Maddox Groves, thank you for being the ultimate work life bestie combo, through our snacking and trauma bonding, coffee shopping, and being such a supportive friend and lab mate. GS&C forever. To Michelle Scott, you will always be missed, and the work you started will always continue. To my dear beautiful Melaine Sebastian, not a day goes by that I don't think of you, I am honored to have continued the work that you started, you are missed so much. To the other lab members and mentees, I am so appreciative for your knowledge and friendship.

Thank you to the amazing administrators of Vanderbilt University in the BRET office, in particular Beth Bowman and Carolyn Berry for guiding me through my first two years of graduate school and a constant support system. I ultimately chose Vanderbilt for my graduate career because of the IMSD program. I would like to thank Christina Keeton, Linda Sealy, and Roger Chalkley. To Roger and Linda, thank you for being constant advocates for minorities in STEM and always being supportive of my goals. Many of my peers in the IMSD program would not have made it to the end of their PhD without your unwavering support and guidance. To Christina Keeton, I want to thank you for going

beyond an administrator as an advisor, mentor, and friend. Thank you for always being there throughout my graduate career. You have helped me through the many challenges of graduate school, and I will be forever grateful to you. To the rest of the IMSD family that I met in graduate school, thank you. We all came from different walks of life with a common goal in becoming scientists and leave our impact on the world.

Last but not least, my graduate school experience would not have been possible without the love and support from my family, friends, and expresso from Starbucks. To Kelsey Pilewski, thank you for being the best random roommate our first year, for always having the face masks and prosecco ready on those rainy days and watching new girl for the 500th time. To Slavi Goleva, my Irish Bulgarian, thank you for our long late-night convos in the car, and being my curly girl. To Lindsay Redman-Rivera, thank you for always making sure I took care of myself, and making sure I ate when I often forgot to, I will always be grateful for our friendship. To Kellie Williford, my Beyonce dance partner, thank you for always brightening my day with your infectious smile, and singing at the top of our lungs in the car. To my best friend from high school, Danielle Hoffman, my blondie, we endured graduate school together at different universities, thank you for trauma bonding with me from hundreds of miles away the last five years and for all of your love and support. Cheers to being Doctors. To my best friend from college, Jessica Bouters, my jelly, my bandmate, my Zumba partner, thank you for our random TikToking, supporting me always, and for being there for all of the big moments in my life including my defense, it means the world to me. To Nick White, thank you for being my brother from another mother. We have persevered in grad school thousands of miles apart, and always having your support and long phone calls has lifted my spirits on the hardest days.

I am still sorry not sorry for bringing you on the expresso addiction train, you always had 10 books. To Katie Khuu, our friendship has meant the world to me since we first sat down to play spades that summer. Thank you for always being there and supporting me. Thank you to my friends, both old and new, who I leaned on heavily during challenging times. Thank you to my titis, tíos, and primis for always checking in on me and supporting me in the most meaningful ways. To my mom, thank you for always believing in me even when I did not believe in myself. You always knew I would make it, even when you had no idea what I was doing. To my dad, my angel, I wish you were here in person to watch me become a Doctor, I know you are watching over me from heaven. Thank you for loving me unconditionally and always being my cheerleader as daddy's girl. Thank you to my dog Kemi for spending many late nights under my desk while I worked. And to my life partner, Tolu, there will never be enough words to describe how grateful I am for your unconditional love and support over the last five years. Thank you for always taking me to get ice cream late at night when I needed a pick me up and hiding emergency chocolate in the house for the really tough times. I love you, cheers to being Doctors.

Embrace his legacy and create your own- Ronald E. McNair
It takes a village.

TABLE OF CONTENTS

LIST OF FIGURES

LIST OF TABLES

LIST OF ABBREVIATIONS

A20	Tumor necrosis factor alpha-induced protein 3
ACSL1	achaete-scute homologue 1
ADAM10	ADAM Metallopeptidase Domain 10
C8i	Caspase 8 (inactive)
C8a	Caspase 8 (active)
C8:FLIP	Caspase 8(active):FLIP
CHX	Cycloheximide
cIAP1	Cellular inhibitor of apoptosis protein 1
cIAP2	Cellular inhibitor of apoptosis protein 2
CI	Complex I
CII	Complex II
CR	Cell Rank
CYLD	cylindromatosis
DKO	Double knockout
DLL1	Delta-like Ligand 1
DLL3	Delta-like Ligand 3
DLL4	Delta-like Ligand 4
FADD	FAS-associated death domain protein
FLIP	FLICE-like inhibitory protein
γSec	gamma-secretase
GEMM	Genetically Engineered Mouse Model
GFP	Green Fluorescent Protein
HCAC	human cervical adenocarcinoma
HCN	hippocampal neurons
HEK	human embryonic kidney
HES1	Hes Family BHLH Transcription Factor 1
HES6	Hes Family BHLH Transcription Factor 6
JAG1	Jagged1
JAG2	Jagged2

KD	Knockdown
KO	Knockout
LUBAC	linear ubiquitin chain assembly complex
MAML	mastermind-like 1
MEF	mouse embryonic fibroblast
MFS	mouse fibrosarcoma
MLKL	Mixed Lineage Kinase Domain Like-Pseudokinase
MLKLp	Mixed Lineage Kinase Domain Like-Pseudokinase (phosphorylate)
MYC	Myelocytomatosis Proto-Oncogene, BHLH Transcription Factor
MYCL	Myelocytomatosis Proto-Oncogene, BHLH Transcription Factor L
NE	Neuroendocrine
NEURDO1	neurogenic differentiation factor 1
NEUROG3	Neurogenin 3
NICD1	Notch Intracellular Domain 1
NICD2	Notch Intracellular Domain 2
NICD3	Notch Intracellular Domain 3
NICD4	Notch Intracellular Domain 4
Non-NE	Non-Neuroendocrine
NOTCH1	Notch Receptor 1
NOTCH2	Notch Receptor 2
NOTCH3	Notch Receptor 3
NOTCH4	Notch Receptor 4
OE	Overexpression
PCD	Programmed Cell Death
PNECs	Pulmonary Neuroendocrine Cells
POU2F3	POU class 2 homeobox 3
PyDyNo	Python Dynamical Network Analysis
PySB	Python Systems Biology
RBPJ	Recombination Signal Binding Protein For Immunoglobulin Kappa J Region
REST	RE1 Silencing Transcription Factor

RIP1	Receptor Interacting Protein 1
RIP1Ub	Receptor Interacting Protein 1 (ubiquitinated)
RIP1dUb	Receptor Interacting Protein 1 (deubiquitinated)
RIP1p	Receptor Interacting Protein 1 (phosphorylated)
RIP3	Receptor Interacting Protein 3
RIP3p	Receptor Interacting Protein 3 (phosphorylated)
RPM	$p53^{fl/fl}$;$Rb^{fl/fl}$; Lox-Stop-Lox [LSL]-Myc^{T58A}
RPR2	$p53^{fl/fl}$;$Rb^{fl/fl}$;$Rbl2^{fl/fl}$
SCLC	Small Cell Lung Cancer
SCLC-A	Small Cell Lung Cancer- achaete-scute homologue 1
SCLC-N	Small Cell Lung Cancer- neurogenic differentiation factor 1
SCLC-P	Small Cell Lung Cancer-POU class 2 homeobox 3
SCLC-Y	Small Cell Lung Cancer-yes-associated protein 1
scVelo	Single-Cell RNA Velocity
TF	Transcription Factor
TNF	Tumor Necrosis Factor
TNFR1	Tumor Necrosis Factor Receptor 1
TRADD	TNFRSF1A Associated Via Death Domain
TRAF2	Tumor Necrosis Factor Receptor Associated Factor 2
TTD	Time-To-Death
YAP1	yes-associated protein 1
WCM	whole-cell modeling
WT	Wild Type

CHAPTER I

I. INTRODUCTION

A systems biology approach to understanding biological systems

Organisms are made up of diverse elements (genes, proteins, and metabolites) that are controlled by a complex network of interactions. These individual living systems are able to react to stimuli, grow, develop, and reproduce over time (Stelling et al., 2004). Signal transduction in biological pathways or networks that associate different factors of living systems are not stationary, rather, they are continuously evolving to adapt to internal and environmental changes over time. The traditional perspective (reductionist approach) on biological systems has addressed the study of living organisms by focusing on isolated components instead of the complex system as a whole (Tavassoly et al., 2018). This consists of breaking a large system into different parts and identifying the connections between these them, with the assumption that molecular structures and their interactions provide enough explanation to understand the whole system (Jensen, 1998; Mayer et al., 2012). These approaches have successfully identified and characterized biological systems and the availability of such multiscale information has catalyzed the formation of systems biology.

Systems biology is an integrative holistic approach that connects the molecular components within a single biological scale and among different scales using a range of experimental and computational methodologies to decode information flow from genes, proteins, and other subcellular components of signaling, to control function (Aldridge et al., 2006; Ashyraliyev et al., 2009; Chen et al., 2010). A systems level understanding of

a biological system can be understood using four key properties: i) Systems structures, which include the networks of interactions and mechanisms in biochemical pathways, ii) System dynamics, the changes of a system's behavior over time using dynamical analysis methods, iii) The control method, including mechanisms used to control cell state that can be modulated to provide potential targets for treatments, and iv) The design method, approaches used to design and construct biological systems (Kitano, 2002). The tools used in systems biology lead to discoveries at various scales of biological organization. Systems biology forms a cyclic process of: i) Experimental design, leading to new insights and questions in biology that are processed using, ii) Technologies, that generate data used to formulate conceptual ideas and models, and iii) Computation, through mathematical formalisms to build mechanistic understanding with new biological insights and hypotheses that drive back to new biological questions and experimental designs (Figure 1). These discoveries are basic building blocks for future advances in medicine, with promise of leading to precision and individualization of treatment.

Top-down and *Bottom*-up approaches to studying multiscale systems

Historically, systems biology has focused on studying cells, tissues, and organ systems as complex biological systems (Jensen, 1998). The rapid development of -omics and sequencing technologies has led to the uncovering of big datasets of basic components that form these complex systems (Ideker et al., 2001; Lander et al., 2001). In comparison, one way to think of systems biology is to understand the broader perspective of physiology. Physiology describes functions in cells, tissues and organ systems using largely phenomenological approaches (to describe, understand, and interpret the meanings of a particular study), while systems biology integrates molecular

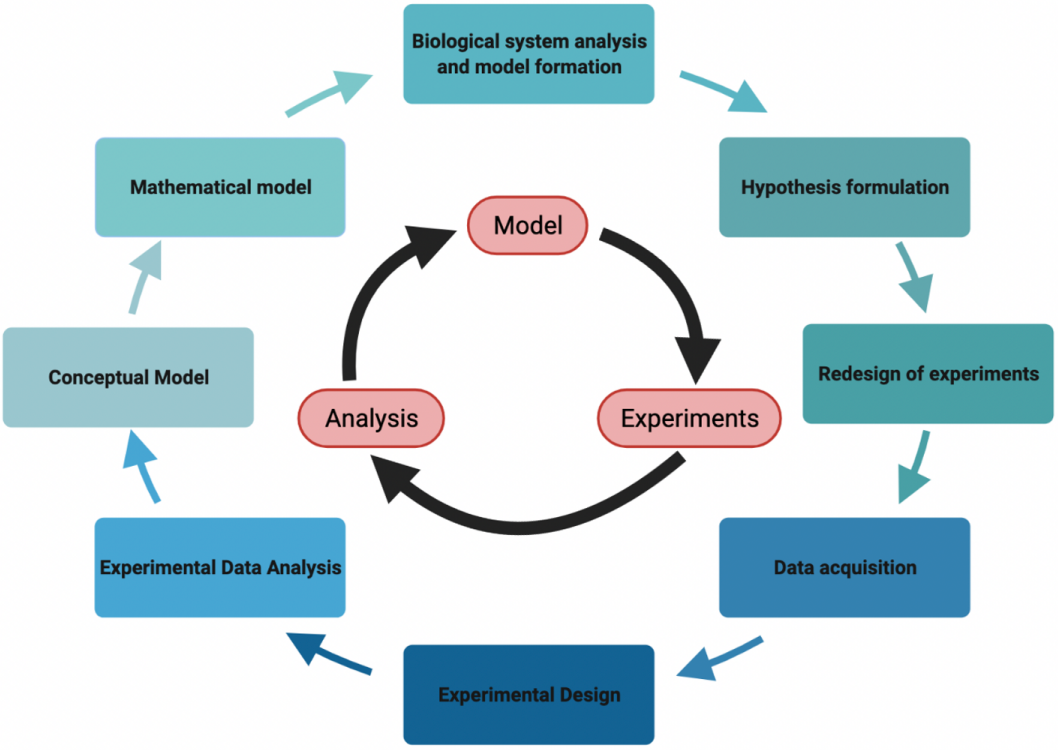

Figure 1: Systems biology approach to understanding biological systems. Workflow of systems biology approach, from experimental design and analysis, mathematical modeling and analysis, and hypothesis formation and future experimental studies.

biology, and biochemistry of molecular components, interactions, and their dynamics to understand how physiological functions arise and are controlled (Tavassoly et al., 2018).

Data integration is core to systems biology, treating the multiple components of interactions as a single system. This integration can be applied at a single scale (i.e. the cellular level) to provide new systems-level insights, but can also be used to decode complex phenotypes at different scales. For example, systems biology can be used to study the evolution of cells and cell survival from a normal cell that becomes cancerous. This involves interactions among molecular components at the cellular level. At the same time, systems biology can be used to integrate the interactions among cells that can develop into tumors. In this systems-level view, as the organizational level of a system increases, new characteristics and capabilities arise (Iyengar et al., 2012; Kitano, 2002). These multiscale systems can be studied using two main approaches: *Bottom-up* and *Top-down*, both with their respective advantages and disadvantages (Figure 2).

Top-down systems biology is an approach to characterize cellular interactions using global data collected from -omics experiments in combination with modeling (Carrera and Covert, 2015; Karr et al., 2015). These models are often phenomenological and serve to discover new insights into the molecular network being studied. This provides a “big picture” of the system, which can be comprehensive and integrative. Interactions among different elements are often defined by correlation and the complexity of these biological systems does not always allow one to make causal (underlying) inferences (Bruggeman and Westerhoff, 2007). Alternatively, *Bottom-up* systems biology does not start with collection of data, but with a detailed model of a molecular network built based on its molecular properties (Carrera and Covert, 2015; Karr et al., 2015). This

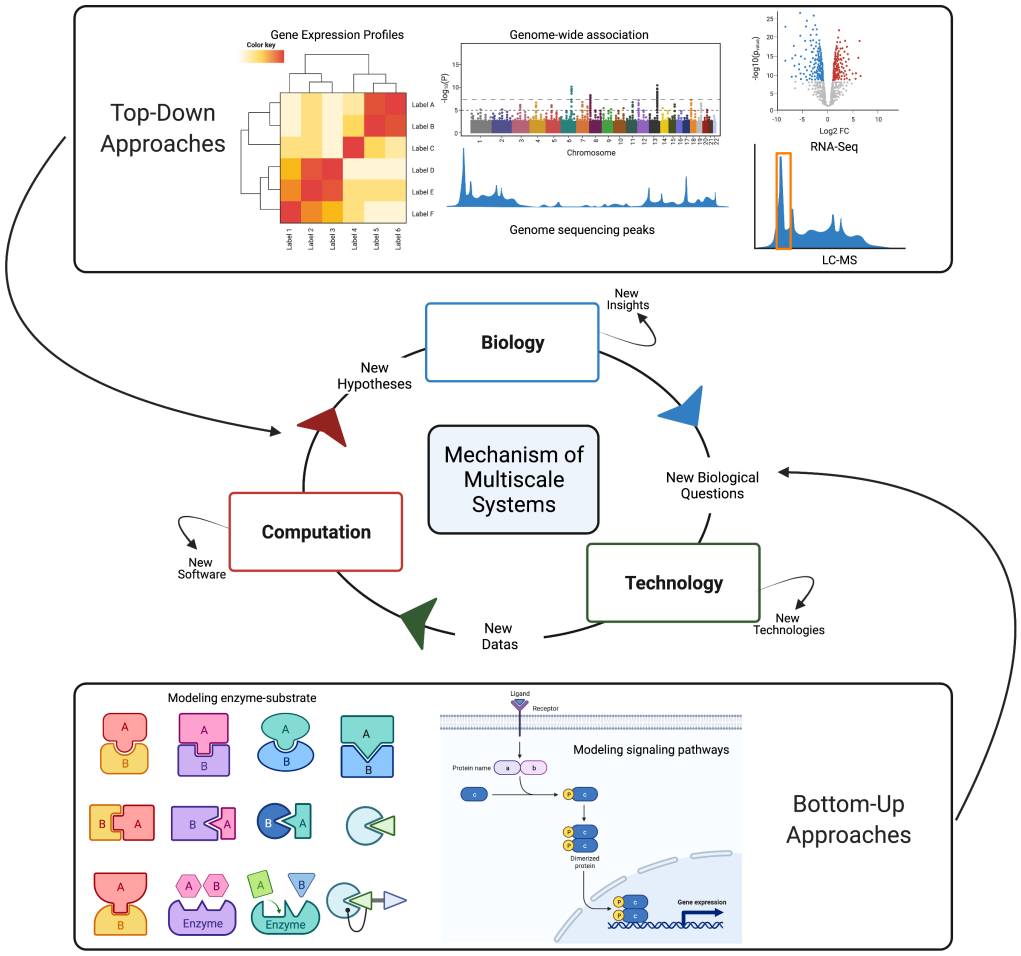

Figure 2: Top-down and Bottom-up approach to systems biology. Methods used in Top-down and Bottom-up approaches connecting to the cyclic process of understanding mechanisms of multiscale systems within systems biology.

approach can provide mechanistic insights into how different elements work together to form a system.

These molecular networks can be quantitatively studied leading to predictive models that can be used to identify potential targets for further investigation and intervention. These approaches have been integrated to further research and knowledge achieved by the synergistic use of models and experimental data. In addition, this complexity motivates the necessity towards comprehensive models of cells that can represent all aspects of cell biology, reflecting the dynamic and multiscale information and systems understanding such as gene networks, metabolic networks, and protein signaling networks, more commonly known as whole-cell modeling (Singla and White, 2021).

Whole-cell modeling approach to studying multiscale systems

An integrative approach to modeling that combines diverse mathematical and computational tools and methods can enable the simultaneous inclusion of fundamentally different cellular processes and experimental measurements. Understanding how complex phenotypes arise from individual molecules and their interactions is a primary challenge in biology that these approaches are primed to tackle. Utilizing both *Top-down* and *Bottom-up* approaches and integrating multiscale axes of data integration, we progress towards whole-cell modeling, to integrate the different subdisciplines of biology to generate more accurate, complete models of cells (Figure 3). Whole-cell modeling efforts will provide new opportunities for investigating how different cellular systems work together, how they are dysregulated in cancer and diseases, and will provide a path for generating and testing new hypotheses for drugs and therapeutic targets. The first whole-

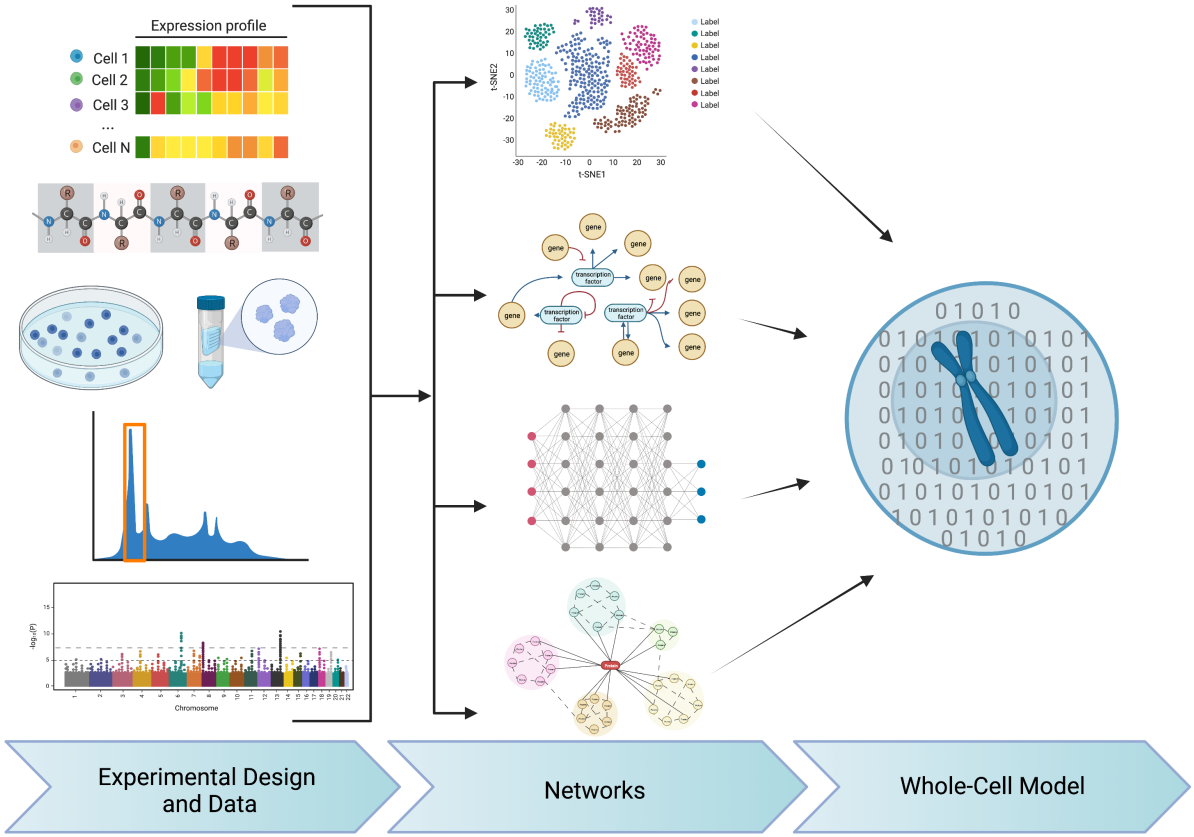

Figure 3: Process of whole-cell modeling. Schematic workflow to whole-cell modeling, including the experimental design and collection of data, building associated networks from experimental data, combined to incorporate into a whole-cell model.

cell model (Karr et al., 2018) was developed to study the life cycle of human pathogen *Mycoplasma genitalium*, which was considered a “first draft” for whole-cell modeling work. The goal of their work was to develop this comprehensive model in a reduced system before proceeding to more complex organisms. However, there were great limitations in the range of experimental techniques available to study this organism, and as a result, much of the data used to build and validate the model was obtained from other organisms (Karr et al., 2015; Singla and White, 2021).

So why build whole-cell models? Whole-cell modeling integrates heterogenous datasets (both quantitative and qualitative), aids to identify gaps in knowledge which can drive hypothesis predictions that can further experimental design to predict complex phenotypes. This ultimately serves as a foundational platform for interpreting complex behaviors and facilitate discovery across a multitude of medial, research and biotechnological applications (Carrera and Covert, 2015). The holy grail of whole-cell modeling is to develop a whole cell model of human cells, detailing the multiscale levels across metabolites, genes, and proteins, all the way up to the complex phenotypes. Personalized medicine is the future direction of healthcare and systems biology serves as the enabling force (Figure 4). Bridging the gap between experimental studies and computational tools and technologies through whole-cell modeling will be the driving force to achieve these goals (Alyass et al., 2015; Chen and Snyder, 2012). One barrier to overcome is connecting numerous signaling pathways that are known to be interrelated through signaling crosstalk, yet the complexity of the underlying biochemistry has made it difficult to explain through experimental studies alone (Aldridge et al., 2006; Chen et al., 2010; Kolczyk and Conradi, 2016).

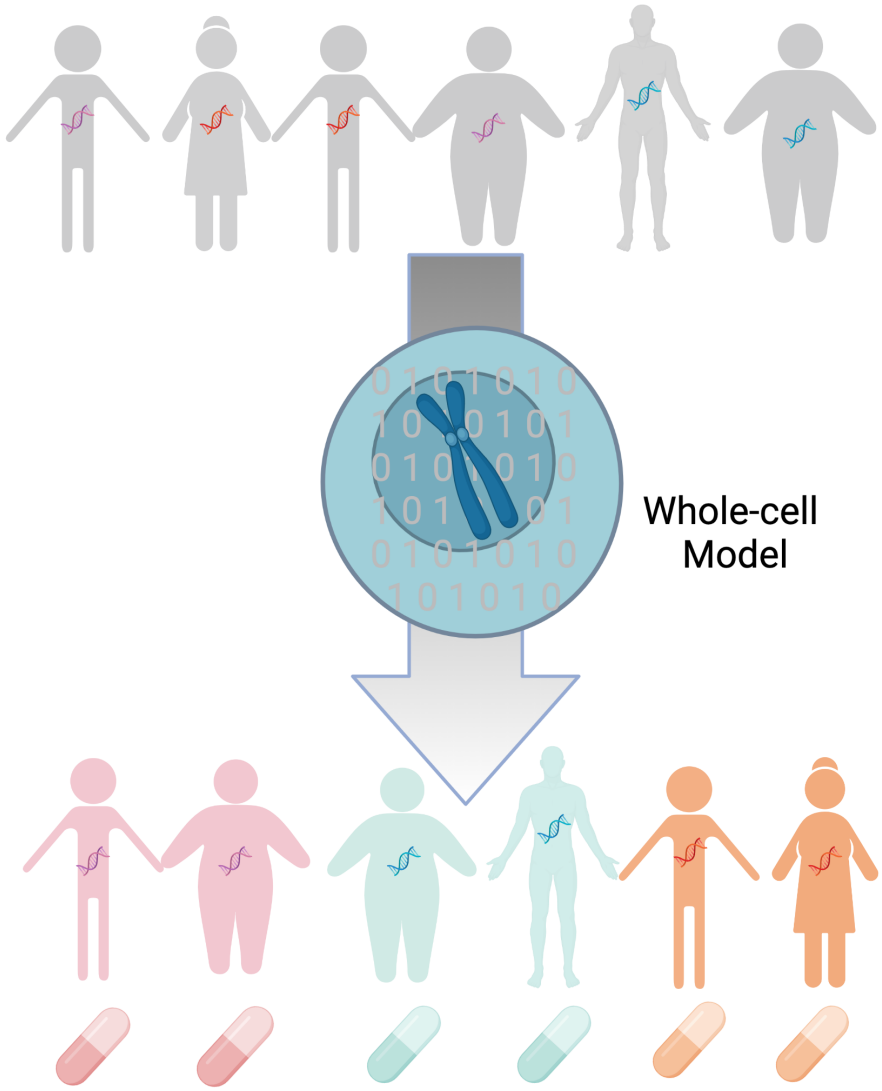

Figure 4: Towards precision medicine with whole-cell modeling. The fundamental goal of whole-cell modeling, to identify and characterize expression profiles in humans, using whole-cell modeling to individualize treatment.

Summary and Study Aims

As the field of systems biology progresses towards whole-cell modeling, and we develop new technologies and computational tools for studying biological systems, our current understanding of the cellular and molecular mechanisms that regulate cell fate decisions will expand. There has been a lot of progress building and encoding individual models of cell fate decisions in human cells including, but not limited to, cell death by apoptosis (Albeck et al., 2008), cell survival by NF-*kappa*B (Kearns et al., 2006; Metzig et al., 2020; Nelson et al., 2004), angiogenesis (Rohrs et al., 2020; Song and Finley, 2020), and pathogenesis (Mortlock et al., 2021). To address this, we take a systems biology approach to study two model systems, integrating both *Top-down* and *Bottom-up* approaches towards the whole-cell modeling effort, to build and encode two models that are both fundamental to cancer and disease: programmed cell death pathway, necroptosis (Cho, 2018; Molnár et al., 2019), and the Notch signaling pathway (Allen and Maillard, 2021; Aster et al., 2017).

While it is well established that necroptosis and Notch signaling regulates a plethora of biological processes that affect cancer and disease, studies have also shown both pathways to execute cell fate decisions in a context-dependent manner. In necroptosis, it is well known that a core axis of modulators, RIP1-RIP3-MLKL are central to necroptosis. However, even when cells express these core mediators, there is substantial variability in their ability to under-go MLKL-mediated cell death. This is likely related to the plethora of modulators that tune signaling along the core necro-ptotic axis, and the mechanisms explaining this variability remain unclear. Moreover, the role of Notch signaling in SCLC is more complex due to the cell-cell communication and diversity

of four ligands and receptors that is hypothesized to execute in a context-dependent manner.

In Chapter II, we characterize context-dependent mechanisms of necroptosis signaling through a bottom-up mechanistic development of the first biochemical necroptosis model and identify distinct execution modes to explain cell-type specific responses and variability in TTD. We also establish roles for CYLD and A20 response differentially driven within each mode to regulate RIP1 ubiquitination towards time to cell death execution. In Chapter III, we explore the role of the Notch signaling pathway using bulk and single-cell data from SCLC human tumors and cell lines to investigate the differential expression of Notch ligands, receptors, and downstream targets across SCLC subtypes. We use a top-down data integration approach to further our development of our mechanistic model of Notch in SCLC. Chapter IV describes the materials and research methods used in the studies in Chapters II and III. Finally, Chapter V discusses the overall conclusions and future implications of this work.

CHAPTER II

II. DISTINCT EXECUTION MODES OF A BIOCHEMICAL NECROPTOSIS MODEL EXPLAIN CELL TYPE-SPECIFIC RESPONSES AND VARIABILITY TO CELL-DEATH CUES

The work presented in this chapter is published and adapted from (Ildefonso et al., 2022): Geena V Ildefonso, Marie Oliver Metzig, Alexander Hoffmann, Leonard A Harris, Carlos F Lopez. Distinct execution modes of a biochemical necroptosis model explain cell type-specific responses and variability to cell-death cues. bioRxiv 2022. https://doi.org/10.1101/2022.02.25.481705.

INTRODUCTION

Understanding cellular response in cell death and disease

Cells respond to stress in a variety of ways, ranging from activation of pathways promoting cell survival to eliciting programmed cell death (PCD; Vanden Berghe et al., 2015; Nikoletopoulou et al., 2013; Sevimoglu and Arga, 2014). Cell death is a crucial process in cellular homeostasis, with over 100 billion cells dying in the human body by different cell death pathways each day (Belizário et al., 2015). Apoptosis has been widely recognized as the primary form of programmed cell death, characterized by the dismantling of the cell into apoptotic bodies that can be easily processed by the immune system (Vanden Berghe et al., 2015). Conversely, necroptosis is an alternative form of programmed cell death in which the cell membrane is ruptured, leading to immune response activation (Aldridge et al., 2009; Degterev et al., 2005). Various human diseases, including neurodegenerative disorders, cardiovascular diseases, infections, and cancer (Figure 5), have been associated with necroptosis (Vanlangenakker et al., 2012). Induction of necroptosis is also currently being explored as an alternative anti-

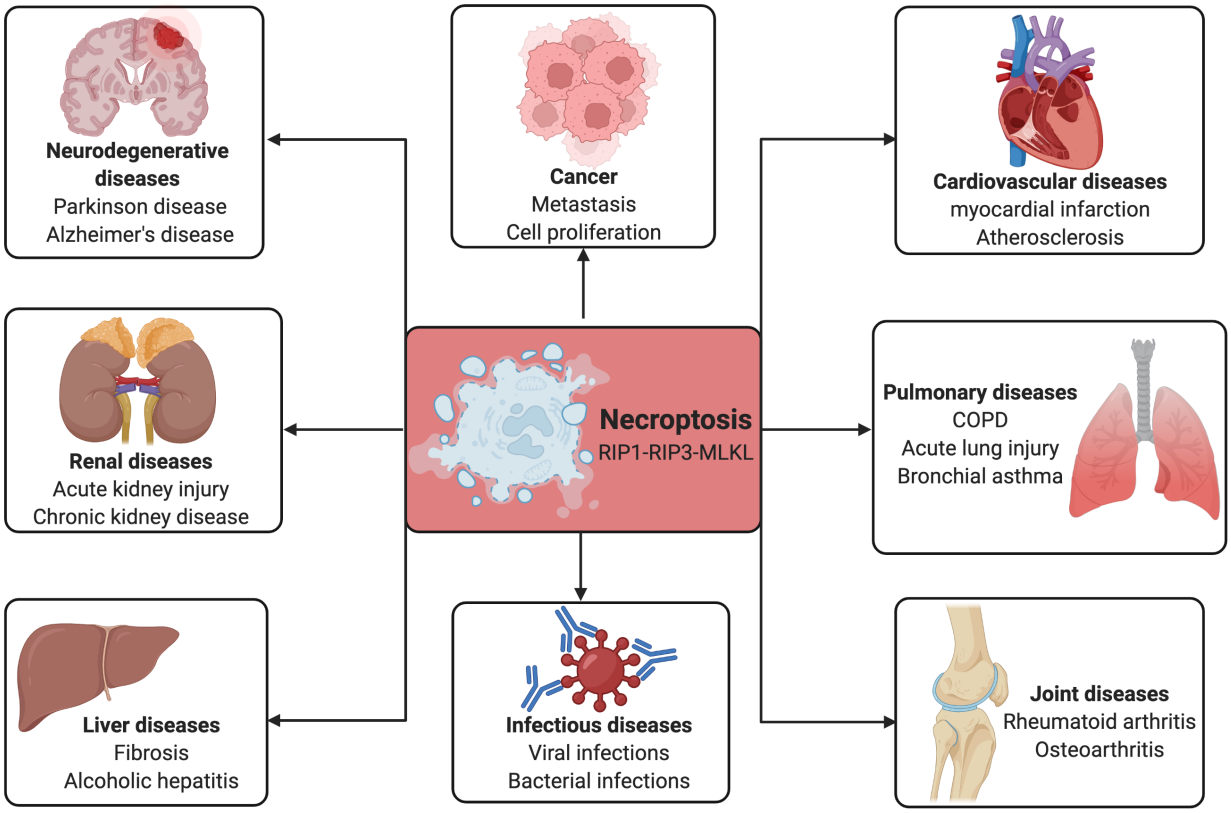

Figure 5: Importance of necroptosis in health and disease. Necroptosis is involved in a verity of diseases, including neurodegenerative diseases, renal diseases, liver diseases, cancers, infections, cardiovascular diseases, pulmonary diseases, and joint diseases.

cancer therapy, since apoptosis resistance is a hallmark of cancer (Hanahan and Weinberg, 2000, 2011).

The identification of crucial signaling and execution molecules, which are highly regulated, revealed that necroptosis encompasses several cell death modalities that can be therapeutically targeted (Basak and Hoffmann, 2008). The discovery of necroptosis has overturned the traditional belief that necrosis is a passive process caused by overwhelming stress and demonstrated that targeting necroptosis for treatment of human disease, such as neurodegenerative diseases and cancer is a promising avenue (Vanlangenakker et al., 2012). Additionally, in the case of apoptotic resistant cells, necroptosis has been seen as a potential "back up" form of cell death. Many questions concerning the crosstalk among the cell death regulators, their intracellular pathways, and the immunological consequences remain unanswered. Triggering necroptosis is also being considered as a potential anticancer treatment (Nikoletopoulou et al., 2013; Shih et al., 2017). Therefore, a mechanistic understanding of necroptosis execution would be highly desirable to accelerate progress in the field.

TNF-induced necroptosis

The best-characterized inducers of necroptosis are death receptor ligands, in particular, tumor necrosis factor (TNF; Moriwaki et al., 2015; Werner et al., 2008). TNF is a known master regulator of inflammation and cell death and has been at the forefront of many fundamental developments in cell biology that focus on the molecular interplay between death and survival signaling pathways (Figure 6; Liu et al., 2016; Vanlangenakker et al., 2011a). To date, studies have explored TNF-induced necroptosis in L929 cells (Vanden Berghe et al., 2015; Horn and Jackson, 1972; Schulz et al., 2006), a murine fibrosarcoma

cell line commonly used as a necroptosis execution model (Vanlangenakker et al., 2011a). However, other cell types including HEK293T, MEFs, HeLa, HT22, and JURKAT have also been shown to execute TNF-induced necroptosis (He and Ting, 2002; Lu et al., 2013; Vanlangenakker et al., 2011a; Wright et al., 2007). In all these cell types, the core necroptosis execution pathway is stimulated with TNF, following downstream activation of complex I & II, transduced by kinase activities of receptor interacting protein kinase-1 (RIP1), which undergoes ubiquitination, deubiquitination and downstream phosphorylation by receptor interacting protein kinase-3 (RIP3), eventually leading to the phosphorylation and activation of mixed lineage kinase domain like protein (pMLKL) and plasma membrane permeabilization (Zhou and Yuan, 2014a). Although many of the primary molecular species involved in necroptosis have been identified, including these core necroptosis mediators, RIP1, RIP3, MLKL, they are variably expressed by different cell types (He et al., 2009; Murphy et al., 2013; Vanlangenakker et al., 2012; Xu et al., 2018).

A recent review of TNF-induced necroptosis signaling (Samson et al., 2021) evaluated the chronology of signaling along the RIP-RIP3-MLKL axis and proposed that a network of modulators surrounds the necroptotic signaling core, tuned in a context-, cell type-, and species-dependent manner. For instance, even when cells express all core mediators of necroptosis, there is substantial variability in their ability to undergo MLKL-mediated cell death (Murphy et al., 2013; Najafov et al., 2019; Sai et al., 2019). As emphasized above, this is likely due to a plethora of modulators that tune signaling along the core necroptotic axis. Collectively, these studies highlight that the mechanisms that modulate necroptosis are not conserved across all cell types.

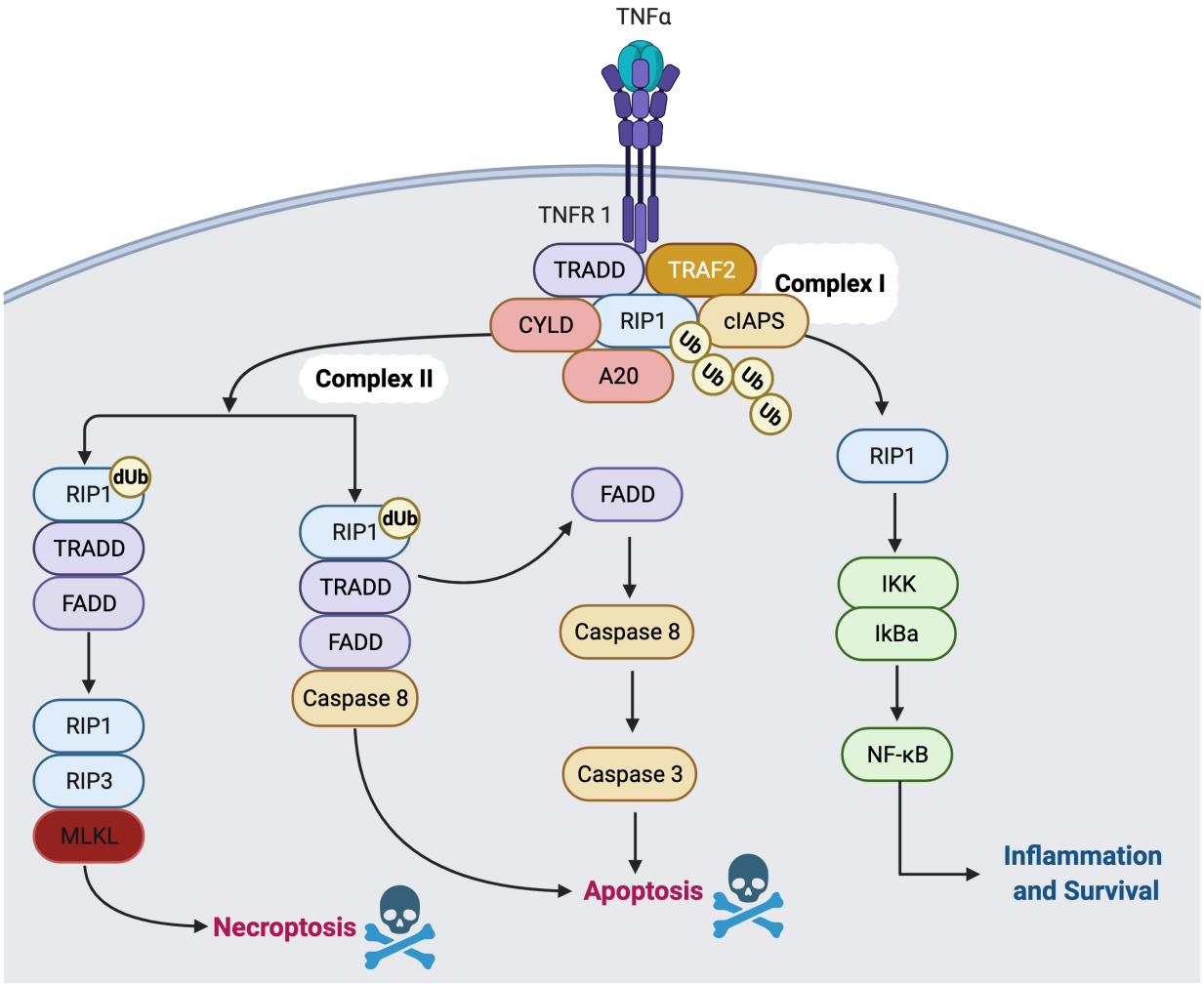

Figure 6: Signaling pathways after stimulation of TNF. Upon binding to its receptor, TNFR1, several proteins are recruited to form complex I, including TRADD, RIP1, TRAF2, and cIAP. Upon ubiquitination of RIP1 by cIAP, signaling will activate the inflammation and survival pathway by NF-*kappa*B. Alternatively, if RIP1 is deubiquitinated by CYLD or A20, complex II is formed. The association of FADD and C8 signals towards apoptosis, while the recruitment of RIP3, recruits MLKL, resulting in necroptosis.

The molecular mechanisms that control necroptosis execution from a systems perspective to understanding necroptosis across cell types remains to be elucidated. This is not due to a lack experimental effort, but rather due to the complexity associated with complex regulatory signaling processes and their associated complexity underlying biochemical interaction networks.

Prior studies (Choi et al., 2019; Hitomi et al., 2008; Lork et al., 2017; Moquin et al., 2013; Sun, 2020; Vanlangenakker et al., 2011b; Wertz et al., 2004; Zhou and Yuan, 2014b) of necroptosis also identified multiple mechanisms of ubiquitination regulation, including K63, K48, and M1 chains, which lead to phosphorylation of RIP1 and RIP3, phosphorylation and activation of cell death marker MLKL (Zhou and Yuan, 2014b), and plasma membrane permeabilization resulting in cell death (Samson et al., 2020). The K63-specific deubiquitinase CYLD (cylindromatosis lysine 63 deubiquitinase; Simonson et al., 2007) and the ubiquitin-editing enzyme A20 (tumor necrosis factor, alpha-induced protein 3; Sun, 2020) are both known to mediate deubiquitination of RIP1, which precedes RIP1 phosphorylation, by cleaving K63 ubiquitin chains and facilitating the formation of complex II (Choi et al., 2019; Hitomi et al., 2008; Lork et al., 2017; Moquin et al., 2013; Sun, 2020; Vanlangenakker et al., 2011b; Wertz et al., 2004). Therefore, both enzymes are generally considered drivers of necroptosis (Vandenabeele et al., 2010a). However, CYLD- and A20-driven deubiquitination of RIP1 have been paradoxically reported as pro- and anti-necroptotic in different cell types: some studies have shown that CYLD drives RIP1 deubiquitination (Kovalenko et al., 2003; Moquin et al., 2013; Simonson et al., 2007; Wright et al., 2007), while others have implicated A20 (Gurung et al., 2015; Lu et al., 2013; Wertz et al., 2004) or reported equal contributions from both enzymes (Dondelinger et al.,

2016; Draber et al., 2015; Vanlangenakker et al., 2011a). These varying reports have led to unresolved controversies within the field regarding the specific molecular mechanisms of complex II formation and subsequent necroptotic cell death (Vanlangenakker et al., 2012). For example, repression of CYLD in L929 cells, a murine fibrosarcoma cell line, protects from TNF-induced necroptosis but, unexpectedly, A20 repression increases sensitivity to necroptosis (Vanlangenakker et al., 2011a). A recent time-resolved analysis of necroptosis rates and network components revealed an incoherent feedforward loop through which NF-kB and A20 counteract pro-necroptotic signaling in L929 cells (Metzig et al., 2020), but it remains unclear how general or cell context-dependent this regulatory control of necroptosis is.

SUMMARY

Here, we present, to our knowledge, the first detailed biochemical model of TNF-induced necroptosis. The model is derived from published literature and incorporates known biology obtained from decades' worth of experimental studies (Table 1). We calibrate the model to experimental phosphorylated MLKL (pMLKL) time course data from TNF-treated mouse fibrosarcoma cells at multiple TNF doses. We then perform a dynamical systems analysis that identifies four modes of necroptosis signal execution. In one case, A20 and CYLD contribute approximately equally to RIP1 deubiquitination, such that both must be knocked out to delay necroptosis induction (knocking out one has no effect, since the signal can be rerouted through the other). In another, RIP1 deubiquitination is driven exclusively by CYLD, with A20 being effectively inactive. In the other two modes, either A20 or CYLD acts as the driver of RIP1 deubiquitination, with the other enzyme, counterintuitively, acting to inhibit necroptosis (consistent with the observation by

Vanlangenakker et al. (Vanlangenakker et al., 2011a)). We also perform sensitivity analyses to identify proteins and kinetic parameters that can be targeted within each mode to modulate pMLKL dynamics and time-to-death (TTD) by necroptosis. We find that, for two modes, proteins and rate constants centered around RIP1 ubiquitination regulation in complex I have the most significant effect on necroptosis execution. For the other two, potential targets include factors involved in the balance between complex II degradation and necrosome formation. Overall, our results show that a consensus pathway model of TNF-induced necroptosis can explain numerous experimentally observed behaviors, including conflicting and counterintuitive results from multiple studies involving different cell types. Following a detailed description of our proposed model, we present results of the parameter calibration, dynamical systems analysis, *in silico* knockout experiments, and sensitivity analyses. We conclude with a discussion of the broader implications of our results, including important insights into the molecular mechanisms of necroptosis execution and the potential for using the model to identify novel pro- and anti-necroptosis therapeutic targets.

RESULTS

A biochemical model of TNF-induced necroptosis describes formation of key signaling complexes along the path to cell death

The death receptor ligand TNF (Li and Beg, 2000), an extensively studied inducer of necroptosis and well-known master regulator of inflammation, has been at the forefront of numerous fundamental discoveries concerning the interplay between cell death and survival pathways (Vanlangenakker et al., 2011a). Here, we propose a detailed, mechanistic model of TNF-induced necroptosis based on an extensive review of the literature (Table 1, with references). The model comprises 14 proteins interacting via 40 reactions (all mass action) to produce 37 biochemical species, including complex I, complex II, and the necrosome (Figure 7), three key macromolecular complexes along

Table 1: Key proteins involved in necroptosis.

Protein	Role in necroptosis	Refs.
A20	Ubiquitin-editing enzyme responsible for deubiquitinating RIP1 in complex I	(Gurung et al., 2015; Wertz et al., 2004)
Caspase -8	Heterodimerizes with cFLIPL (long isoform), leading to cleavage and inactivation of RIP1 and RIP3 in complex II	(Feltham et al., 2017; Micheau et al., 2002)
cFLIPL	Heterodimerizes with caspase-8, leading to cleavage and inactivation of RIP1 and RIP3 in complex II	(Oberst et al., 2011; Tsuchiya et al., 2015)
cIAP1/2	Catalyzes, via its RING domains, the activating K63-linked polyubiquitination of RIP1	(McComb et al., 2012; Vanlangenakker et al., 2011a)
CYLD	Deubiquitinates RIP1 in either complex I or within the RIP1-RIP3 necrosome	(Moquin et al., 2013; Simonson et al., 2007)
FADD	TNFR1-interacting scaffold protein in complex II	(Hsu et al., 1996a; Lawrence and Chow, 2005; Vandenabeele et al., 2010a)
LUBAC	TNFR1-interacting protein recruited by cIAP1/2 in complex I that promotes RIP1 ubiquitination	(Haas et al., 2009; Vanlangenakker et al., 2011a)
MLKL	Recruited to the necrosome by RIP1, where it is phosphorylated, leading to cell death by membrane rupture	(Grootjans et al., 2017; Sun et al., 2012; Wegner et al., 2017)
Pro-caspase-8	Recruited via its death effector domain to complex II and cleaved to yield active caspase-8	(Feltham et al., 2017; Micheau et al., 2002)
RIP1	A multifunctional adaptor protein in the necrosome that recruits and activates RIP3 and MLKL	(O'Donnell and Ting, 2011; Vandenabeele et al., 2010b; Vanlangenakker et al., 2011a)
RIP3	Recruited to the necrosome by binding to and cross-phosphorylating RIP1	(Feng et al., 2007; He et al., 2009; Wegner et al., 2017)
TNF	Pleiotropic pro-inflammatory cytokine that activates necroptosis in the absence of caspase activity	(Carswell et al., 1975)
TNFR1	TNF receptor superfamily member death receptor that recruits RIP1 to complex 1	(Hsu et al., 1996b; Wajant and Siegmund, 2019)
TRADD	TNFR1-interacting protein in complexes I and II that serves as a docking adaptor for the binding of RIP1 to TRAF2	(Hsu et al., 1996b; Pobezinskaya and Liu, 2012)
TRAF2	TNFR1-interacting protein that recruits cIAP1/2 to complex I, promoting K63-linked RIP1 ubiquitination	(Hsu et al., 1996a; Wang et al., 1998)

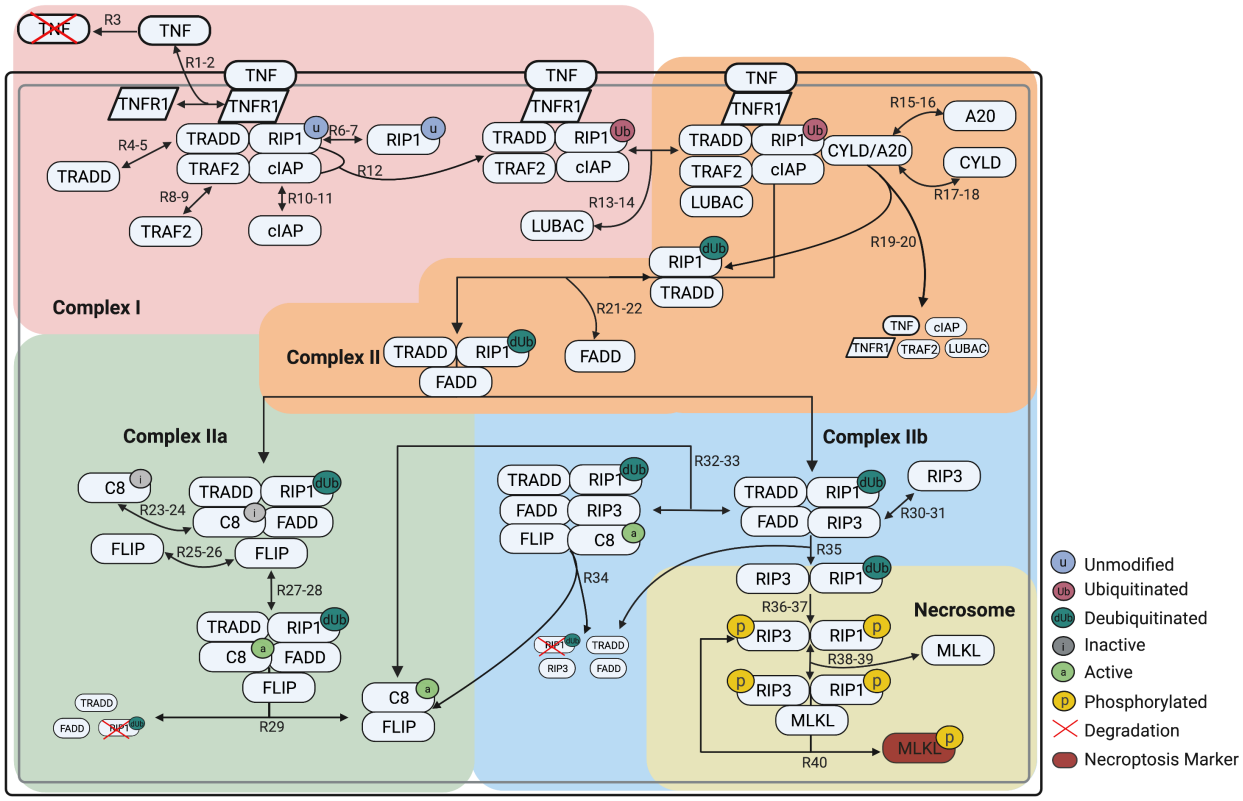

Figure 7: Schematic of the necroptosis execution model. The diagram is color coded to highlight the processes involved in formation of complex I, complex II, complex IIa, complex IIb, and the necrosome. Arrows are labeled with 'RN' or 'RN-M', where N and M correspond to reaction indices in the model. In many (but not all) cases, 'R_{N-M}' denotes a set of reversible reactions, with N the index for the forward direction and M for the reverse. Created with BioRender.com.

the path from cell-death cue to necroptosis execution. Below, we describe in detail the steps involved in the formation of each complex, beginning with TNF binding to TNF receptor 1 (TNFR1) and ending at phosphorylation of the necroptosis cell death reporter MLKL. A model schematic is provided as a visual aid (Figure 7), with reactions, including association, dissociation, phosphorylation, ubiquitination, deubiquitination, and degradation, denoted as "R_N," where N is the reaction number. Note that protein synthesis is omitted from the model because all experiments were performed in the presence of cycloheximide, commonly used to sensitize cells to the action of TNF (Wallach, 1984).

Signaling through the necroptosis pathway is initiated when the cytokine TNF binds to the extracellular domain of TNFR1 ($R_{1\text{-}2}$), which protects TNF from degradation (R_3) and activates the receptor by causing a conformational change in its intracellular domain (Van Antwerp et al., 1996; Vanlangenakker et al., 2011a; Wajant and Siegmund, 2019). The adaptor protein TRADD (TNFR1-associated death domain) is then recruited to the intracellular domain of TNFR1 ($R_{4\text{-}5}$) to facilitate binding of RIP1 (unmodified; $R_{6\text{-}7}$) and TRAF2 (TNFR-associated factor 2; $R_{8\text{-}9}$) (Liu et al., 2016; Pobezinskaya and Liu, 2012; Zheng et al., 2006).TRAF2 recruits and binds cIAP1/2 (cellular inhibitor of apoptosis proteins 1 and 2; $R_{10\text{-}11}$), which then add non-degradative polyubiquitin chains to RIP1 (R_{12}) (Zhou and Yuan, 2014b). Ubiquitinated RIP1 recruits other necessary components to the complex, including LUBAC (linear ubiquitin chain assembly complex; $R_{13\text{-}14}$). We refer to the supramolecular structure, which is anchored to the cell membrane and composed of TNF, TNFR1, TRADD, ubiquitinated RIP1, TRAF2, cIAP1/2, and LUBAC, as complex I (Etemadi et al., 2015; Wallach, 1984) (Figure 7, *pink*). Biologically, complex

I is known to drive multiple pathways in addition to necroptosis, including apoptosis and the inflammatory NFkB pathway (Gong et al., 2019).

Formation of complex I is followed by deubiquitination of RIP1 by the enzymes A20 (Gurung et al., 2015; Sun, 2020) and CYLD (Kovalenko et al., 2003; Moquin et al., 2013; Simonson et al., 2007; Wright et al., 2007), which competitively bind to RIP1 in its ubiquitinated state ($R_{15\text{-}18}$), causing cleavage, deubiquitination, and release in association with TRADD and the dissolution of complex I ($R_{19\text{-}20}$). The RIP1:TRADD heterodimer then recruits FADD (Fas-associated protein with death domain; $R_{21\text{-}22}$), initiating the formation of complex II, also known as the cytosolic death-inducing signaling complex (Figure 7, *orange*). Complex II can then be modified via two competing paths, one anti-necroptotic and one pro-necroptotic. The anti-necroptotic path involves FADD, via its death effector domain, mediating the recruitment of inactive Caspase 8 (C8i; $R_{23\text{-}24}$) (Micheau and Tschopp, 2003) which subsequently binds FLIP (cellular FADD-like IL-1β-converting enzyme-inhibitory protein; $R_{25\text{-}26}$), resulting in the complex commonly referred to as complex IIa (Figure 7, *green*) (Micheau and Tschopp, 2003; Vanlangenakker et al., 2011a). FLIP then oligomerizes with C8i to produce active Caspase-8 (C8a; $R_{27\text{-}28}$) (Micheau et al., 2002; Tsuchiya et al., 2015) which cleaves RIP1 for truncation (i.e., degradation), resulting in dissolution of the complex and release of the active C8a:FLIP heterodimer (Feoktistova et al., 2011; McIlwain et al., 2013) (R_{29}) that directly inhibits necroptosis ($R_{32\text{-}34}$).

The pro-necroptotic path involves formation of complex IIb (Figure 7, *blue*), which occurs when deubiquitinated RIP1 in complex II recruits RIP3 (receptor-interacting protein kinase 3; $R_{30\text{-}31}$), blocking C8i recruitment ($R_{23\text{-}24}$). The C8a:FLIP heterodimer can then

be recruited to complex IIb ($R_{32\text{-}33}$), which cleaves RIP1 for truncation, leading to dissolution of the complex (R_{34}). Alternatively, RIP3 and deubiquitinated RIP1 can dissociate from complex IIb as a heterodimer (R_{35}) (Vanlangenakker et al., 2011a). Cross-phosphorylation of RIP3 (R_{36}) and then RIP1 (R_{37}), followed by recruitment of MLKL ($R_{38\text{-}39}$) (Declercq et al., 2009; Moriwaki and Chan, 2013), results in the necroptosis signaling complex, known as the necrosome (Figure 7, *yellow*) (Vanlangenakker et al., 2011a). Phosphorylation of MLKL (Sun et al., 2012) in the necrosome by phosphorylated RIP1 and RIP3 is followed by release of pMLKL from the phosphorylated RIP1:RIP3 heterodimer (R_{40}), which is again free to bind MLKL. We assume dephosphorylation and degradation of the phosphorylated RIP1:RIP3 heterodimer is negligible, consistent with experimental reports (Cho et al., 2009). Translocation of pMLKL to the cell membrane (Ronan et al., 2016) then causes rapid plasma membrane rupture and inflammatory response due to the release of DAMPs (damage-associated molecular patterns) and cytokines (Pasparakis and Vandenabeele, 2015), ultimately resulting in cell death.

Western blots and mass spectrometry enable Bayesian parameter estimation of the necroptosis model

To explore the dynamics of our computational necroptosis model, we first calibrated it to experimental protein time course data using a Bayesian parameter estimation approach (Shockley et al., 2018). Briefly, we used L929 cells, a murine fibrosarcoma cell line that is a well-established model system for studying necroptosis (Vanlangenakker et al., 2011a). Cells were treated with 100, 10, 1, and 0.1 ng/ml of TNF over 16 hours and pMLKL levels were estimated at multiple time points via Western blot using Bio-Rad (Figure 8A). To quantify initial protein abundances, used as inputs to the model, we used label-free mass spectrometry in untreated L929 cells for proteins C8, FADD, MLKL, RIP3,

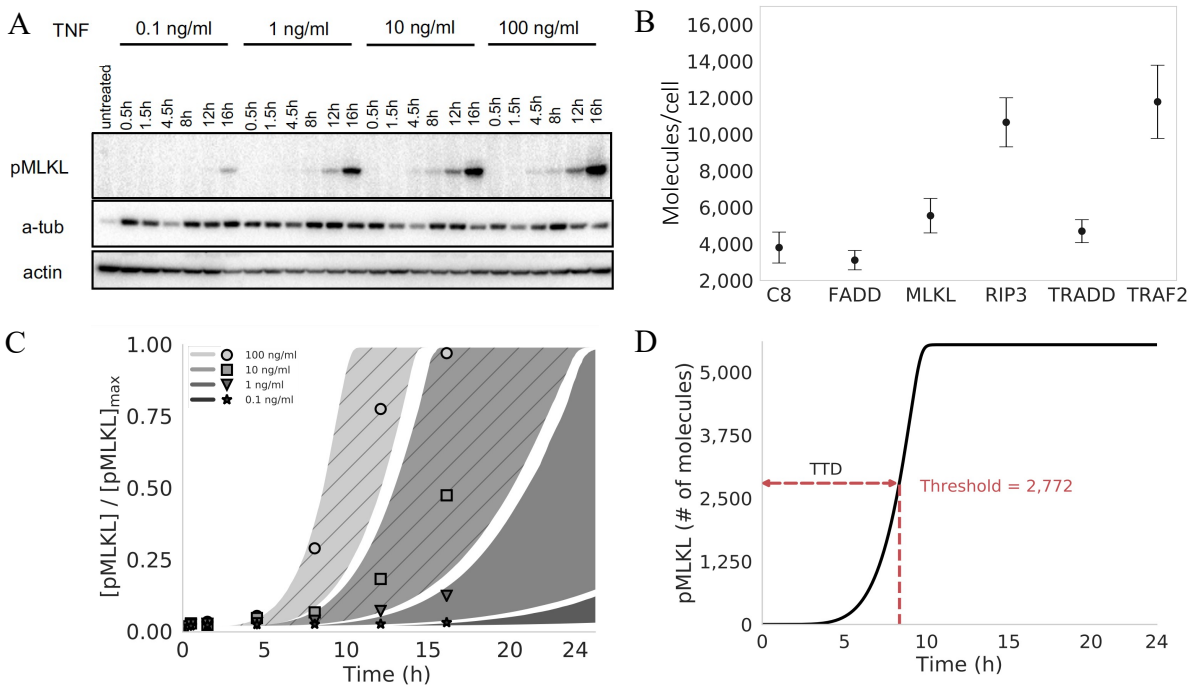

Figure 8: Proteomics, parameter calibration, and quantifying time-to-death. (A) Western blots for phosphorylated MLKL (pMLKL) at multiple time points in L929 (murine fibrosarcoma) cells under 0.1–100 ng/ml TNF stimulation. Alpha tubulin (a-tub) and actin, used as loading controls, are shown for comparison. (B) Mass spectrometry data from untreated L929 cells for multiple proteins involved in necroptosis execution. Points represent the median of three replicates (used as input to the computational model); error bars span the interquartile range. (C) Simulated pMLKL time courses (plotted as 95% probability envelopes) for 0.1–100 ng/ml TNF stimulation (same concentrations as in *A*) based on 10,628 parameter sets obtained from Bayesian parameter estimation. The model was calibrated to the 100 and 10 ng/ml TNF data only (shaded regions with diagonal lines); time courses for the lowest TNF concentrations (shaded regions with no diagonal lines) amount to a simple model validation. Points correspond to the Western blot data in *A*, quantified via densitometry. Points and shaded regions are colored the same, based on TNF dose. (D) Illustration of the time-to-death (TTD) metric used to quantify cell death *in silico*. A hard threshold of 2,772 molecules (half the median MLKL level in *B*) was chosen to signify cell death (see Materials and Methods). MLKL: mixed lineage kinase domain-like protein; TNF: tumor necrosis factor.

TRADD, and TRAF2 (Figure 8B). All other initial protein levels (other than TNF, which depends on applied dose) were set to values based on biologically plausible assumptions (Table 2). Parameter estimation (Figure 9) was then performed using PyDREAM (Shockley et al., 2018), a multi-chain Monte Carlo sampling tool, with a multi-objective cost function that included data from the two highest TNF doses (100 and 10 ng/ml; Figure 8C). In all, an ensemble of 10,628 parameter sets and their prior (before fitting) and posterior (after fitting) distribution probabilities were obtained (Figure 10), all of which reproduce the experimental data reasonably well (Eydgahi et al., 2013). Model simulations at the two lowest TNF doses (1 and 0.1 ng/ml; Figure 8C) showed good correspondence to experimental data, providing a simple validation of the model fits.

Table 2: Initial protein levels used as input to the computational model. Proteins shown in bold were either measured by mass spectrometry in this work or, in one case, based on applied dose (TNF). Initial amounts for the other proteins were obtained from the literature (Hua et al., 2005; Uhlén et al., 2005, 2015).

Protein	**Amount (molecules)**	**Source**
A20	9,075	Calculated
C8	3,799	This work
cIAP	8,986	Calculated
CYLD	9,075	Calculated
FADD	3,109	This work
FLIP	3,900	Calculated
LUBAC	7,226	Calculated
MLKL (unmod)	5,544	This work
RIP1	20,044	Calculated
RIP3	10,654	This work
TNF*	2,326	This work
TNFR	4,800	Calculated
TRADD	4,696	This work
TRAF2	11,776	This work

*100 ng/ml

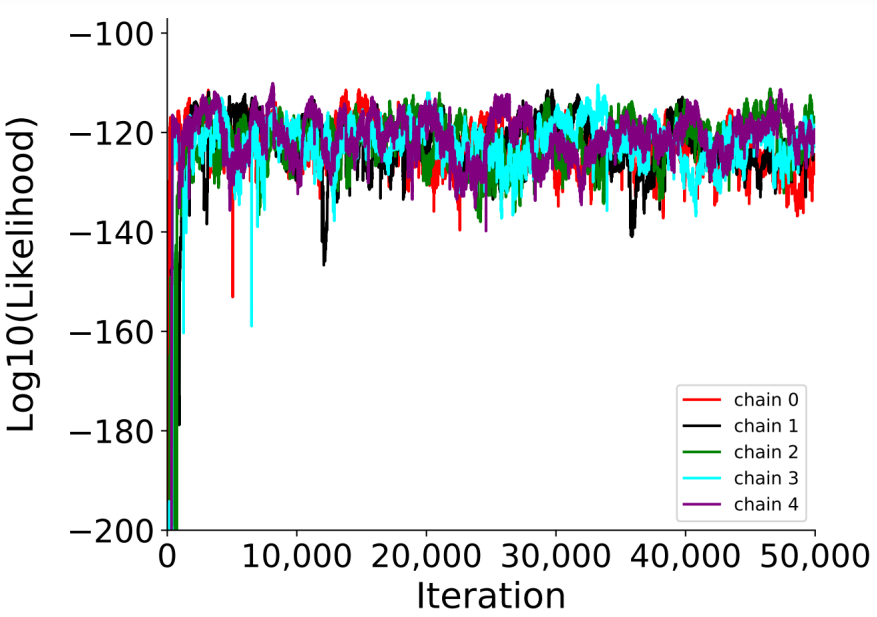

Figure 9: Log-likelihood vs. iteration for all five Markov chains used in the Bayesian parameter calibration. For each chain, the first 25,000 iterations were discarded (considered burn-in), leaving a total of 125,000 parameter sets total, of which 10,628 are unique.

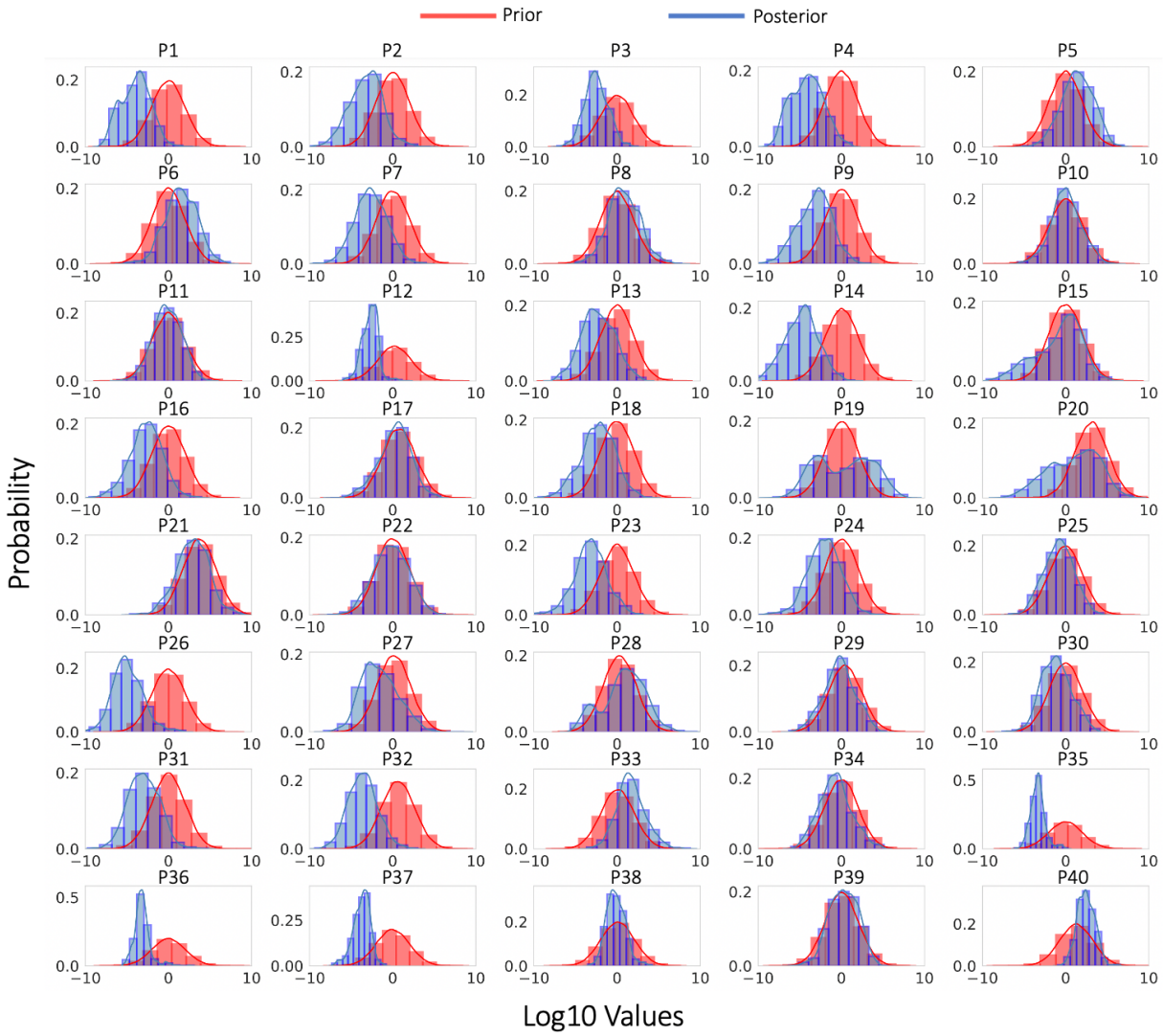

Figure 10: Distributions of parameter values from Bayesian model calibration. Both prior (red) and posterior (blue) distributions are shown.

A dynamical systems analysis identifies four distinct necroptosis execution modes differing by mechanism of RIP1 ubiquitination regulation

We performed a dynamical systems analysis to explore the possibility that distinct "modes of necroptosis execution" exist within the parameter set ensemble obtained from Bayesian parameter estimation. The rationale is that while different parameterizations of the model achieve cell death at approximately equal times, they may arrive there via significantly different sequences of molecular events. We utilized a computational tool (Ortega et al., 2021) that identifies subnetworks of reactions that dominate the production or consumption of a target species, pMLKL in this case, at user-specified times along a time course. Each subnetwork is given an integer label and each time point is associated with a subnetwork. Thus, a continuous concentration time course is "digitized" into a sequence of integers, which we refer to as a "dynamical signature." This transformation enables simple comparisons between time courses obtained with different parameter sets using standard dissimilarity metrics, such as the longest common subsequence (Studer and Ritschard, 2016). Applying this approach to all 10,628 parameter sets obtained from Bayesian parameter estimation of our necroptosis model and clustering the resulting dynamical signatures using a spectral clustering algorithm (Figure 11) (Rokach and Maimon, 2005), we obtained four distinct clusters, or modes of necroptosis execution (Figure 12A).

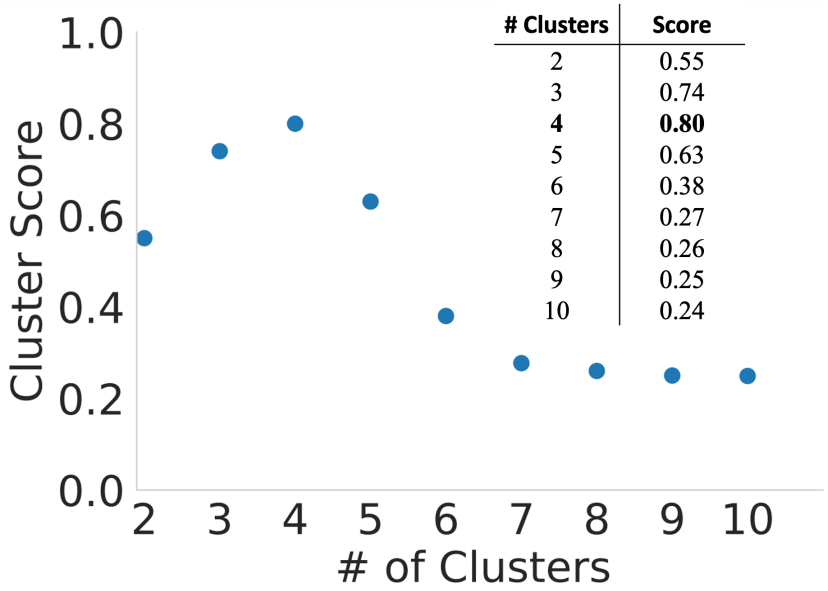

Figure 11: Silhouette clustering scores for determining the number of modes of necroptosis execution. The maximum value is for four clusters. Values were also calculated for 11-20 clusters and were all <0.3 (data not shown).

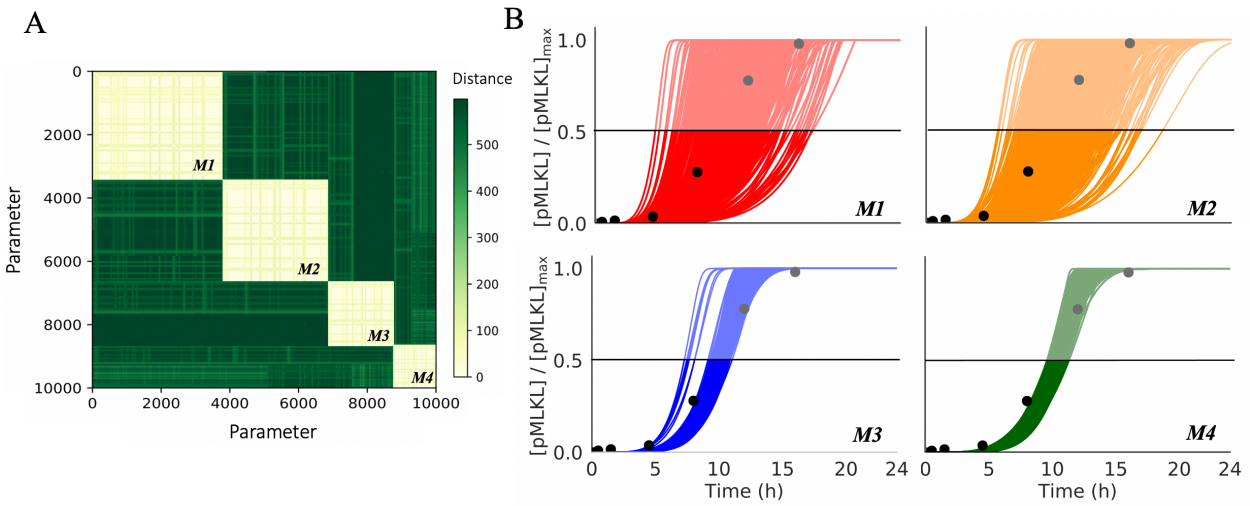

Figure 12: Four modes of necroptosis execution exhibit variability in temporal dynamics and differ in rate constant values and responses to CYLD and A20 knockouts. (A) Clustering analysis of simulated time courses (100 ng/ml TNF) from 10,628 parameter sets reveals four distinct modes of execution (*M1*, …, *M4*). Dissimilarity ("distance") between dynamical signatures (digitized time courses) was quantified using the longest common subsequence (see Materials and Methods). (B) Simulated time courses (100 ng/ml TNF) of the necroptosis marker, phosphorylated MLKL (pMLKL), show significantly more variability in time-to-death (TTD; defined as the time at which pMLKL reaches its half-maximal value) in modes 1 and 2. Time courses for all parameter sets associated with each mode are shown. Experimental Western blot data (black circles; quantified from Figure 8A) is included to illustrate the model fit for each mode.

Interestingly, two of the execution modes exhibit significantly more variability in pMLKL temporal dynamics and TTD (defined in Figure 8D) across their associated parameter sets than the other two (Figure 12 B). This suggests the modes harbor fundamental differences in rate constant values that lead to differential robustness to parameter variations. To explore this further, we compared the distributions of rate constants across modes and identified eight (out of 40) with significant differences (>7.5-fold) between the largest and smallest mean (Figure 13A; additional distributions are shown in Figure 14, corresponding descriptions in Table 3). We also consider distributions for two rate constants (P12 and P13; parameter indices correspond to reaction indices in Figure 7) with much smaller differences across means (~3-fold in both cases) but for which the model exhibits high sensitivity (discussed in the next subsection). In all, these 10 rate constants correspond to reactions spanning the model topology, starting with the association of TRADD to complex I (P4), which has a somewhat increased rate in mode 4. Further downstream, the rate constant for ubiquitination of RIP1 by cIAP (P12) is slightly larger in mode 1 than in the other modes. Small differences are also seen for the binding rate of LUBAC to complex I (P13). The rate constant for binding of A20 to ubiquitinated RIP1 (P15) is significantly smaller in mode 4 than in the other modes and somewhat smaller in mode 2 relative to modes 1 and 3. Deubiquitination of RIP1 by A20 (P19) is significantly reduced in modes 2 and 4, while, interestingly, the rate constant for RIP1 deubiquitination by CYLD (P20) in mode 1 is reduced by almost the same amount relative to the other modes. For activation/deactivation of C8 in complex IIa, which is a critical step in the pathway for determining whether the cell will progress to necroptosis, mode 4 has both a significantly larger activation (P27) and significantly smaller

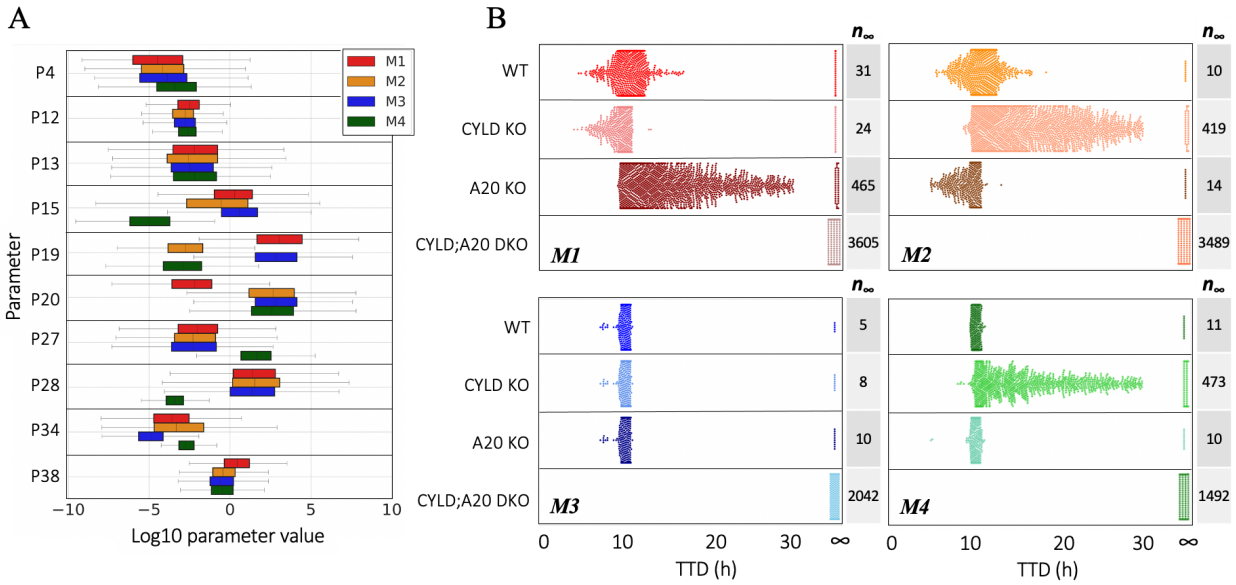

Figure 13: Four modes of necroptosis execution exhibit variability in temporal dynamics and differ in rate constant values and responses to CYLD and A20 knockouts. (A) Variations in the values of eight rate constants (PN, where N corresponds to the associated reaction index in Figure 7) distinguish the four modes of execution. (B) Knockouts of CYLD and A20 (100 ng/ml TNF) differentially affect TTD, relative to wild type (WT), across the four modes (each dot corresponds to a parameter set). CYLD/A20 double knockout inhibits cell death in all cases (TTD = ∞). The number of parameter sets that do not result in cell death (n_∞) are included for all modes under all conditions. KO: knockout; DKO: double knockout.

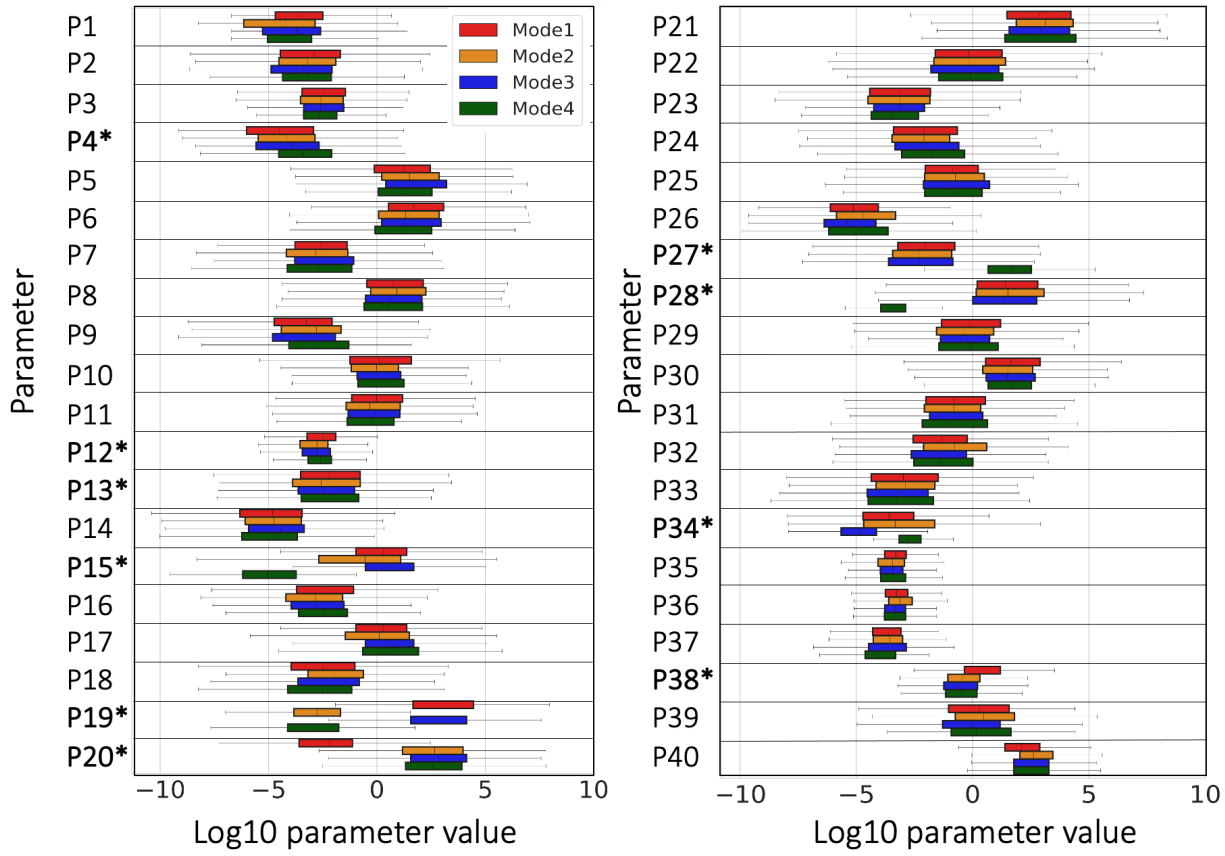

Figure 14: Four modes of necroptosis execution exhibit variability in temporal dynamics and differ in rate constant values and responses to CYLD and A20 knockouts. (A) Clustering analysis of simulated time courses (100 ng/ml TNF) from 10,628 parameter sets reveals four distinct modes of execution (M1, …, M4). Dissimilarity ("distance") between dynamical signatures (digitized time courses) was quantified using the longest common subsequence (see Materials and Methods).

Table 3: Parameter values and reaction descriptions. CI: complex I; RIP1-u: unmodified RIP1; RIP1-Ub: ubiquitinated RIP1; RIP1-dUb: RIP1 deubiquitinated; C8i: inactive C8; C8a: active C8; RIP1p: RIP1 phosphorylation; RIP3p: RIP3 phosphorylation; MLKLp: MLKL phosphorylation

Parameter	Reaction	Parameter	Reaction
P1	Association of TNF to TNFR	**P21**	Association of FADD to RIP1(dUb):TRADD in complex II
P2	Dissociation of TNF:TNFR	**P22**	Dissociation of FADD from RIP1(dUb):TRADD in complex II
P3	Degradation of TNF	**P23**	Association of inactive C8 (C8i) to FADD in complex IIa
P4	Association of TRADD to complex I	**P24**	Dissociation of C8i from complex IIa
P5	Dissociation of TRADD from complex I	**P25**	Association of FLIP to C8i in complex Iia
P6	Association of RIP1-u to complex I	**P26**	Dissociation of FLIP from C8i in complex IIa
P7	Dissociation of RIP1-u from complex I	**P27**	Activation of C8i:FLIP -> C8a:FLIP heterodimer in complex IIa
P8	Association of TRAF2 to complex I	**P28**	Inactivation of C8a:FLIP -> C8i:FLIP in complex IIa
P9	Dissociation of TRAF2 from complex I	**P29**	Degradation of RIP1(dUb) by C8a:FLIP in complex IIa
P10	Association of cIAP to complex I	**P30**	Association RIP3 to RIP1(dUb) in complex IIb
P11	Dissociation of cIAP from complex I	**P31**	Dissociation of RIP3 from RIP1(dUb) in complex IIb
P12	Ubiquitination of RIP1-u by cIAP in complex I	**P32**	Association of C8a:FLIP to complex IIb
P13	Association of LUBAC to RIP1-Ub in complex I	**P33**	Dissociation of C8a:FLIP from complex IIb
P14	Dissociation of LUBAC from RIP1-Ub in complex I	**P34**	Degradation of RIP1(dUb) by C8a:FLIP in complex IIb
P15	Association of A20 to RIP1-Ub in complex I	**P35**	Dissociation of RIP1(dUb):RIP3 from complex IIb to necrosome
P16	Dissociation of A20 from complex I	**P36**	Phosphorylation of RIP1(p) by RIP3 in necrosome
P17	Association of CYLD to RIP1-Ub in complex I	**P37**	Phosphorylation of RIP3 by RIP1(p) in necrosome
P18	Dissociation of CYLD from complex I	**P38**	Association of MLKL to necrosome
P19	Deubiquitination of RIP1-Ub by A20 to complex II	**P39**	Dissociation of MLKL from necrosome
P20	Deubiquitination of RIP1-Ub by CYLD to complex II	**P40**	Phosphorylation of MLKL(p)

deactivation (P28) rate constant. The rate constant for subsequent RIP1 degradation by the active C8a:FLIP heterodimer to complex IIb (P34), which inhibits necroptosis, is somewhat smaller in mode 3 and larger in mode 4 relative to the other modes. Finally, the binding rate constant for MLKL to the phosphorylated RIP1:RIP3 heterodimer (P38), the final step in the formation of the necrosome, is somewhat increased in mode 1. These results clearly illustrate that significant differences exist in the values of rate constants across the modes of execution, despite the similarities in pMLKL temporal dynamics.

CYLD and A20 are known regulators of RIP1 deubiquitination (Choi et al., 2019; Hitomi et al., 2008; Lork et al., 2017; Moquin et al., 2013; Sun, 2020; Vanlangenakker et al., 2011b; Wertz et al., 2004) but have been reported as both drivers and inhibitors of necroptosis in different cell types (Dondelinger et al., 2016; Draber et al., 2015; Kovalenko et al., 2003; Moquin et al., 2013; Simonson et al., 2007; Vanlangenakker et al., 2011a; Wright et al., 2007). To investigate the roles of CYLD and A20 in our necroptosis model, we performed *in silico* CYLD and A20 knockout (KO) experiments and compared TTD distributions to the unperturbed, i.e., "wild-type" (WT), case (Figure 13B). Unsurprisingly, in all cases CYLD/A20 double KO (DKO) prevents cell death (TTD = ∞). However, for single CYLD KO and A20 KO, we see highly variable responses across the four modes of execution. For mode 1, we see that knocking out A20 leads to a general increase in TTD (i.e., decrease in necroptosis sensitivity) across the parameter sets, consistent with A20 acting as a regulator of RIP1 ubiquitination and driver of necroptosis (Gurung et al., 2015; Sun, 2020). Conversely, CYLD KO results in a general reduction in TTD (i.e., increase in sensitivity), indicating that CYLD in mode 1 counterintuitively operates as an inhibitor of necroptosis. We see the opposite trends in mode 2: A20 KO reduces TTD,

while CYLD KO leads to a general increase in TTD across the parameter sets. This result is consistent with observations by Vanlangenakker et al. (Vanlangenakker et al., 2011a) that A20 depletion can sensitize cells to death by necroptosis. In mode 3, we see that single KOs of A20 and CYLD have no effect on TTD. Since DKO prevents cell death in all cases, this reveals that A20 and CYLD both drive RIP1 deubiquitination and, hence, when one enzyme is knocked out signal flow diverts through the other. Finally, in mode 4, CYLD KO leads to a general increase in TTD, like mode 2; however, A20 KO has no effect, as in mode 3. In all, the results of *in silico* KO experiments reveal distinct differences in the roles of A20 and CYLD in RIP1 ubiquitination regulation among the four model-predicted modes of necroptosis execution (summarized in Table 4).

Table 4: Roles of A20 and CYLD in RIP1 deubiquitination and necroptosis execution in the four signal execution modes. ⇓: decrease; ⇑: increase; →: leads to; TTD: time-to-death.

Mode 1	• A20 ⇓ → TTD ⇑ • CYLD ⇓ → TTD ⇓	• A20 deubiquitinates RIP1 • CYLD (counterintuitively) inhibits necroptosis
Mode 2	• CYLD ⇓ → TTD ⇑ • A20 ⇓ → TTD ⇓	• CYLD deubiquitinates RIP1 • A20 (counterintuitively) inhibits necroptosis
Mode 3	• CYLD ⇓ → TTD ⇑ • A20 ⇓ → TTD constant	• CYLD deubiquitinates RIP1 • A20 has no significant role in necroptosis execution
Mode 4	• A20 ⇓ → TTD constant • CYLD ⇓ → TTD constant • A20 ⇓ + CYLD ⇓ → TTD ⇑	• Both A20 and CYLD can drive RIP1 deubiquitination • If one is knocked out, the signal can reroute through the other

Ubiquitination of RIP1 by cIAP in complex I and binding of LUBAC to complex I are global modulators of necroptosis sensitivity across execution modes

Targeting necroptosis by small molecule modulators has emerged as a promising approach for both cancer therapy and treatment of inflammatory diseases (Wu et al., 2020). It is of interest, therefore, to determine if modulating factors exist that are common across all modes of execution, which could represent novel therapeutic targets. Towards this end, we performed sensitivity analyses based on "representative" parameter sets for each mode (automatically generated by our dynamical systems analysis tool) (Ortega et al., 2021) over the 14 non-zero initial protein concentrations (Figure 15A) and 40 rate constants (Figure 16A and Figure 17). Initial protein concentrations were varied ± 20% around a reference set of concentrations (Table 7) used for parameter estimation; rate constant values were varied ± 20% around the representative parameter set for each mode. We then validated the results of these analyses (i.e., to confirm they are not specific to the representative parameter set) by performing, for all parameter sets associated with each mode, *in silico* knockdowns (KDs) by 70% and 10-fold overexpression (OE) for the initial concentrations (Moriya, 2015; Taxman et al., 2006) (Figure 15B) and by varying the rate constants values ± 10-fold (Figure 16B, 17).

Across the four modes of execution, we see three common protein modulators of necroptosis sensitivity: TNF, TNFR, and MLKL (Figure 15). These are not unexpected (and, hence, not novel targets), since these proteins are well-known master regulators of TNF-induced necroptosis (Samson et al., 2021; Vercammen et al., 1997). More interestingly, for the rate constants, we see three common modulators across the four modes (Figure 16) corresponding to the association of TNF to TNFR (P1), ubiquitination of RIP1 by cIAP in complex I (P12), and association of LUBAC (P13) to complex I (see

Figure 7, *pink*). The former is not unexpected, given that TNF is the death-inducing stimulus driving necroptosis. However, the latter two are not intuitively obvious and, hence, are potential global targets predicted by our model. Specifically, for all four modes, we see that increasing the values of these two rate constants (P12 and P13) leads to a significant decrease in TTD (i.e., increased sensitivity to necroptosis), and vice versa. Note that the analyses based on the representative parameter set (Figure 16A) show only that TTD decreases when these two rate constant values are increased. However, by repeating the analyses over all parameter sets associated with each mode (Figure 16B), we confirm that TTD also increases (i.e., sensitivity to necroptosis decreases) when the rate constant values are decreased.

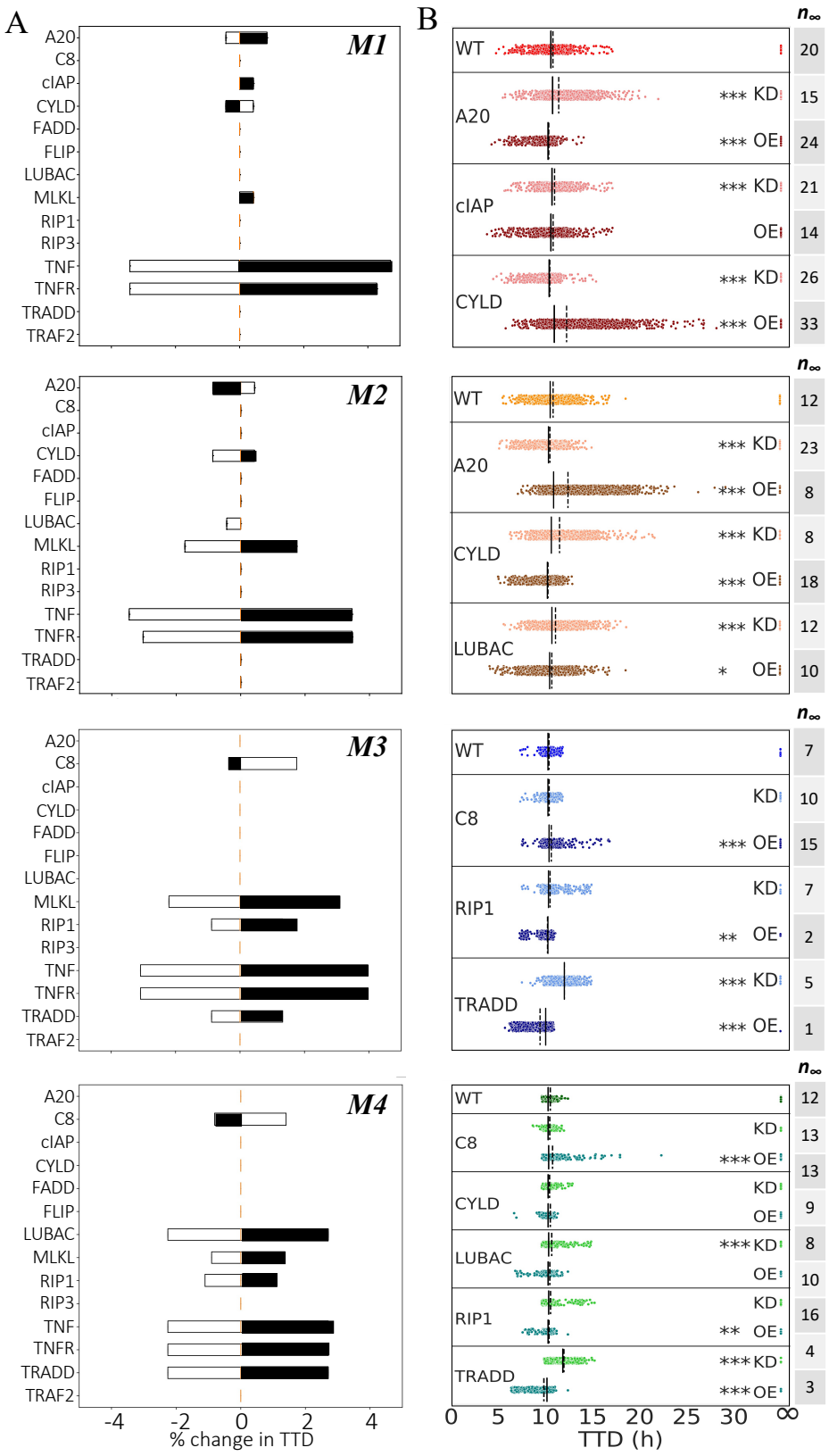
A
B
M1
M2
M3
M4
A20
C8
cIAP
CYLD
FADD
FLIP
LUBAC
MLKL
RIP1
RIP3
TNF
TNFR
TRADD
TRAF2
WT
KD
OE
*** KD
*** OE
** OE
* OE
n∞
-4
-2
0
2
4
% change in TTD
0
5
10
15
20
25
30
∞
TTD (h)

Figure 15: Sensitivity analyses and model-predicted protein targets for each mode of execution. (A) Changes in TTD for "representative" parameter sets of each mode. Black shaded regions signify decreases in initial protein concentrations; white shaded regions signify increases. (B) Knockdown (KD; 70%) and overexpression (OE; 10-fold) of potential targets identified in A for all parameter sets for each mode. The number of parameter sets that do not result in cell death (n_∞) are included. Solid black lines = medians, dashed black lines = means; * $p < 0.05$, ** $p < 0.01$, *** $p < 0.001$ (Mood's median test).

Sensitivities to initial protein levels and rate constant values reveal execution mode-dependent targets for modulating time-to-death

We have shown that the four modes of necroptosis execution (Figure 12A) exhibit differences in variability in TTD (Figure 12), rate parameter values (Figure 13A), and responses to A20 and CYLD KOs (Fig. 3D). This suggests that, in addition to the global modulators identified above (TNF, TNFR, MLKL, P1, P12, P13; Figs. 4 and 5), each mode also has a unique set of factors that drive response. For mode 1, these include proteins, i.e., A20, cIAP, and CYLD (Figure 15–*top row*), and rate constants (P10, P11, P15–P19; Figure 16–*top row* and Figure 14) associated with RIP1 ubiquitination regulation in complex I (see Figure 7, *orange*). The sensitivities to A20 and CYLD are consistent with the results from *in silico* KO experiments (Figure 13B). Intuitively, we can understand these sensitivities as due to competitive binding between A20 and CYLD to complex I coupled with differences in the rate constants for RIP1 deubiquitination by A20 (P19) and CYLD (P20; see Figure 13A). In other words, increasing the amount of A20 leads to increased amounts of A20-bound complex I (and vice versa). Since the rate constant for RIP1 deubiquitination in mode 1 by A20 is much larger than for CYLD (Figure 13A), this results in a significant decrease in TTD (i.e., increase in sensitivity to necroptosis). Conversely, increasing the amount of CYLD leads to more CYLD-bound complex I (and vice versa). Since CYLD is less efficient at deubiquitinating RIP1, this results in a much lower overall rate of RIP1 deubiquitination and a significant increase in TTD (decrease in sensitivity to necroptosis). Sensitivities to rate constants associated with these processes (P10, P11, P15–P19) can be explained similarly.

As in mode 1, potential targets in mode 2 include proteins, i.e., A20, CYLD, and LUBAC (Figure 15A, *second row*), and rate constants (P15–P20; Figure 16–*second row*

and Figure 14) associated with RIP1 ubiquitination regulation. The sensitivities to A20 and CYLD, however, are reversed in their effects on TTD as compared to mode 1, i.e., increasing A20 increases TTD, while increasing CYLD decreases TTD. Again, these results are consistent with *in silico* KO experiments (Figure 13B) and can be understood in terms of competitive binding between A20 and CYLD to complex I and differences in rate constants for RIP1 deubiquitination by A20 and CYLD (Figure 13A). Also note that TTD in modes 1 and 2 are sensitive to the rate constant for TNF degradation (P3; Figure 16–*top and second rows*), which is not unexpected since TNF is the stimulus driving necroptosis.

For mode 3, potential targets are associated with formation of the necrosome from complex IIb, which immediately precedes necroptosis execution (see Figure 7, *blue*). Specifically, we see sensitivities to proteins C8, RIP1, and TRADD (Figure 15–*third row*), the latter two of which are key components of complex II, and rate constants (P2–P6; Figure 16–*third row* and Figure 14) for reactions upstream of complex II that include the association of RIP1 and TRADD to complex I. Intuitively, the comparatively small value of the rate constant in mode 3 for degradation of C8a:FLIP-bound complex IIb (P34; see Figure 13A) what ultimately drives these sensitivities. Modifying rates of reactions that contribute to complex II formation and/or the rate of binding of C8i to complex II, alters the balance between the rates of necrosome formation and degradation of complex IIb that prevents necroptosis, thus affecting TTD. Also note, in contrast to modes 1 and 2, the lack of sensitivity in mode 3 to variations in the initial concentrations of A20 and CYLD.

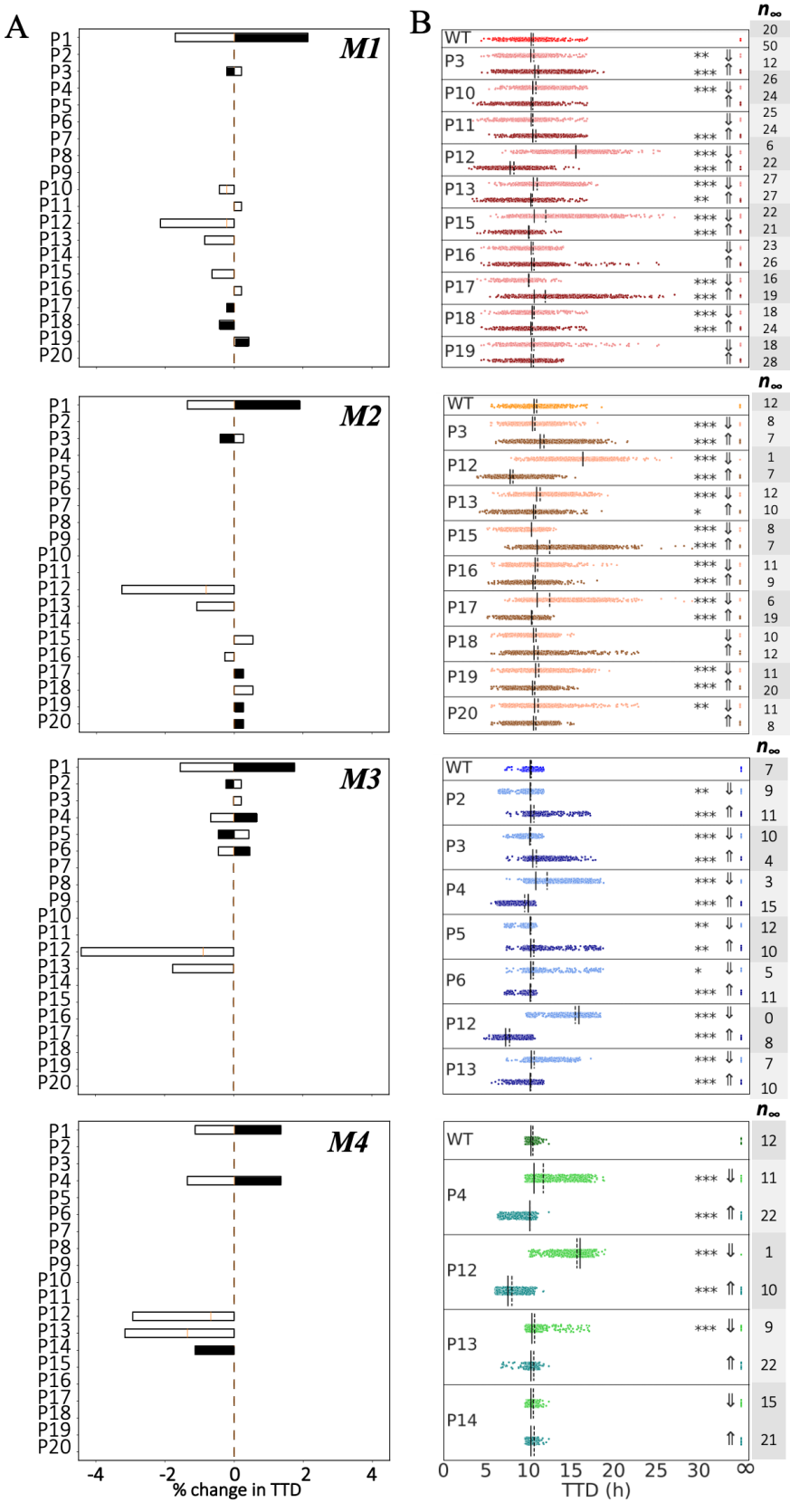
A
B
M1
M2
M3
M4
P1
P2
P3
P4
P5
P6
P7
P8
P9
P10
P11
P12
P13
P14
P15
P16
P17
P18
P19
P20
WT
-4
-2
0
2
4
% change in TTD
0
5
10
15
20
25
30
∞
TTD (h)

Figure 16: Sensitivity analyses and model-predicted rate constant targets for each mode of execution. (A) Changes in TTD for "representative" parameter sets of each mode. Black shaded regions signify decreases in rate constant values; white shaded regions signify increases. (B) Decreases (⇓; 10-fold) and increases (⇑; 10-fold) of potential targets identified in A for all parameter sets for each mode. The number of parameter sets that do not result in cell death (n_∞) are included. Solid black lines = medians, dashed black lines = means; * $p < 0.05$, ** $p < 0.01$, *** $p < 0.001$ (Mood's median test).

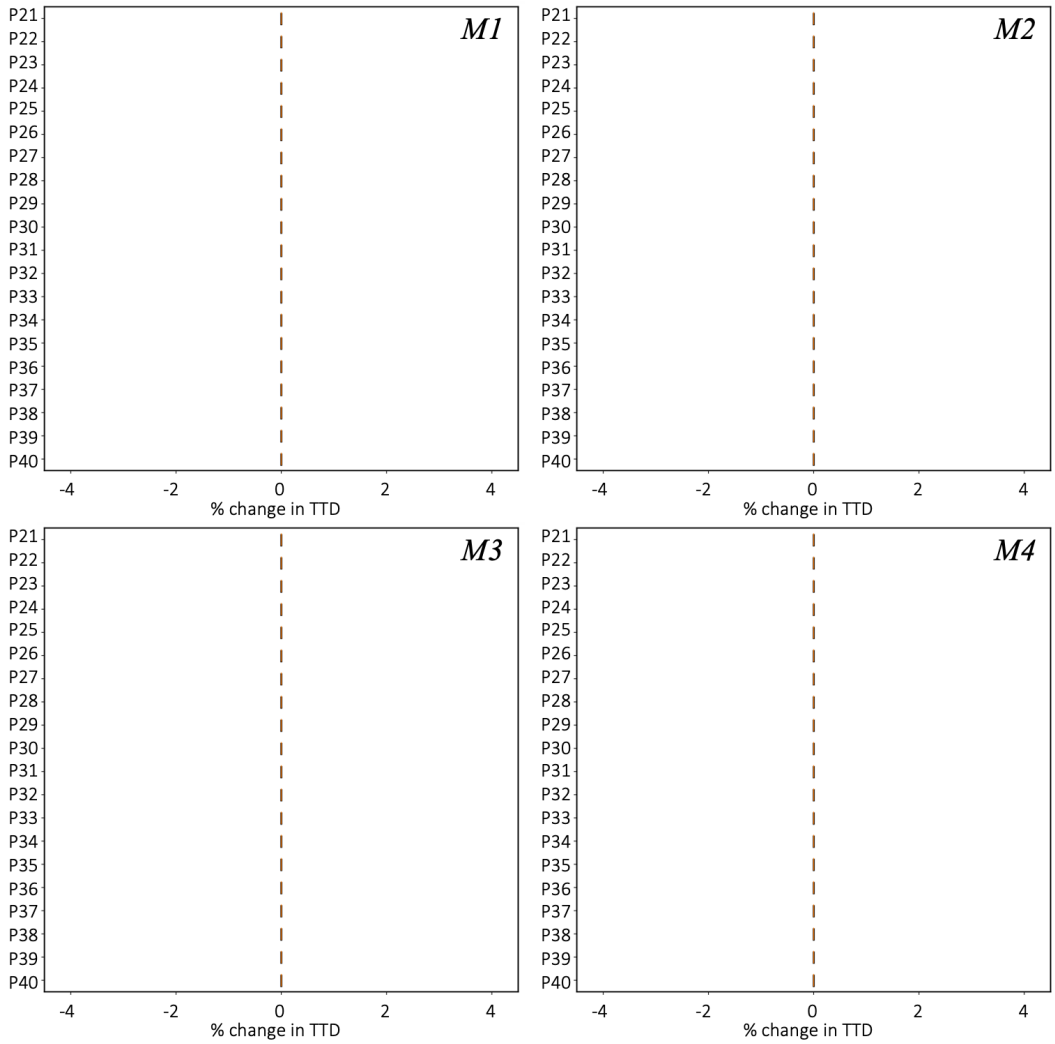

Figure 17: Rate constant sensitivity analyses show no sensitivity for parameters P21-P40 in any mode. Values were varied in a range ± 20% around the reference parameter set for each mode.

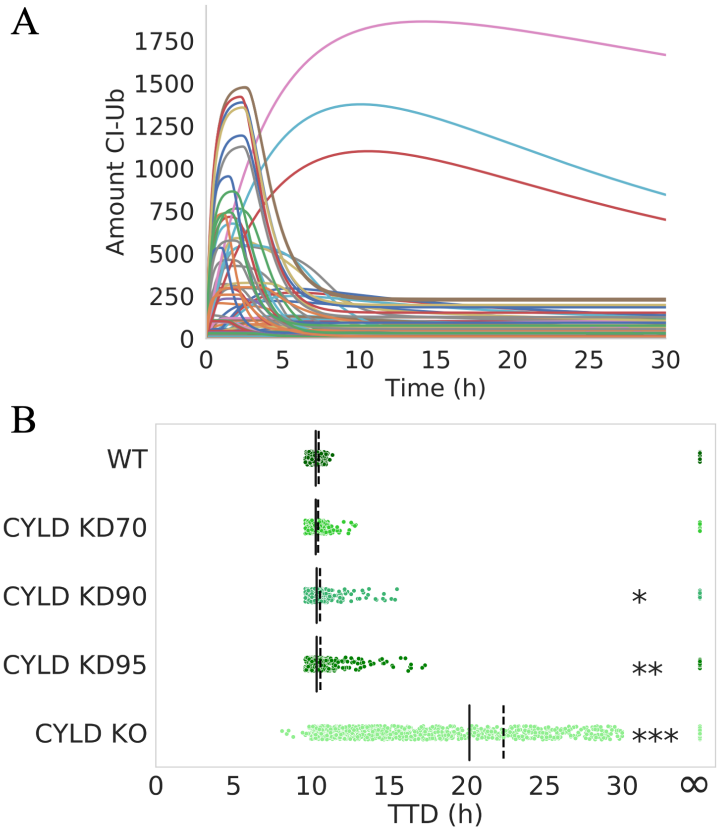

Figure 18: Dynamics in necroptosis execution mode 4. (A) Time courses for ubiquitinated complex I for all parameter sets in mode 4 show that CYLD (9,075 molecules; Table 7) is always in great excess. (B) TTD distributions over all parameter sets in mode 4 for CYLD knockdowns (KDs; 70%-95%) and knock out (KO), compared to wild-type (WT). Solid black lines = medians, dashed black lines = means; * $p < 0.05$, ** $p < 0.01$, *** $p < 0.001$ (Mood's median test).

This is because, in this mode, A20 and CYLD are effectively indistinguishable enzymes, i.e., rate constants for binding and unbinding from complex I (P15–P18) and RIP1 deubiquitination (P19 and P20) are virtually identical for both (Figure 13A). Thus, varying the concentration of one is effectively equivalent to varying the concentration of the other by the same amount.

In mode 4, we see the same sensitivities as in mode 3 to varying concentrations of C8, RIP1, and TRADD (Figure 15–*bottom row*) and the rate constant for association of TRADD to complex I (P4; Figure 16–*bottom row* and Figure 14). These sensitivities can be understood in the same way as in mode 3, in terms of the balance between necrosome formation and complex IIb degradation. However, we see an additional sensitivity in mode 4 to the initial concentration of LUBAC (Figure 15–*bottom row*). Interestingly, for the representative parameter set, this is evident for both increases and decreases in LUBAC concentration (Figure 15A–*bottom row*), but when all parameter sets are considered is only statistically significant for the KD experiments (Figure 16A–*bottom row*). Note also that the representative parameter set shows a sensitivity to the dissociation rate of LUBAC from complex I (P14; Figure 16A–*bottom row*) but the effect is not statistically significant when all parameter sets are considered (Figure 16B–*bottom row*). Furthermore, despite the results of *in silico* KO experiments that show RIP1 deubiquitination in mode 4 is driven exclusively by CYLD (Figure 13B), we do not see a sensitivity in TTD to variations in CYLD concentration, even for a 70% KD (Figure15–*bottom row*). We can explain both this result and the one-way sensitivity to variations in LUBAC as due to a severely dysfunctional A20 in mode 4, evident in exceedingly small rate constants for A20 binding to complex I (P15) and subsequent RIP1 deubiquitination

(P19), coupled with a comparatively large rate constant for C8 activation (P27) and small rate constant for C8 inactivation (P28; Figure 13A). Essentially, A20 does not compete with CYLD for binding to complex I (P15 $\ll$ P16), and since CYLD is in great excess relative to complex I (Figure 18A), varying CYLD concentration has little to no effect on TTD except for very large reductions, such as a KO (Figure 13B and Figure 18B). Moreover, the exceedingly fast rate of C8 activation (P28/P27 $\ll$ 1) leads to a rapid accumulation of active C8a:FLIP heterodimer, which inhibits necroptosis by binding and degrading complex IIb. This essentially sets a “speed limit” on the rate of pMLKL production, i.e., any increase in complex I concentration due to an increase in the concentration of LUBAC, which would be expected to decrease TTD because of the large excess of CYLD, is counteracted by the increased concentration of C8a:FLIP. However, decreasing complex I concentration by knocking down LUBAC would still be expected to increase TTD, as confirmed by our results.

Table 5: Multiple experimental studies of necroptosis in the literature can be associated with different model-predicted modes of execution. In the seconds column, the specific cell line used (if applicable) is included in parentheses. HCAC: human cervical adenocarcinoma; HCN: hippocampal neuron; HEK: human embryonic kidney; HTL: human T lymphocyte; MEF: mouse embryonic fibroblast; MFS: mouse fibrosarcoma. ⇓: decrease; ⇑: increase; ⇔: no change.

Reference	Cell type	Quote(s) from article	Interpretation	Possible execution mode(s)
Feoktistova et al. (2020)	HCAC (HeLa)	"[T]he deletion of A20 in HeLa or HaCaT cells had no effect on the TNF-mediated cell death sensitivity"	A20 ⇓ TTD ⇔	M3, M4
Hitomi et al. (2008)	HTL (Jurkat)	"[I]nhibition of CYLD expression in Jurkat cells also attenuated necroptosis"	CYLD ⇓ TTD ⇑	M2, M4
Liu et al. (2014)	HCN (HT-22)	"RIP1 and its deubiquitinase CYLD are required for TNF-induced necrosis of HT-22 cells"	CYLD ⇓ TTD ⇑	M2, M4
Moquin et al. (2013)	MEF	"CYLD regulates RIP1 ubiquitination in the TNFa-induced necrosome, but not in the TNFR-1 signaling complex" "Although CYLD was recruited to TNFR-1 in a ligand-dependent manner, RIP1 ubiquitination was not affected in CYLD$^{-/-}$ MEFs"	CYLD ⇓ TTD ⇑	M4 (M2 excluded; see text)
Vanlangenakker et al. (2011)	MFS (L929)	"[W]e and others previously showed that CYLD repression protects L929 cells from TNF-induced necroptosis" "[W]e were surprised to find that A20 depletion had an opposite effect and greatly sensitized the cells to death" "[W]e found that TRADD depletion in L929 cells did not affect TNF-induced necroptosis"	CYLD ⇓ TTD ⇑ A20 ⇓ TTD ⇓ TRADD ⇓ TTD ⇔	M2
Wertz et al. (2004)	HEK (HEK293T)	"Co-transfection of wild-type A20 de-ubiquitinates RIP in HEK293T cells."	A20 ⇓ TTD ⇑	M1
Wertz et al. (2004)	MEF	"However, in the absence of A20, RIP1 will neither be de-ubiquitinated nor targeted for proteasomal degradation. Indeed, RIP recruited to activated TNFR1 remained hyperubiquitinated and was stabilized in A20$^{-/-}$ MEFs"	A20 ⇓ TTD ⇑	M1
Wright et al. (2007)	HCAC (HeLa)	"RIP1 ubiquitination [was] inhibited by wild-type (Wt) CYLD but not a catalytically inactive CYLD mutant (Mut)"	CYLD ⇓ TTD ⇑	M2, M4

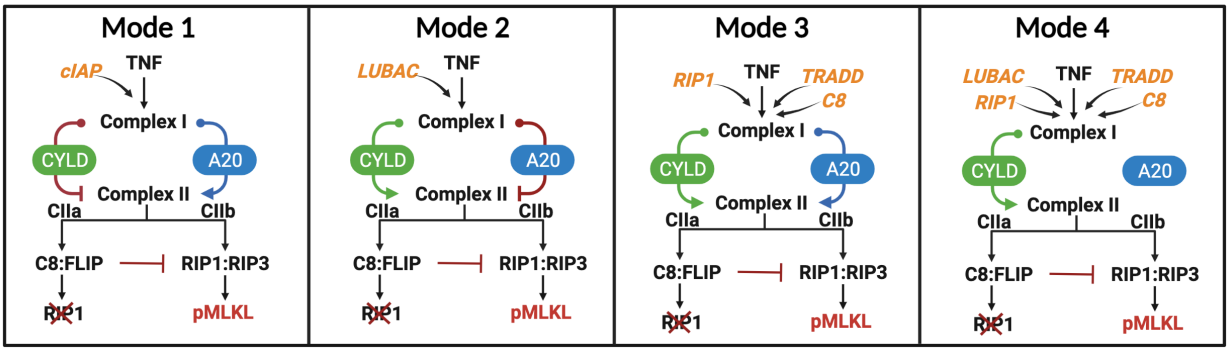

Figure 19: Four modes of execution in necroptosis. Schematic depiction of each mode of execution identified presenting distinct differences in initial protein sensitivity (orange), RIP1 ubiquitination regulation by CYLD (green) or A20 (blue), inhibition (red bar line), and parameter sensitivity influencing pro- or anti- necroptotic responses.

DISCUSSION

A recent review of TNF-induced necroptosis (Samson et al., 2021) described signaling along the RIP1-RIP3-MLKL axis in terms of at least three major compartmentalization events: TNFR internalization in complex I, multiprotein assembly of complexes IIa and IIb, and necrosome formation leading to translocation of pMLKL to the membrane. Importantly, the authors emphasized that cues and regulation mechanisms underlying these compartmentalization events are poorly understood and proposed that a network of modulators surrounds the necroptotic signaling core (Murphy et al., 2013; Najafov et al., 2019; Sai et al., 2019), tuned in a context-, cell type-, and species-dependent manner. The results presented here are entirely consistent with this view, i.e., a detailed kinetic model comprising core and complementary necroptotic signaling proteins and associated rate constants (Table 1 and Figure 7), calibrated to experimental data (Figure 8A–C), can produce cell-death dynamics via distinct execution modes (Figure 12A,B), distinguished by variations in rate constants (Figure 13A) and the roles of A20 and CYLD in RIP1 ubiquitination regulation (Table 5 and Figure 13B). Moreover, model sensitivity analyses based on TTD (Figure 8D) revealed global and mode-specific modulators of necroptosis sensitivity for each mode (Figures 15 and 16). Global modulators include known effectors, such as TNF, TNFR, MLKL, and rate constants associated with these proteins, as well as two unexpected modulators: the rate constant for RIP1 ubiquitination by cIAP in complex I (P12) and the binding rate constant for LUBAC to complex I (P13). Mode-specific modulators include, for modes 1 and 2, proteins and rate constants involved in RIP1 ubiquitination regulation (A20, cIAP, CYLD, LUBAC, P10, P11, P15–P20) and, for modes

3 and 4, factors regulating the balance between complex IIb degradation and necrosome formation (C8, LUBAC, RIP1, TRADD, P2–P6, P14, P27, P28).

Since evading apoptosis is a hallmark of cancer (Hanahan, 2022; Hanahan and Weinberg, 2000, 2011), inducing necroptosis is currently being explored as a potential anticancer treatment (Gong et al., 2019; Meng et al., 2016; Wu et al., 2020). Moreover, inhibiting necroptosis is crucial for treating a variety of inflammatory diseases, including cardiovascular, liver, and neurodegenerative diseases (Choi et al., 2019; Vanlangenakker et al., 2012). Thus, improving our understanding of the molecular pathways that drive necroptosis is critical for identifying novel therapeutic targets against these deadly diseases. The detailed kinetic model of TNF-induced necroptosis proposed in this work represents the first successful attempt to describe contrasting, and sometimes counterintuitive, context-, cell type-, and species-dependent responses to cell-death cues using a consensus set of biochemical interactions deduced from decades of experimental work. This is a significant contribution that advances our knowledge of necroptosis and also provides a foundation for future *in silico*-guided drug discovery efforts. Altogether, the model presented in this study is a significant step towards the construction of a comprehensive computational model of the interconnected pathways controlling cell fate decisions, which could lead to the development of novel therapies against inflammatory diseases and cancer by enabling identification of molecular targets that shift the balance of fates towards either evasion or promotion of necroptosis.

CHAPTER III

III. ELUCIDATING THE ROLE OF NOTCH SIGNALING IN SMALL CELL LUNG CANCER

INTRODUCTION

Tumor heterogeneity and molecularly characterizing the subtypes of SCLC

Small Cell Lung Cancer (SCLC) has become a hot topic in the last few years given the aggressiveness of the disease, lack of therapeutic treatment options, and poor prognosis outcomes. SCLC is a high grade neuroendocrine (NE) carcinoma that has been characterized as a “homogeneous” disease by its histology, which generally presents as a carpet of small round cells with little cytoplasm (Ko et al., 2021). There have been many scientific advances to molecularly characterize this cancer, however the lack of effective biomarkers to guide treatments has remained a persistent problem (George et al., 2015; Ko et al., 2021). The median overall survival from extensive SCLC is less than 10 months, with less than 5% of patient survival after five years. The standard care of treatment for SCLC, which has not changed, encompasses a combination of etoposide and carboplatin/cisplatin chemotherapy (Sundstrøm et al., 2002). Although clinically, SCLC is still regarded as a single disease entity (Gazdar et al., 2017; Ko et al., 2021), preclinical studies from past decades identified biologically different SCLC subgroups (Figure 20).

SCLC was originally classified into “classic” and “variant “ phenotypes in 1985 (Carney et al., 1985), based on the *in vitro* and *in vivo* behavior of SCLC cells. The “classic” phenotype was associated with high expression of NE markers, and non-adherent growth pattern in cell cultures (Gazdar et al., 1985; Schwendenwein et al., 2021). In contrast, the “variant” phenotype was characterized by larger cells, low

expression of NE markers, and an adherent or loosely adherent growth pattern *in vitro* (Dora et al., 2020; Gazdar et al., 2017). In the last decade, SCLC has been recently classified into NE and non-NE (non-neuroendocrine) subtypes (Rudin et al., 2019; Wooten et al., 2019). Transcriptomic profiling has defined possible drivers of NE and non-NE SCLC, where the classic NE subtype of SCLC has been further divided by expression of two transcription factors, ASCL1 (achaete-scute homologue 1) and NEUROD1 (neurogenic differentiation factor 1), which appear to regulate distinct neuroendocrine gene programs (Borromeo et al., 2016a; Poirier et al., 2013). Variant non-NE SCLC tumors are low in ASCL1 and NEUROD1. More recently, the phenotypic heterogeneity of SCLC has become defined by differential expression of four key transcriptional regulators: NE markers, ASCL1, and NEUROD1, with non-NE markers, POU2F3 (POU class 2 homeobox 3) and YAP1 (yes-associated protein 1; (Huang et al., 2018; Rudin et al., 2019; Wang et al., 2021). Furthermore, with the most recent classification of these subtypes, a deeper understanding of the SCLC molecular anomalies has led to a wave of novel targetable agents including the identification of the Notch pathway and its deregulation as a crucial event in SCLC tumorigenesis, disease progression and chemoresistance (Crabtree et al., 2016; Ireland et al., 2020; Leonetti et al., 2019).

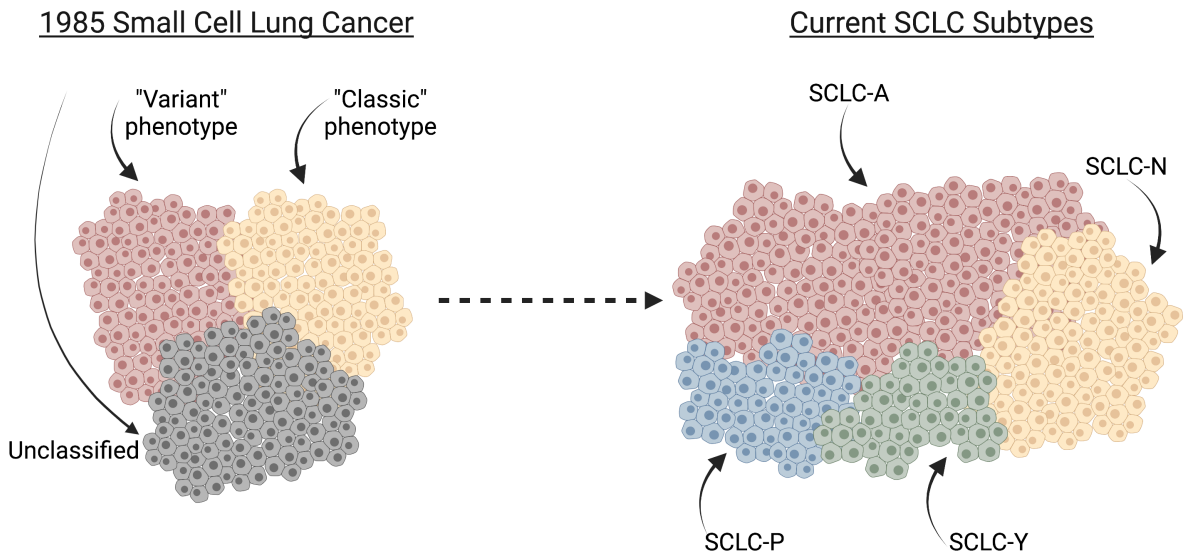

Figure 20: Tumor heterogeneity in SCLC over the years. Historic classification of SCLC in 1985, phenotypically made up of “classic,” “variant,” and unclassified cells (left). Current SCLC is distinguished by four subtypes: SCLC-A, SCLC-N, SCLC-P, and SCLC-Y, characterized by key markers within each population from SCLC cells.

Notch signaling: cell fate control and signal integration in development

The Notch signaling pathway through direct cell-to-cell communication between neighboring cells regulates cell proliferation, cell fate, differentiation and cell death during development (Hori et al., 2013). In mammalian systems, Notch activation is known to promote cancer development, while it can also play a tumor suppressive role (Ayaz and Osborne, 2014; Ntziachristos et al., 2014). The Notch signaling pathway is triggered by the interaction of four Notch receptors (Notch 1–4), three Delta-like ligands, DLL1 (Delta Like Canonical Notch Ligand 1), DLL3 (Delta Like Canonical Notch Ligand 3), DLL4 (Delta Like Canonical Notch Ligand 4), and two ligands of the Jagged family JAG1 (Jagged 1), and JAG2 (Jagged 2; Sprinzak and Blacklow, 2021). The binding of the receptor to its ligand can occur between different cells (trans-interaction) or within the same cell (cis-interaction), leading to either activation or inhibition of the transducing signal, respectively (Miele, 2006). DLL3 is the only ligand that binds to its Notch receptor through a cis-interaction, an uncharacteristic inhibitory effect in regulating the signaling cascade of interactions (Owen et al., 2019). When membrane bound receptors interact with ligands on an adjacent cell, two consecutive proteolytic cleavages of the receptor are initiated, freeing the intracellular portion of Notch to enter the nucleus and activate the transcription of target genes. The first cleavage (S2) by ADAM10 (A disintegrin and metalloprotease 10) generates the substrate for the second cleavage (S3) by the γ-secretase complex (Hori et al., 2013). The second cleavage releases the NECD (Notch extracellular domain) that gets endocytosed by the neighboring cell bound to its ligand while the NICD (Notch intracellular domain) translocates to the nucleus and forms a complex including RBPJ (Recombination Signal Binding Protein For Immunoglobulin Kappa J Region) and MAML1

(Mastermind-like transcriptional co-activator 1), stimulating transcription of target genes (Figure 21) (Hori et al., 2013) including but not limited to, REST (RE1 Silencing Transcription Factor), HES1 (Hes Family BHLH Transcription Factor 1), MYC (Myelocytomatosis), and HES6 (Hes Family BHLH Transcription Factor 6).

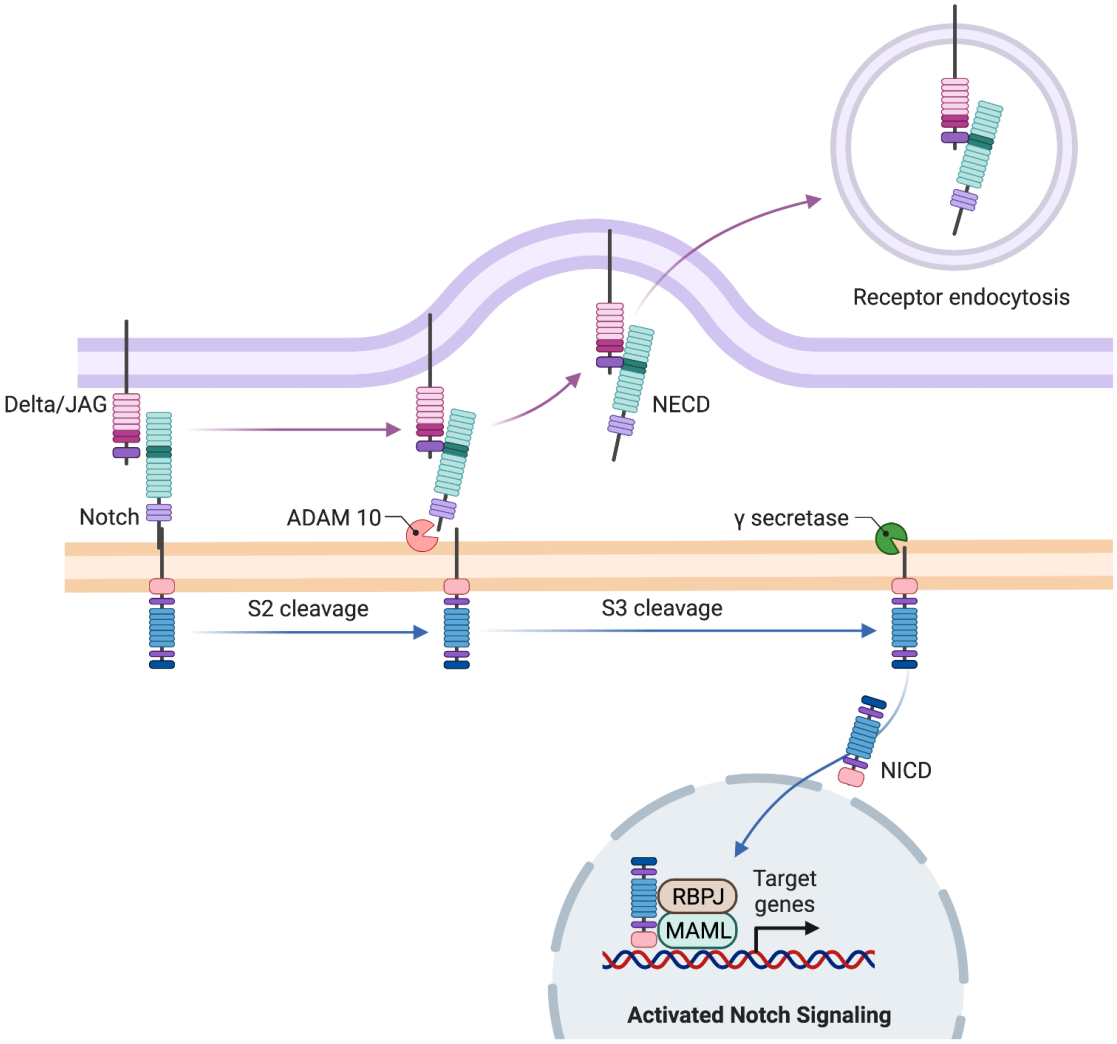

Figure 21: The core Notch pathway. Binding of the Delta ligand (pink) on one cell to the Notch receptor (green) on another cell results in two proteolytic cleavages of the receptor. ADAM10 (A disintegrin and metalloprotease 10, red) catalyzes the S2 cleavage, resulting in the release of the NECD (Notch extracellular domain) that is endocytosed into the neighboring cell bound to its ligand. The S2 cleavage also generates a substrate for S3 cleavage γ-secretase (green). This proteolytic processing mediates release of the NICD (Notch intracellular domain), which enters the nucleus and interacts with the DNA-binding co-activator Mastermind like-1 (MAML1; green) and other transcription factors.

Role of Notch in SCLC subtype determination and plasticity

During normal lung development, Notch pathway activation prevents cells from differentiating to a neuroendocrine fate, and promotes the trans-differentiation of Pulmonary neuroendocrine cells (PNECs) into non-neuroendocrine club cells (Ouadah et al., 2019). “Phenotypic plasticity” is the ability of a single genotype to produce more than one alternative form of morphology, physiological state, and/or behavior in response to environmental conditions (West-Eberhard, 1989, 2008). Organisms employ mechanisms of environmental assessment that enable behavior to be adaptively plastic, that is, supportive of individual reproductive success in which Notch pathway activation is hypothesized to play an important role. In cancer, Notch is considered to be both tumor suppressive and oncogenic, depending on the context (Hori et al., 2013; Ntziachristos et al., 2014). In SCLC, Notch1–4 are mutated in ~25% of human tumors, and a large subset of those mutations are inactivating (George et al., 2015). This is consistent with Notch acting as a tumor suppressor, as Notch signaling in SCLC has been shown to induce cell cycle arrest (Sriuranpong et al., 2001). Similar to normal development, Notch signaling is generally suppressed in NE subtypes of SCLC, which are fast growing and chemosensitive. Recent data from (Lim et al., 2017) showed that Notch signaling can also be pro-tumorigenic, by inducing a fate switch from NE to this slower-growing but chemoresistant non-NE subtype. Using a $p53^{fl/fl}$;$Rb^{fl/fl}$;$Rbl2^{fl/fl}$ conditional triple knockout (RPR2) SCLC mouse model, green fluorescent protein (GFP) was expressed from the endogenous *Hes1* promoter to measure Notch pathway activation. Both *Hes1*-positive GFP^{high} cells, which expressed non-NE and mesenchymal markers, and *Hes1*-negative GFP^{neg} cells, which expressed NE genes, were found in the tumors. Non-NE $Hes1^{pos}$ cells

were shown to arise from an NE cell of origin, and the transition from NE to non-NE could be induced with Dll4. While *Notch1* is expressed in some SCLC subtypes, blockade of just *Notch2/3* was sufficient to prevent this transition. Although GFP^{neg} cells were much faster growing than GFP^{pos} cells, and thus should rapidly outcompete them in tumors, the presence of both cell types within individual tumors suggested association between them. $Hes1^{pos}$ cells were shown to promote the growth of NE cells, while Notch ligands such as Dll4 on NE cells could promote the transition to the non-NE phenotype. Consequently, deregulation of Notch signaling has differential effects across cell types, by either turning on or turning off a variety of downstream genes at early or late stages of cancer development (Figure 22). Notably, Hes1 is a transcriptional repressor of ASCL1, which has a critical function in NE cell development and differentiation of lung epithelial cells (Westhoff et al., 2009). ASCL1 is known for its importance in the development of normal PNECs, which are the precursors of SCLC tumor initiating cells. This pro-tumorigenic relationship between NE and non-NE cells suggests a functional role for heterogeneity in SCLC driven by the Notch pathway.

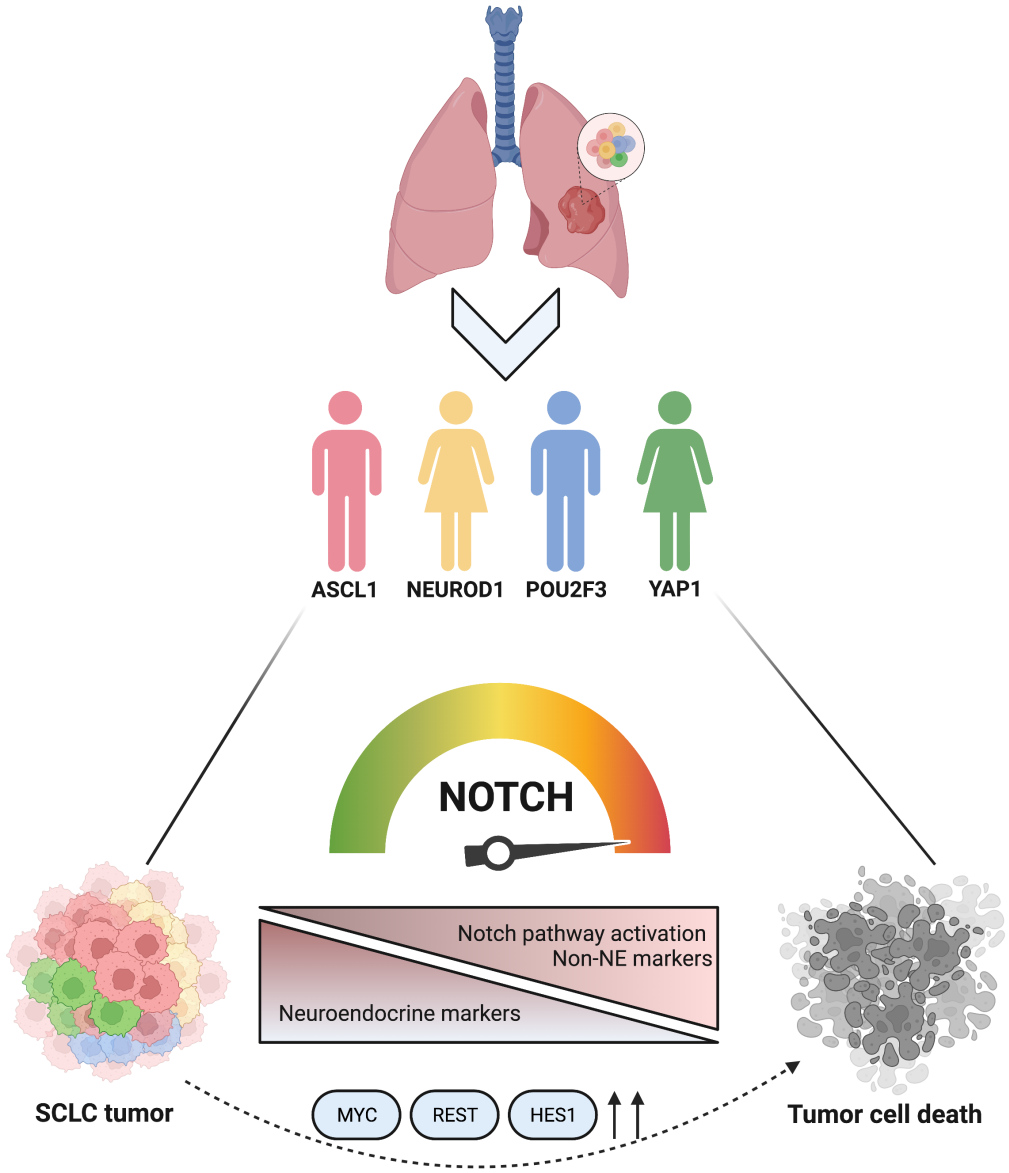

Figure 22: Notch and Small cell lung cancer subtypes. A schematic of an SCLC tumor in the lung, made up of ASCL1^{+}, NEUROD1^{+}, POU2F3^{+}, and YAP1^{+} cells progressing in the presence of Notch pathway activation markers to tumor cell death including increased expression of MYC, REST, and HES1 and decrease neuroendocrine markers.

Notch pathway, MYC, and the SCLC-N to -Y transition

Recent studies have shown that MYC (MYC Proto-Oncogene, BHLH Transcription Factor) may also play a role in driving SCLC phenotype transitions through activation of the Notch pathway. In particular, a transition from SCLC-A to -N to -Y has been shown to occur in a MYC-driven ($p53^{fl/fl}$;$Rb^{fl/fl}$; Lox-Stop-Lox [LSL]-Myc^{T58A}, RPM) mouse model of SCLC (Ireland et al., 2020). RPM tumors *in vivo* showed early-stage lesions have high levels of NE markers, including ASCL1, while late-stage invasive tumors are positive for non-NE markers such as NEUROD1, YAP1, and Notch proteins such as HES1. Single cell transcriptomic analysis of a time course of RPM tumor cells *in vitro* demonstrated that MYC can promote non-NE subtype evolution from earlier NE cells. Interestingly, multiple Notch pathway genes are MYC targets, such as Notch2, Hes1, Hes6, and Jag2. Consistent with this, Notch pathway genes are enriched as cells transition from SCLC-A to -Y, suggesting a possible role for the Notch pathway in this subtype evolution. For example, Dll3 and Hes6, which inhibit Notch pathway activity, were expressed early in the transition, while Hes1, Rest, and Notch2 increase in expression over time. Ectopic MYC overexpression in classic MYCL-high (NE) cell lines and RPR2 tumors induced variant, non-NE morphology and Notch receptor expression. The role of Notch was further validated by a Notch signaling inhibitor (gamma secretase inhibitor, DAPT), which delayed transitions from NE to non-NE subtypes in the time course, suggesting Notch activation is an important step in MYC-driven subtype evolution.

Differential activity driven by diversity of Notch ligands and receptors

The Notch signaling pathway regulates a diverse array of cell types and cellular processes and is tightly regulated by ligand binding (D'Souza et al., 2008). The diversity

of Notch receptors and ligands, raises the question of how downstream signaling is affected by the types of receptors and ligands, as well as by modulating proteins (Figure 23; Sprinzak and Blacklow, 2021). Cellular context and tissue distribution are also added layers of *in vivo* complexity that further contribute to differences in activity and functional output. Several studies have attempted to quantify the affinity of various mammalian Notch receptors for Delta-like and Jagged ectodomain fragments using a variety of biochemical methods (Tveriakhina et al., 2018). There are intrinsic differences in the affinity of different Notch receptors for the two major Delta-like ligands, Dll1 and Dll4, with Notch1 favoring Dll4 by an order of magnitude and Notch2 favoring Dll1 by roughly threefold (Andrawes et al., 2013; Tveriakhina et al., 2018). There are also similar intrinsic affinity of Notch1 for both Dll1 and Jag1 (Taylor et al., 2014). In addition, cell-based and biochemical analysis showed that Dll1 and Dll4 differentially activate Notch1 and Notch2, with Notch1 activated more strongly by Dll4 and Notch2 activated more strongly by Dll1 (Figure 23; Mohtashami et al., 2010) consistent with previous studies. Furthermore, Dll4, Jag1, and Jag2 have been shown to preferentially bind with Notch3 (Indraccolo et al., 2009, Pelullo et al., 2014, Sasnauskiene et al., 2014), and Notch4 (Claxton and Fruttiger, 2004; Pedrosa et al., 2015; Sasnauskiene et al., 2014). Potential differences in activity may come from the observed differences in binding affinities between receptors and ligands, as well as from other differences on the ligand side, including modulation of ubiquitination and endocytosis (Sprinzak and Blacklow, 2021). Another recent study investigated the differences in activity between Dll1 and Dll4 using live cell imaging to track the dynamics of a Notch1 transcriptional reporter in response to activation by sender cells containing either Dll1 or Dll4 (Nandagopal et al., 2018). Interestingly, this study found

that activation by Dll1-expressing cells led to a pulsed transcriptional response, while activation by Dll4 led to a sustained transcriptional response in the receiving cells. In contrast, DLL3 is the only ligand that binds and inactivates the Notch receptor pathway through a *cis*-interaction, thus promoting SCLC tumorigenesis (Leonetti et al., 2019). DLL3 is responsible for retaining Notch and DLL1 in the Golgi apparatus, preventing their localization to the cell surface and subsequent cross interactions (Chapman et al., 2011; Owen et al., 2019).

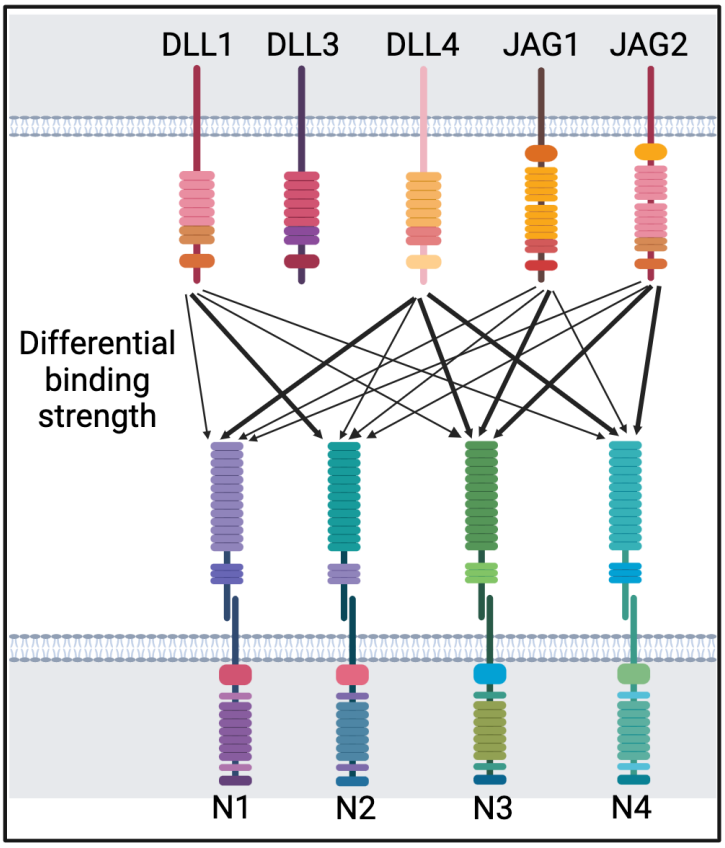

Figure 23: Diversity of receptor–ligand interactions. Schematic showing the factors affecting the strength of Notch signaling for different receptors, ligands, and regulator modifications. Differential binding is depicted by arrows, where the thickness of the arrows represents the binding strength (the thicknesses drawn are only schematic and do not necessarily represent actual binding strength). Note that DLL3 does not trans-activate Notch receptors.

Although unique ligand–receptor combinations have been identified that induce specific cellular responses, the molecular mechanisms underlying ligand-specific signaling remains an outstanding question in the field. Moreover, given the direct and somewhat simple signaling mechanism attributed to Notch, it is unclear how different Notch ligands could induce distinct signaling responses. It is important to determine if different ligand–Notch complexes recruit unique signaling effectors and whether the distinct responses involve activation of cytoplasmic and/or nuclear signaling pathways. Ligands have intrinsic signaling activity independent of Notch as well as their potential to participate in bidirectional signaling are interesting but relatively unexplored areas of ligand biology that warrant further investigation. The importance of Notch ligands in cancer and other pathological states involving aberrant angiogenesis has identified Notch ligands as potential and promising therapeutic targets (Lobov et al., 2007; Roca and Adams, 2007; Sainson and Harris, 2008; Yan and Plowman, 2007). The use of Notch ligands in the expansion and maintenance of stem cells for tissue regeneration/replacement underscores their fundamental biological importance (Dallas et al., 2005; Delaney et al., 2005). Finally, it is important to emphasize these emerging findings to continue developing Notch-based therapeutics that could be used efficiently in patients with immune and inflammatory diseases.

Applying geometric methods to study tumor diversity in cancer

Recent advances have enabled powerful methods to sort tumors into prognosis and treatment groups. While the ability to sort tumors is powerful and useful, there remains an open question of understanding, from a theoretical perspective, why tumors vary in the way that they do. To address this, Hausser et al. (Hausser et al., 2019) applied a

theory of multitask evolution, known as Pareto task inference (ParTI), to cancer. They reasoned that cancer is a case of intense evolution inside the body, and cancer cell growth and survival are conditioned on fulfilling multiple tasks, including stress resistance, growth, and interactions with the immune system (Hanahan, 2022; Hanahan and Weinberg, 2011). Each task then requires a different profile of gene expression, with the presumption that no tumor can be optimal at all tasks at once, because cells are limited in their protein production and timing of different functions (Gillies et al., 2012). Thus, the idea is that if cell communities that optimally manage the trade-off relevant for their particular niche function in the body they will outgrow and out-survive cells that are only suboptimal. Growth and survival are only two of the possible tasks that affect tumor cell fitness. This raises the question of how can we detect and understand trade-offs between three and more tasks and identify tasks without assuming they previously existed? Using the fact that tumors need to perform multiple tasks to contribute to their fitness, they found that trade-offs between tasks constrain tumor gene-expression to a continuum bounded by a polytope whose vertices are gene expression profiles, each specializing in one task (Cook and Wrana, 2022; Hausser et al., 2019). This approach can integrate additional types of molecular data into a framework of tumor diversity grounded in evolutionary theory. This is represented geometrically (Figure 24). Consider selection performance at two tasks: in this phenotypic trait space, each task has a single point that represents the phenotype with optimal performance for that task (archetypes). As the phenotypes deviate from this point, the task performance is proposed to decline following a contour function around the archetype. Pareto optimal phenotypes in this two-task example system would those spanning the line connecting the two archetypes (Figure 24A). This

region containing the Pareto optimal phenotypes is referred to as the “Pareto font,” and its geometry can extend to systems with any number of tasks (Figure 24B). “Specialist” phenotypes are those that prioritize performance of a single task, adopting a state with high similarity to an archetype. A “Generalist,” however, exhibits trade-offs to balance performance of multiple tasks, where its phenotype exists within the Pareto front but remains distant from individual archetypes (Figure 24C). A population of generalists can also be highly heterogeneous, with the specific performance trade-offs varying throughout the population. These principles of multitask optimization and Pareto optimality provide a framework to interpret cellular phenotypes.

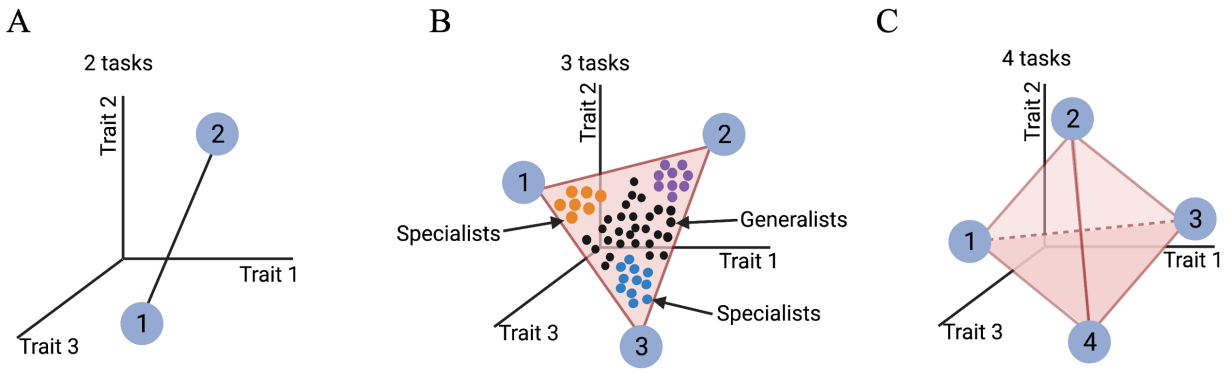

Figure 24: Geometric properties of the Pareto front. (A) Two tasks form a line, and when under selection for more than one task, the Pareto front represents the phenotypes with optimal performance trade-offs. (B) Populations under selection for more than two tasks span a polytope connecting archetypes where Specialist phenotypes show bias towards individual tasks, while generalists exhibit trade-offs to balance performance at many tasks (C) Polytope with four vertices representing connecting archetypes.

SUMMARY

Studies have shown that activation of Notch signaling during SCLC progression generates an unexpected level of tumor heterogeneity (Rubin et al., 2020), and that Notch signaling is required for the NE to non-NE fate switch (Lim et al., 2017), however the exact mechanism of action is not well understood. The Notch pathways is composed of ligands (Jagged 1 & 2 and Delta-like homologues 1 & 4) and receptors (Notch 1–4). The diversity of Notch ligands and receptors raises questions of how downstream signaling is affected by the types of receptors and ligands, as well by modulating proteins (Sprinzak and Blacklow, 2021). The hypothesis is that there is an underlying combinatorial complexity between the Notch ligands and receptors that is responsible for the diversity of responses that could explain the role Notch plays in SCLC. Beyond these recent findings, the functional interactions between Notch pathway activity and the transcriptional regulators defining the four subtypes of SCLC remain to be investigated. We recently applied a systems approach using Archetype Analysis on bulk transcriptomics data from SCLC, composed of NE and non-NE subtypes and found that the subtypes fit well in a 5-dimensional polytope, proposing the vertices specialize in task trade-offs among specialists (A, A2, N, P, Y) and generalists cells (Groves et al., 2021). Dynamics of Intratumoral heterogeneity are especially relevant for SCLC, since cooperativity and transitions among SCLC subtypes have been postulated to underlie its recalcitrant features, i.e., early metastatic spread, and inevitable relapse after therapy response (Ireland et al., 2020; Lim et al., 2017; Rudin et al., 2019). This analysis was performed on numerous datasets including the bulk transcriptomics, SCLC tumors, and SCLC single cells to better understand SCLC heterogeneity and plasticity. Here, we expanded this

analysis to investigate Notch signaling within these archetypes and how pathway activation is regulated in specialist and generalist populations within SCLC and find that Notch signaling is distinctly differentiated across different scales (tumors, bulk transcriptomics, single cell transcriptomics) within archetype specialists and generalists.

RESULTS

SCLC tumors are composed of distinct Notch pathway expression profiles in specialist and generalist cells

Previous studies have demonstrated that SCLC cells transition between SCLC-A (NE) and, SCLC-Y (non-NE) subtypes under certain perturbations, such as Notch pathway activation (Lim et al., 2017) and MYC hyperactivation (Ireland et al., 2020; Patel et al., 2021). In these studies, classical neuroendocrine (NE) cells, such as SCLC-A, -A2, and -N, acquire non-NE properties including variant morphology and expression of non-NE markers (such as YAP1 or POU2F3). In particular, a transition from SCLC-A to -N to -Y has been shown to occur in a MYC-driven ($p53^{fl/fl}$;$Rb^{fl/fl}$; Lox-Stop-Lox [LSL]-Myc^{T58A}, RPM) mouse model of SCLC (Ireland et al., 2020). RPM tumors *in vivo* showed early-stage lesions have high levels of NE markers, including *ASCL1*, while late-stage invasive tumors are positive for non-NE markers such as *NEUROD1*, *YAP1*, and *NOTCH* proteins such as *HES1*. This study revealed the importance of Notch signaling in the NE to non-NE transition, however, they did not examine all components of the Notch signaling pathway within these tumors. To understand the comprehensive role of Notch signaling within these RPM tumors over the 21 day time-course (Figure 25A), we investigated the expression of Notch ligands, receptors, downstream targets, and inhibitors (Augert et al., 2019; Dai et al., 2013; Furuta et al., 2019; Hurtado et al., 2019; Tiberi et al., 2012; Xie et

al., 2012) previously shown to play inhibitory roles in Notch signaling activation. Importantly, with our recent classification that these SCLC cell lines and tumors comprise continuums of cell states with both specialists and generalists (Groves et al., 2021), we were interested to explore the role of Notch within these specialist and generalist cells.

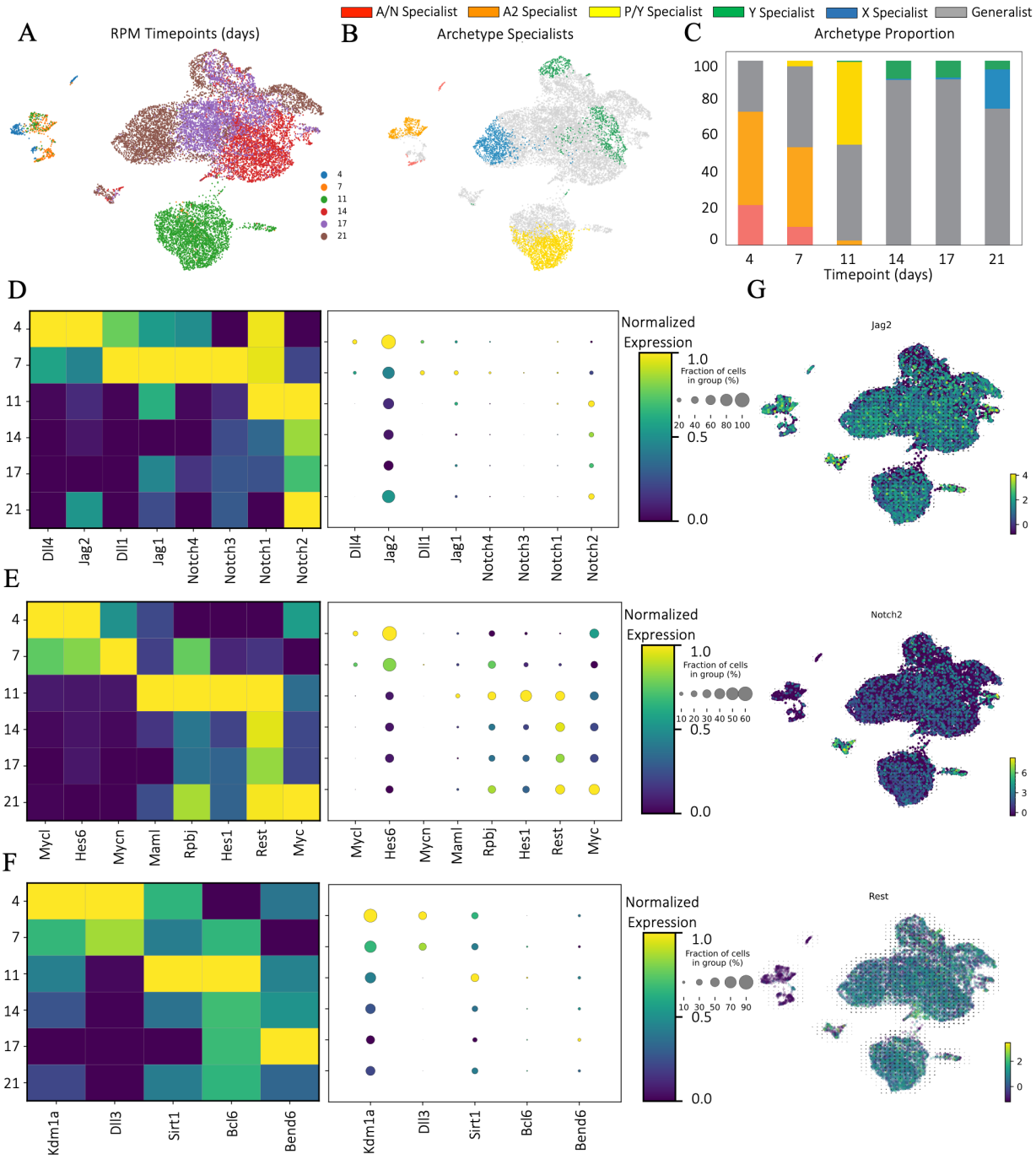

Figure 25: Notch initiation and activation is differentially expressed within GEMM tumor progression. (A) UMAP of RPM time course with timepoints labeled. Days 4 and 7 fall in the same region of the UMAP; Day 11 is mostly distinct; and Days 14-21 fall in the same large cluster. (B) Bulk archetype signature scores for single cells in time course. Days 4 and 7 are enriched in SCLC-A, -A2, and -N archetype signatures; Day 11 is moderately enriched for SCLC-P and -Y signatures; and a subpopulation of Days 14 to 21 is enriched in the SCLC-Y signature. (C) Stacked bar plots show overall subtype composition change from (*B*). (D-F) Cluster maps of Notch ligands and receptors across time course (D), Notch downstream targets (E), and Notch inhibitors (F). (G) UMAP of

JAG2, NOTCH2, *REST* highlighting the upregulated expression in late timepoint generalist cells.

The previously identified subtypes were aligned with the bulk archetypical signatures and found that a six-vertex polytope best fit the data, with 5 of the 6 archetypes enriched for SCLC signatures (Materials and Methods, Chapter IV), suggesting a multi optimization of tasks may have a role in this time course (Groves et al., 2021). As expected, there was a shift from NE subtype cells to non-NE with distinguished proportions of specialist and generalist cells (Figure 25B, C). Within the early timepoints (days 4 and 7), tumors were largely composed of specialist SCLC-A/-N, and SCLC-A2 specialists (> 50%), thought to form a continuum of specialists and generalists near these NE archetypes. Interestingly, *DLL4* and *JAG2* are highly expressed in day 4, while *DLL1* and *JAG2* are highly expressed in day 7 in comparison (Figure 25D, *left*). However, when we look closely at the fraction of cells (%) in each group, *DLL1*, *DLL4*, and *JAG1* make up only about 20% of the cells in these timepoints, and *JAG2* expression is the only ligand representing more than 50% of the cells in the early timepoints (Figure 25D, *right*) suggesting *JAG2* could be preferentially responsible for Notch receptor activation in earlier timepoints. Additionally, looking at the Notch receptors, there is minimal expression in day 4 except for *NOTCH1*, while *NOTCH3* and *NOTCH4* are only expressed in day 7, with very low to no expression of *NOTCH2* in the early SCLC-A/-N, and SCLC-A2 specialist archetypes. When we look at the fraction of cells expressing these Notch receptors, less than 10% of the cells across all four receptors are present in these tumors. Additionally, the downstream targets and inhibitors involved in Notch signaling including the Notch activating complex (*MAML, RBPJ*), and Notch targets

(*HES1, REST*) all show low expression, consistent with *NOTCH 1–4* also showing low expression with the inability to activate its downstream targets.

Subsequently, when examining Notch inhibitors, we see high expression of *KDM1A* (*LSD1*), an inhibitor of Notch signaling, recently shown to epigenetically suppress the expression of NOTCH1 (Augert et al., 2019), and DLL3, an inhibitory ligand of Notch, regulated by ASCL1 (Owen et al., 2019) in early timepoints of SCLC-A/N and SCLC-A2 specialists providing an rationale for why Notch expression is lower in the earlier timepoints (Figure 25F). *HES6*, an inhibitor of *HES1* repression of *ASCL1* is also highly expressed in early timepoints in *ASCL1*$^{+}$ archetypes in more than 50% of the cells, while *HES1* expression is very low. *HES6* is known to inhibit the repression of *ASCL1* by *HES1*, providing a possible explanation in the early timepoints for in the decrease in *Notch1-3* and *HES1* expression and high ASCL1 expression. Until recently, the molecular mechanisms underlying the distinction between MYC-, MYCL and MYCN- driven subsets of SCLC have remained unexplored. Patel et al. (Patel et al., 2021) showed that *MYC* expression is required to maintain lineage state marker, NEUROD1, in NEUROD1^{+} cells, and *MYC* is incompatible with ASCL1^{+} cells, ultimately leading to trans-differentiation to Neurod1 in SCLC. We see high *MYCL* and *MYCN* expression in early timepoints (Figure 25E, *left*) across SCLC-A/N, -A2 specialists, however, they only make up a very small fraction of cells in these tumors (Figure 25E, *right*).

A very small proportion of cells begin to transition into the SCLC-P/-Y specialist archetype in day 7, and by day 11, we see a large population of cells making up the SCLC-P/-Y archetype (Figure 25C). *JAG2, NOTCH2*, the Notch activating signaling complex (*MAML* and *RBPJ*) and downstream activators *HES1*, and *REST* are

upregulated in day 11, in total making up a little less than 50% of the cells in the SCLC-P/-Y archetype (Figure 25D-F). This suggests *JAG2* may be responsible for activating Notch and signaling in the transition between NE and non-NE states. *SilRT1* is highly expressed in day 11, possibly attributing to the lowered expression of the other Notch receptors. The later timepoints between days 14 and 17 show cells moving towards the SCLC-Y archetype, consistent with the increase in YAP1 expression found in (Ireland et al., 2020). Interestingly, by day 21, cells fall near a new archetype that is not enriched in any of the SCLC signatures, however, are enriched for MYC targets, oxidative phosphorylation, reactive oxygen species (ROS) pathway, and glycolysis (Groves et al., 2021), with further research necessary to characterize this non-NE archetype. However, we do see expression of *JAG2, NOTCH2, RBPJ*, and *REST* in day 21, potentially playing a role in this specialist archetype and correlating with the enrichment of MYC targets (Figure 25D, E). Additionally, these genes are most highly expressed in the generalist population in day 21 (Figure 25G), compared to any other timepoint, suggesting Notch may be an additional distinguisher in this generalist population. It is important to note that the later timepoints are made up of less than 20% of SCLC-Y and SCLC-X specialist cells, and largely composed of generalist cells where Notch signaling is also shown to be expressed. Together, these results show that Notch activation and signaling is differentially expressed across NE and non-NE specialist and generalist archetypes, and inhibitors, *HES6* and *KDM1A* of Notch signaling could potentially be driving the low Notch activation in SCLC-A/-N, -A2 specialists.

Enrichment of Notch ligands and downstream signaling partners in Bulk transcriptomics represent diverse pairing across SCLC archetypes

Given that Notch ligand expression, receptors, and signaling targets and inhibitors are enriched differentially in each archetype, we sought to determine how Notch signaling and pathway expression is regulated within bulk transcriptomics compared to tumors. To explore these relationships between Notch signaling and SCLC subtypes, we analyzed a dataset of bulk RNA-sequencing on 120 human SCLC cell lines from two sources: the CCLE (Barretina et al., 2012), and cBioPortal (Cerami et al., 2012; Gao et al., 2013). This combined dataset contains cell lines with overexpression of each of the four subtypes, ASCL1 (NE), NEUROD1 (NE), POU2F3 (non-NE), and YAP1 (non-NE), sufficiently covering the relevant phenotypic space for SCLC. Interestingly, H82 cells have been shown to express both NE and non-NE markers (Figure 26A), however since they span between SCLC-N and SCLC-Y, they remain unclustered in this analysis. Using AA, we explain the heterogeneity in bulk transcriptomics data between five archetype vertices corresponding to five major SCLC phenotypes (SCLC- A, -A2, -N, -P, and -Y, Figure 26A), and upregulated expression of each across all of the bulk transcriptomics.

Interestingly, we see consistently high expression of DLL1 and JAG2 across majority of SCLC-A, and SCLC-A2 while DLL4 and JAG2, respectively which show lower expression in comparison (Figure 26B). DLL ligands have been shown to be primarily in ASCL1+ cells, however, we see upregulation of DLL1 in the SCLC-P archetype as well, while DLL4 has low to no expression in all non-NE archetypes. The specific role of JAG2 across SCLC subtypes remains unexplored, however we see upregulation of JAG2 across all 5 archetypes, including the H82 unclustered cells, along with high expression of NOTCH2 (Figure 26B). NOTCH1-3 are consistently upregulated in the non-NE

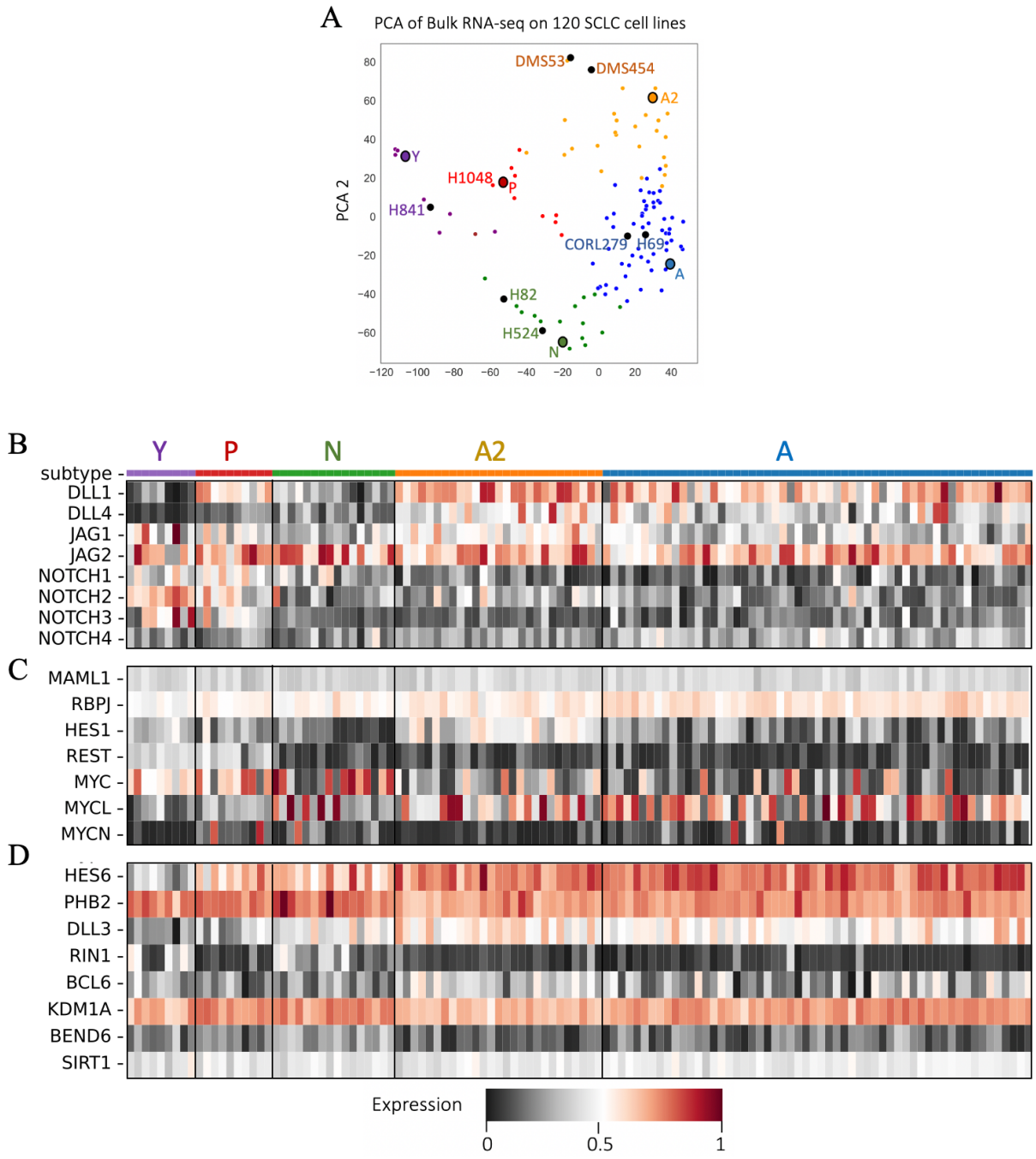

Figure 26: PCA and expression profiles of SCLC subtypes and Notch signaling in bulk transcriptomics data. (A) PCA of bulk RNA-seq on 120 cell lines showing the first two components. Eight cell lines labeled within each archetype were chosen for single cell transcriptomics. Cells are colored according to subtype clustering for ASCL1, NEUROD1, POU2F3, and YAP1. (B) Heat maps of Notch ligands and receptors (C), Notch downstream targets and (D) inhibitors. Subtypes on (B-D) are color coded according to (A).

archetypes, expectedly, however, NOTCH4 is only expressed in the SCLC-A,-A2 archetypes, suggested NOTCH ligands and receptors may be functioning in a context-dependent manner. The activating signaling complex with NOTCH including MAML and RBPJ are upregulated across all archetypes, and RBPJ is most highly expressed in all archetypes except SCLC-Y (Figure 26C). Previous reports have studied SCLC-A2 in the context of NOTCH and HES1 activation, where counterintuitively NOTCH expression is low, however, HES1 expression is high consistent with our findings, however, this mechanism remains unknown. MYC family expression is mixed across each archetype, MYC has highest expression specifically in SCLC-N, -P, and unclustered H82 cells while MYCL is highest in SCLC-A/-A2, and MYCN remains moderately low across all archetypes which suggesting distinct roles within each archetype also reported in previous studies (Figure 26C) (Brägelmann et al., 2017; Patel et al., 2021). When we examine the downstream inhibitors of NOTCH signaling, HES6 and KDM1A (LSD1) are noticeably highly upregulated across all 5 archetypes and H82 cells (Figure 26D). Additionally, DLL3 is moderately to highly expressed across SCLC-A/-A2/N archetypes, consistent with previous studies revealing the regulation of ASCL1 and DLL3 (Figure 26D) (Owen et al., 2019). SIRT1, which negatively regulates NOTCH is moderately expressed consistently across each archetype, along with BCL6 (specifically in SCLC-A/-A2) which could provide rationale for lower expression of NOTCH across these archetypes.

Single cell SCLC transcriptomics reveals Notch signaling is upregulated distinctly in specialist cells

The diversity of SCLC cell line and tumor samples has been characterized by considering bulk RNA-sequencing data, identifying five archetypical gene programs that are enriched at extremes of this phenotypic space. However, bulk RNA-seq and immunohistochemistry

(IHC) analyses confirm some samples are positive for more than one TF, such as tumors that are positive for both ASCL1 and NEUROD1 (Simpson et al., 2020; Zhang et al., 2018). In bulk data, it is unclear if this is due to a mix of discrete NE and non-NE cells, or if intermediate phenotypes exist. These layers of heterogeneity suggest that single-cell data is valuable to fully parse subtype prevalence in SCLC cell lines and tumors. To investigate this heterogeneity within SCLC, we analyzed expression from a panel of 8 cell lines (A: CORL279, H69, A2: DMS454, DMS53, N: H524, H82, P: H1048, Y, H841) selected to maximally span the archetype space (Figure 27A; Materials and Methods, Chapter IV) (Groves et al., 2021). Applying AA to the single cell data using the archetype signatures from the bulk transcriptomics, we found the fall into four archetype vertices (SCLC-A, -A2, -N, -Y), suggesting that SCLC cells also present multi-task optimization within individual cells as well as population (Groves et al., 2021). It is important to note that SCLC-P was not found as an archetype by the cell line expressing POU2F3 (H1048), falling more central in the polytope (Figure 27B), and the proportion of H1048 cells are made up predominately of SCLC-P, along with SCLC-Y and generalist cells. There are a few speculations as to why an SCLC-P archetype was not found outlined in (Groves et al., 2021). For this analysis we will explore Notch signaling within the four identified archetypes and separately for H82, H1048, and CORL279 cells that were not closely classified into the specialist archetypes.

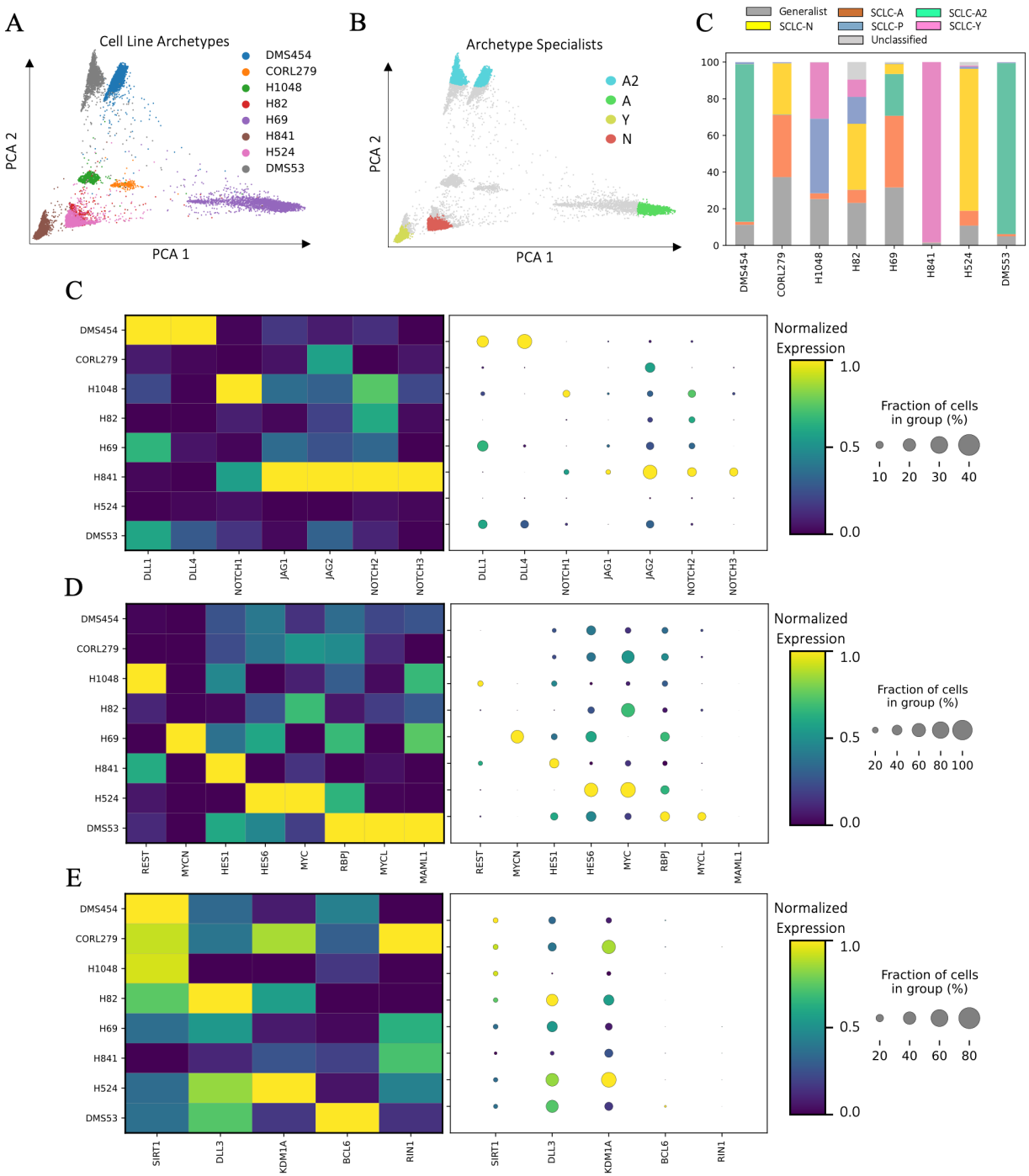

Figure 27: Notch initiation and activation is differentially expressed within single cell transcriptomics. (A) PCA of panel of eight cell lines from single cell transcriptomics. (B) PCA of Archetype specialists and generalists (SCLC-A, -A2, -N, -Y). signature scores for single cells in time course. (C) Stacked bar plots show overall subtype composition change from (*B*). (D-F) Cluster maps of Notch ligands and receptors across time course (D), Notch downstream targets (E), and Notch inhibitors (F).

The single-cell archetype was enriched in one of four SCLC signatures: A, A2, N, or Y (Figure 27B) and occupies a distinct region in archetype space, expected from the bulk transcriptomics (Figure 26A). While each cell line was predominately a single subtype, some included cells that could be classified as generalists, falling between multiple archetypes (Figure 27C). Within one of the two SCLC-A specialists, H69, we see highest expression of MYCN, along with DLL4 and RBPJ, however, the remaining ligands and Notch receptors have very low expression. Additionally, the Notch ligands and receptors in SCLC-A/-N specialist, CORL279 are highly downregulated, JAG2 is the only gene with moderate expression within these cells (Figure 27D), however, we see a large fraction of cells express KDM1A (LSD1), a direct inhibitor of Notch proving a potential rationale for low expression of Notch in these cells (Figure 27F). Interestingly, although DMS454 and DMS53 are both predominately made up of SCLC-A2 specialists (>80%) and previous studies have shown that DLL ligands are upregulated in $ASCL1^{+}$ cells, DLL1 and DLL4 are highly expressed in only one of the SCLC-A2 cell lines, DMS454 (Figure 27C). DLL1 and DLL4 make up a little less than half of the fraction of cells in this cell line and have moderate to low expression in DMS53 cells, suggesting DLL ligand expression may be context-dependent within $ASCL1^{+}$ cells. The remaining Notch ligands JAG1/JAG2 and receptors (NOTCH1-3, NOTCH4 was dropped due to low read counts) make up less than 10% of the cells in both SCLC-A2 specialists, however, downstream targets including RBPJ, HES1, and MYCL are upregulated, while inhibitor, DLL3 is also upregulated, potentially resulting in low NOTCH expression (Figure 27D,E).

H524, an SCLC-N specialist cell line with a small proportion of SCLC-A and generalist cells show no expression of any Notch ligands, receptors, or downstream

targets except for MYC (Figure 27D,E). These specialist cells are also highly expressed in KDM1A (LSD1; Figure 27F), which could be playing a role in the suppression of Notch, reducing the transcription of Notch ligands. Moving towards the non-NE specialists, largely H1048 SCLC-P/-Y specialist with a small proportion of generalist cells, are upregulated in NOTCH1 and NOTCH2, and downstream target REST, however, we see low expression of the remaining Notch ligands, including RBPJ, and MAML, the two genes in the transcriptionally active complex formed with Notch to activate downstream targets (Figure 27D,E). In contrast, H841, SCLC-Y specialists show highly expressed JAG2, NOTCH2, NOTCH3, and HES1, however, the transcriptional activating complex with RBPJ and MAML are not expressed suggesting RBPJ may be acting as a transcriptional repressor (Castel et al., 2013) in the absence of Notch (Figure 27D,E). The unclustered H82 cells from bulk transcriptomics make up a mix of NE and non-NE cells, a large proportion of SCLC-N, -Y, -P, and generalist cells (Figure 26A, 27C). We see low expression across all Notch ligands, receptors, and downstream targets except for upregulation of MYC (Figure 27E) which has been shown to play a role in the NE to non-NE transition (Ireland et al., 2020). We do see highly expressed DLL3 in these cells, although ASCL1 is low, suggesting that DLL3 may also be regulated outside of ASCL1 and a potential rational for low Notch expression (Figure 27F).

A computational model of Notch signaling describes cell-to-cell communication along the path of SCLC subtype transitions

Notch ligands (DLL1 & 4, JAG1 & 2) and receptors (NOTCH1-4) have been extensively studied in the context of cell development and differentiation. The main steps of the Notch signaling cascade are very well conserved across several organisms and include production and targeting of the Notch receptor to the cell membrane, ligand-receptor

binding, conformational rearrangement of the receptor, release of the intracellular domain (NICD) and downstream transcriptional regulation. Here, we propose a detailed, mechanistic model of cell-to-cell communication between NE and non-NE SCLC cells in the context of Notch signaling activation and repression (Table 6, Materials and Methods). The model comprises 16 proteins (ligand/receptor combinatorial binding) interacting via 82 reactions to produce 62 biochemical species, including the ligand/receptor binding, Notch signaling complex activation, transcription of target genes, and transition between an NE and non-NE cell (Figure 28). Below, we describe in detail the steps involved in the ligand/receptor binding and downstream signaling activation, ending with either activation of target genes or inhibitors binding to repress Notch signaling and transition to an NE cell. A model schematic is provided as a visual aid (Figure 28).

Table 6: Summary of key genes involved in Notch signaling

Gene	Role in Notch signaling	References
ASCL1	Transcription factor required for proper development of PNECs and is essential for the survival SCLC with neuroendocrine features.	(Baine et al., 2020; Borromeo et al., 2016a)
BCL6	BCL6 triggers exclusion of the co-activator Mastermind-like 1 (MAML) and recruitment of SIRT1	(Tiberi et al., 2012)
BEND6	BEND6 binds the mammalian CSL protein CBF1 (RBPJ) and antagonizes Notch-dependent target activation, inhibiting of Notch signaling	(Dai et al., 2013)
DLL(1/4)	Ligands are single pass transmembrane receptors and typical Notch activation includes direct cell-cell interaction (trans-activation).	(Mohtashami et al., 2010)
DLL3	Inhibitory Notch ligand that is highly expressed in SCLC. Notch signaling is downregulated during NE tumor growth and is inhibited by DLL3 expression, regulated by ASCL1.	(Furuta et al., 2019; Owen et al., 2019; Xie et al., 2019)
HES1	TF whose expression is initiated by the Notch signaling pathway, a repressor of cell cycle inhibitors.	(Kageyama and Ohtsuka, 1999; T et al., 1999)
HES6	HES6 counteracts HES1 repression of ASCL1 activity, shown to antagonize functionally HES1 and relieve positive bHLH factors like ASCL1 from inhibition by HES1	(Nelson et al., 2009; Somasundaram et al., 2005)
JAG(1/2)	Ligands are single pass transmembrane receptors and typical Notch activation includes direct cell-cell interaction (trans-activation).	(Sasnauskiene et al., 2014; Xiu et al., 2020)
LSD1 (KDM1A)	LSD1 bound to the NOTCH1 locus suppresses NOTCH1 expression and downstream signaling	(Augert et al., 2019)
MAML	Mastermind-like proteins act as critical transcriptional co-activators for Notch signaling with RBPJ	(Liu et al., 2015; Miyamoto and Weinmaster, 2009)
MYC	MYC promotes a neuroendocrine-low phenotype associated with high expression of NEUROD1. MYC and NEUROD1 expression are associated with variant SCLC	(Ireland et al., 2020; Patel et al., 2021)
MYCL	MYCL and ASCL1 as key drivers of tumorigenesis in classic SCLC that are required for tumor growth. ASCL1 proteins were only expressed in MYCN- and MYCL-amplified cells	(Brägelmann et al., 2017; Patel et al., 2021)
MYCN	MYCN overexpression drives SCLC chemoresistance and provide a therapeutic strategy to restore chemosensitivity ASCL1 proteins were only expressed in MYCN- and MYCL-amplified cells	(Brägelmann et al., 2017; Dammert et al., 2019)
NOTCH (1/2/3/4)	The Notch family of type-1 transmembrane receptors consists of four protein paralogs (Notch1–4) in humans and mice.	(Hori et al., 2013; Lim et al., 2017; Meder et al., 2017)
RBPJ	Plays a crucial role in Notch-mediated gene transcription. In the absence of Notch activation, CSL/RBPJ acts as a transcriptional repressor in complex	(Castel et al., 2013; Lake et al., 2014)
REST	Identified as the TF that suppresses the expression of neuronal genes, keeping cells in a non-NE phenotype	(Lim et al., 2017)
RIN1	Identified in a reporter-based cell culture assay to act as a transcriptional repressor complex between RBPJ and SHARP inhibiting Notch signaling	(Hurtado et al., 2019)
SIRT1	SIRT1 associates with NICD and functions as a NICD deacetylase, which opposes the acetylation-induced NICD stabilization	(Xie et al., 2012)

Signaling through the Notch pathway is initiated via juxtracrine signaling with a neighboring cell that expresses one of the four Notch ligands on its surface (DLL1, DLL4, JAG1, JAG2) which can bind to any of the four NOTCH receptors (NOTCH1, NOTCH2, NOTCH3, NOTCH4). A recent review of the biophysics of Notch signaling summarized the binding strengths of Notch ligands to their receptors (Figure 23), and their preferential binding profiles. We include all combinatorial combinations of ligand and receptor binding pairs to encompass all possible avenues for Notch receptors to be activated. Ligand binding promotes two proteolytic cleavage events in the Notch receptor (D'Souza et al., 2008). The first cleavage is catalyzed by ADAM10, and the second is mediated by γ-secretase, resulting in the release of the NECD that gets endocytosed by a neighboring cell, and the NICD which then translocates to the nucleus (Kopan, 2012; Liu et al., 2015). We model these interactions as two species initially bound in complex to form the NOTCH receptors (NOTCH = NECD%NICD) that can then become dissociated to form the NECD and NICD separately, respectively. The NICD then forms an activating transcriptional complex containing RPBJ and MAML, DNA-binding proteins (Lake et al., 2014; Liu et al., 2015). This complex is crucial for any downstream signaling, modeled as three separate species with the requirement that RBPJ binding first, consistent with previous studies reporting that RPBJ is the only nuclear protein known to mediate the bulk of Notch signals (Castel et al., 2013), and helps recruit MAML to the complex. The NICD:RBPJ:MAML transcriptional complex turns on numerous target genes, including REST, MYC family genes, HES family genes, and synthesis of its own ligands and receptors that cycle back to the cleavage processes and cell to cell communication (Brägelmann et al., 2017; Ireland et al., 2020; Kageyama and Ohtsuka, 1999; Lim et al., 2017; T et al., 1999).

Inhibitors of Notch signaling are also included in the model as biologically relevant. These inhibitors include, BCL6, BEND6, DLL3, HES6, LSD1, SIRT1, and RIN1 (diagram simplified for clarity). BCL6 binds to MAML repressing its function (Tiberi et al., 2012), and recruits SIRT1, which negatively regulates the NICD (Xie et al., 2012). BEND6 and RIN1 can also bind to RPBJ and inhibit Notch target activation and signaling, and LSD1 can inhibit the transcription of *Notch* gene stopping the ability for receptor synthesis (Augert et al., 2019). Lastly, DLL3, the only Notch ligand that negatively regulates Notch signaling through *cis*-inhibition, is positively regulated by ASCL1, in turn, repressing non-NE cells towards NE fate (Nandagopal et al., 2019; Owen et al., 2019). We endogenously include expression of ASCL1, YAP1, POU2F3, and NEUROD1 in the model to account for NE and non-NE cell fate decisions. Increased expression of POU2F3 or YAP1 positively regulates Notch signaling and continued cycling through activation and synthesis of the pathway, however, as ASCL1 or NEUROD1 increase in expression, synthesized NOTCH in the nucleus transforms to a “mutated” state, signaling to the neighboring cell to increase transcription of NE markers, including ASCL1 and NEUROD1 to transition from non-NE to NE. Recent studies have reported that increased MYC activation is connected to the NE to non-NE transition along with Notch activation, we include transition back to a non-NE cell with increased NOTCH and MYC expression. This model encompasses all proposed interactions involved in the NE to non-NE transitions in SCLC providing a foundation for exploring mechanistic insights involved in SCLC progression.

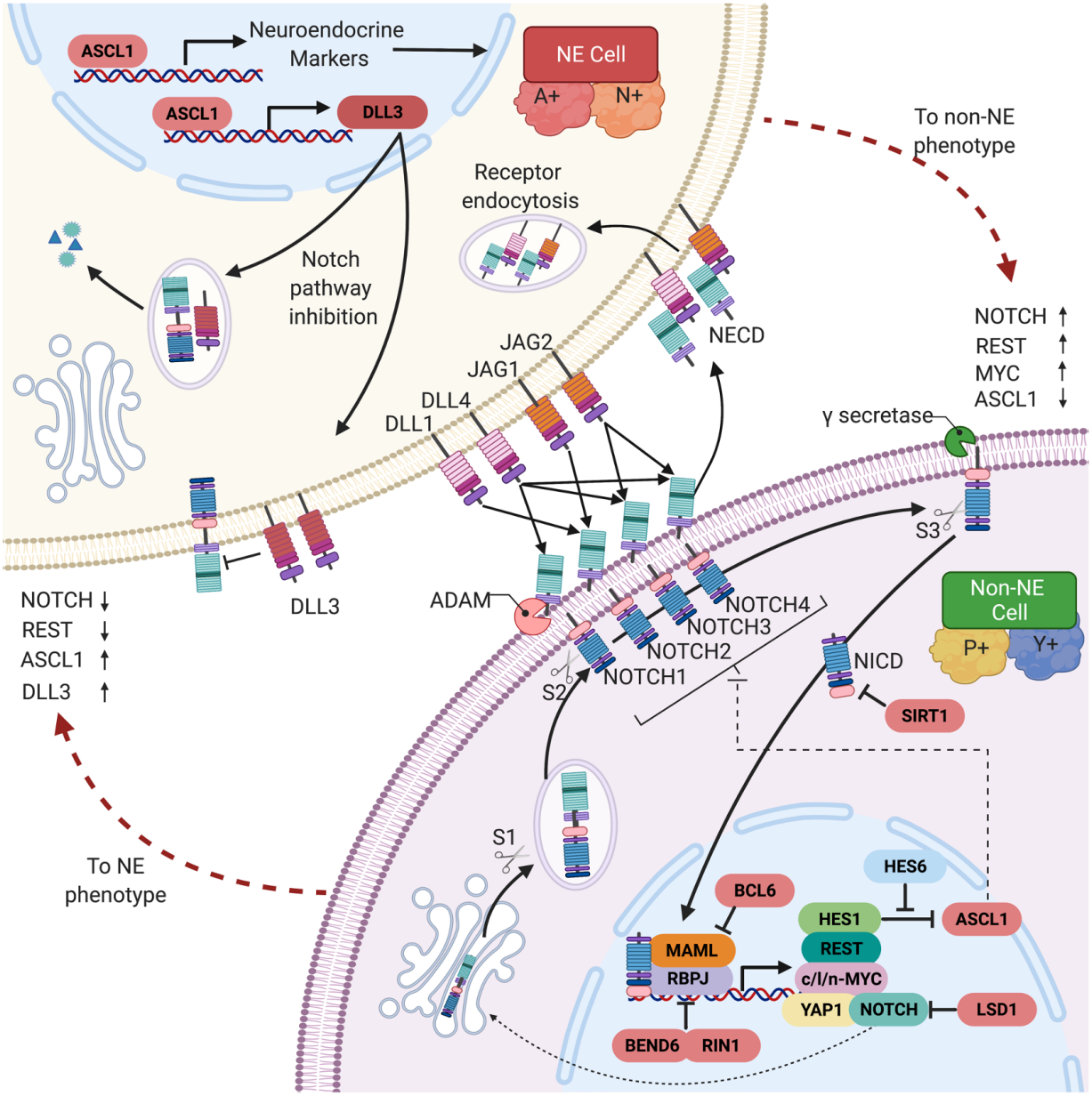

Figure 28: Schematic of the cell-to-cell communication Notch model. The schematic diagram represents non-NE cell communication with NE SCLC cell. Arrows indicate activating interactions, dashed or bar lines represent inhibitory interactions. Non-NE cell regulates positive Notch activation, and increased REST, MYC, and HES1 expression. NE SCLC cell is upregulated in neuroendocrine markers, including ASCL1, NEUROD1, and DLL3. Created with BioRender.com.

DISCUSSION

While SCLC has historically been treated as a single disease, recent studies have converged on the concept that SCLC is composed of at least four molecular subtypes with unique characteristics. Previous bioinformatic approaches classified SCLC into NE and non-NE subtypes (Wooten et al., 2019), suggesting that the subtypes may represent dynamic states of transition. More recently (Groves et al., 2021) we proposed an alternative, continuous view of SCLC heterogeneity based on SCLC archetypes where the transcriptional profile of every single cell can be evaluated based on distance from archetypes and graded as a specialist or generalist (i.e., a cell between archetypes A and Y has a generalist phenotype with a high degree of A and Y characteristics). The goal of this study was to understand dynamics of Notch signaling regulation within these subtypes since Notch activation has been shown to play a role in the NE to non-NE SCLC subtype transition (Ireland et al., 2020; Lim et al., 2017). We found that each of the Notch ligands and receptors have distinct expression profiles across each dataset, differentially expressed from one another and between archetypes supporting the hypothesis that Notch signaling is regulated in a context-dependent manner and that underlying combinatorial complexity between ligand and receptor pairings could contribute to the diversity seen in SCLC.

Together, these results advocate for future studies focused on the complexity that is involved between Notch ligands and receptors, their influence on downstream signaling, and regulation of SCLC. The combination of these global -omics data studies allow us to identify trends across these archetypes, we move towards understanding the biochemical mechanism involved in Notch signaling and SCLC with

our computational model (Figure 28) that incorporates all of the known interactions of Notch signaling (Table 6), and the cell-to-cell communication between neighboring SCLC cells with the goal of identifying distinct pathways of signal transduction that can be mechanistically explained in SCLC progression.

CHAPTER IV

IV. MATERIALS AND METHODS

Necroptosis Methods

Cell culture and reagents

L929 cells (NCTC clone 929, L cell, L-929, derivative of Strain L) were purchased from the American Type Culture Collection (ATCC) and cultured in Dulbecco's Modified Eagle Medium (DMEM; Corning) supplemented with 10% fetal bovine serum (FBS; Omega Scientific), 1% L-Glutamine, and 1% penicillin/streptomycin (Thermo Fisher Scientific) at 5% CO_2 and 37°C. Mouse recombinant TNF was purchased from R&D (Cat# 410-MT-10).

Immunoblotting

L929 cells (2–3 $\times$ 10^6) were grown in 10-cm dishes for 24 h followed by treatment with TNF (0.1, 1, 10, or 100 ng/ml) for 16h. Dead cells were removed by washing with ice cold phosphate-buffered saline (PBS). Remaining adherent cells were lysed using radioimmunoprecipitation assay (RIPA) buffer with 1% Triton X-100, protease, and phosphatase inhibitors. Samples were normalized for total protein concentration (Bradford assay, Bio-Rad), denaturated in 3$\times$ sodium dodecyl sulfate (SDS) sample buffer (5 minutes at 95°C) and subjected to gel electrophoresis (4–15% Criterion™ TGX™ Precast Midi Protein Gel, Bio-Rad) and immunoblotting (polyvinylidene difluoride Transfer Membrane, Thermo Fisher Scientific). Membranes were blocked in 5% bovine serum albumin (BSA)/tris buffered saline with Tween® 20 (TBS-T) and incubated with the following antibodies: pMLKL (1:1000, Abcam, Cat# ab196436), actin (1:3000, Santa Cruz,

Cat# sc-1615), anti-rabbit (1:5000, Santa Cruz, Cat# sc-2004), anti-goat (1:3000, Santa Cruz, Cat# sc-2354). Signal was developed using chemiluminescent substrate (SuperSignal West Pico Plus, Thermo Fisher Scientific) and visualized with ChemiCoc MP imaging system (Bio-Rad).

Determining initial protein concentrations

Expression levels for six proteins (caspase-8, FADD, unmodified MLKL, RIP3, TRADD, and TRAF2) were measured in L929 cells using absolute protein quantitation mass spectrometry. As a negative control, cells were collected in three replicate 6-well plates and cell lysates were gathered, prepped for protein precipitation, pellet, and digestion in the Vanderbilt Mass Spectrometry Research Center (MSRC) Proteomics Core Laboratory. For the other eight proteins in the model, initial concentrations were estimated from measurements reported in the literature and the human protein atlas (Stokes and Lauffenburger, 2022; Uhlén et al., 2005, 2015). Concentrations were converted to units of molecules/cell assuming an L929 cell diameter of 15μm (Milo et al., 2009).

Bayesian parameter calibration

We estimated parameter values using PyDREAM (Shockley et al., 2018), a Python implementation of the DiffeRential Evolution Adaptive Metropolis (DREAM) method (Vrugt and Ter Braak, 2011). We utilized pMLKL Western blot data at the two highest TNF doses (100 and 10 ng/ml) and defined a multi-objective cost function,

$$Cost(\Theta) = \sum_t \sum_d \frac{1}{2\sigma^2(t,d)} [x_m(t,d) - x_e(t,d)]^2 \quad (1)$$

where Q is the parameter set, $x_m(t,d)$ and $x_e(t,d)$ are model-predicted and experimentally measured pMLKL concentrations, respectively, at time t and TNF dose d, and $s(t) = 0.1 \cdot x_e(t,d)$ (following previous studies; Eydgahi et al., 2013; Kochen and Lopez, 2020; Spencer et al., 2009). This function corresponds to the negative log of the likelihood ($-\ln(likelihood(\Theta))$) in the Bayesian framework assuming the measurement errors at time t have a normal distribution. Using the Bayes formula, the value of the log posterior distribution, i.e. the probability of a parameter vector given the experimental data, for a particular parameter vector is defined as

$$-\ln(post(\Theta)) \propto -\ln(likelihood(\Theta)) - \ln(prior(\Theta))$$

where $post(\Theta)$ is the posterior probability of parameter vector Θ, and $prior(\Theta)$ are the prior probabilities assigned to each of the parameters in the parameter vector Θ. PyDREAM samples the posterior distribution and finds probable parameter sets that fit the experimental data within the constraints that the network interactions and the network kinetics imposes. To further constraint the model, we added the requirement that thermodynamic cycles present in the interaction network must obey detailed balance/free energy conservation in the likelihood function. A parameter vector as a set of positive real values, one value representing each reaction rate ("R") defined in the model used to run a simulation. These parameter vectors from PyDREAM represent the differences in the protein-protein binding affinity interactions (association and dissociation rates) within the molecular network. The parameter distributions refer to the frequency of occurrence of different values from the same kinetic parameter.

Parameter sampling was performed using five Monte Carlo chains, each run for 50,000 iterations, the first 25,000 of which were considered burn-in and discarded, resulting in 125,000 parameter sets. Out of these, we extracted an ensemble of 10,628 unique parameter sets. Convergence was achieved for all chains (Figure 9), assessed using the Gelman-Rubin test (Csete and Doyle, 2002; Vrugt, 2016). Starting positions for all PyDREAM chains were determined using particle swarm optimization (Marini and Walczak, 2015 ; PSO): we performed 100 PSO runs, of 500 iterations each, saved the parameter sets from the last iteration of each run, and selected the five with the lowest cost function values (Equation 1). Also, for all parameters, we set prior distributions in PyDREAM to log-normal distributions, $LN\left(\mu = \log_{10}\left(\sum_{i=1}^{5} p_i/5\right), \sigma^2 = 4\right)$, where p_i is the value of the parameter from the *i*-th PSO run. Starting rate constant values for the PSO runs were set to physically plausible values (Aldridge et al., 2006; Lawson et al., 2015): association=10^{-6} min^{-1}, dissociation=10^{-3} min^{-1}, ubiquitination/phosphorylation=1 min^{-1}, and degradation=1 min^{-1} (Table 7). In all cases, simulations were performed by numerical integration of ordinary differential equations (ODEs) using LSODA (Petzold, 1983), as implemented in the Python package SciPy (Virtanen et al., 2020).

Dynamical systems analysis methods

Workflow to obtain a modes of signal execution from fitted parameter network dynamics

Modes of signal execution were identified using PyDyNo, a Python-based software package for dynamical systems analysis of biochemical models with uncertain parameters (Ortega et al., 2021). PyDyNo takes as input a model object as PySB (Lopez et al., 2013b) or SBML (Hucka et al., 2003; Keating et al., 2020) formats, an input file with parameter sets, and a target species (pMLKL, in our case). The algorithm builds a

bipartite graph from the model reaction network. This bipartite graph has a set of nodes that correspond to model species, and another set of nodes that correspond to reactions, and edges only connect species nodes with reaction nodes. This bipartite graph enables the identification of all reactions that produce a specific species. PyDyNo updates the direction of graph edges related to bidirectional reactions to indicate the net flux of the reaction at a specific time point. Hierarchically, the algorithm constructs a dominant pathway starting from the user- defined target species. For the first step, we identify the set of dominant reactions, i.e., those reactions which contribute most to the production of the target species. Dominant reactions are classified based on the instantaneous reaction rates; the conditions determining the dominant reactions are detailed in the following paragraph. We then trace back through the bipartite graph along those dominant reactions to the corresponding reactant species, which are added to the dominant sub-network. For each reactant species that was added to the sub-network we determine their dominant reactions and trace back through the bipartite graph to the next set of reactant species. This procedure is continued for a pre-determined number of iterations defined by the user parameter *depth*. Once the procedure is complete, the result is a species-to-species sub-network representing the dominant pathway over which most of the signal is flowing to produce the target at the current time point. Note that we have defined the dominant sub-networks and their construction based on *production* of the target species. Alternatively, the procedure can be formulated to define the dominant sub-networks and their construction based on the *consumption* of the target species.

ODE simulations are run (Petzold, 1983; Virtanen et al., 2020) for all parameter sets and “digitized” into a sequence of integers, termed a “dynamical signature,” based on “dominant” subnetworks of reactions identified at each time point. Simulating biochemical models with different initial protein levels or kinetic parameters may result in different dynamical signatures. These signatures can be compared to determine their level of discrepancy. We can then group sequences that have similar dominant subnetworks and define these groups of sequences as modes of signal execution. Basically, the algorithm identifies, at every time point, the subnetwork of reactions that contribute most to either the production or consumption (depending on user preference; production, in our case) of the target species and assigns to each identified subnetwork an integer index. Each time point is thus associated with an integer index and the entire simulated time course with a sequence of integers, i.e., the dynamical signature. We refer the reader to the original work (Ortega et al., 2021) for further details on how PyDyNo identifies dominant subnetworks from ODE simulations of biochemical models. We repeated this procedure for all 10,628 unique parameter sets obtained from PyDREAM, with all simulations run at the highest TNF dose (100 ng/ml) for 16h simulated time, in line with experimental data (Fig. 2A). Dynamical signatures were clustered using a spectral clustering method (Von Luxburg, 2007) with the longest common subsequence (Studer and Ritschard, 2016) (LCS) as the distance metric. The optimal number of clusters, i.e., modes of execution, was determined using a silhouette score (Rousseeuw, 1987) for cluster sizes between 2 and 20 (Figure 11). For each mode, a “representative” dynamical signature was defined as the one with the minimal sum of distances to all other signatures(Gabadinho et al., 2011) (i.e., the medoid). Distributions across all mode

combinations were analyzed for significance using the Kolmogorov–Smirnov Test (Table 7).

Sensitivity analyses for initial protein concentrations and rate constants

We used a sensitivity analysis tool (Harris et al., 2017) available in PySB (Lopez et al., 2013) to quantify changes in TTD, defined as the time at which pMLKL reaches a pre-defined threshold (Figure 8D), due to changes in both initial protein concentrations and rate constants. Briefly, the sensitivity analysis tool varies pairs of protein concentrations or rate constants over a range of values relative to a reference set (in this case, [-20%, …, -2%, 0%, 2%, …, 20%]) and calculates the resulting changes in TTD. For each protein or rate constant, a "single-parameter sensitivity multiset" (Harris et al., 2017) is then obtained, which summarizes the range of changes in TTD due to the changes in protein or rate constant values and can be visualized as a boxplot (Figures 15A and 16A). Reference rate constants are those associated with the representative dynamical signatures obtained for each mode from PyDyNo (see previous subsection). For protein concentration sensitivities, reference concentrations are those obtained from mass spectrometry (Figure 8B) and the literature or human protein atlas (Stokes and Lauffenburger, 2022; Uhlén et al., 2005, 2015) (Table 7) and all simulations were performed using the reference rate constant values. Note that we defined a hard threshold of 2,772 pMLKL molecules to define TTD, which is half the amount measured by mass spectrometry (Figure 8B). We chose this, rather than, e.g., the half-maximal amount of pMLKL, to prevent any bias (i.e., changes in the threshold) when varying the initial amount of MLKL. This choice is consistent with experimental evidence that plasma membrane

damage accumulates until a threshold is reached, triggering cell death (Samson et al., 2020).

Results of the sensitivity analyses above, which used reference rate constant values, were then validated by performing, over the full set of rate constant values for each mode, *in silico* KD (70%) and OE (10-fold) experiments for protein concentrations and $\pm$ 10-fold variations for the rate constants (Figures 15B and 16B). This was critical for identifying results that were specific only to the reference parameter set and, hence, could be discounted from our analyses. Statistical significance was determined for each condition's distribution across all modes analyzed using three statistical tests: Kolmogorov–Smirnov Test (2008) for distribution comparison, T-test (Kim, 2015) for mean comparison, and Mood's median test (Virtanen et al., 2020) for median comparison (Tables 7-10).

Table 7: Combinatorial comparisons between modes to determine significance across each rate parameter in the necroptosis model.

	M1, M2	M1, M3	M1, M4	M2, M3	M2, M4	M3, M4
P1	*	*	*	*	*	*
P2	0.001	*	*	*	0.0001	*
P3	0.02	0.01	0.0004	*	0.003	0.001
P4	0.006	*	*	*	*	*
P5	0.03	*	0.001	*	*	*
P6	*	0.186	*	*	0.0003	0.0008
P7	*	0.005	0.01	*	0.07	0.001
P8	0.0002	> 0.05	0.01	*	*	0.82
P9	*	*	*	*	*	*
P10	*	0.005	*	0.0004	*	0.13
P11	*	0.04	*	*	*	*
P12	*	0.0001	*	*	*	*
P13	*	0.025	0.0005	0.0007	*	0.0007
P14	0.13	*	0.002	*	*	*
P15	0.0001	*	*	*	*	*
P16	*	0.0003	*	0.003	*	*
P17	*	*	*	*	*	0.02
P18	*	0.019	*	*	*	*
P19	*	*	*	*	*	*
P20	*	*	*	*	0.024	*
P21	*	0.005	0.04	*	*	0.049
P22	0.07	0.004	> 0.05	*	0.035	0.0002
P23	0.001	*	*	*	*	*
P24	*	0.02	*	*	*	0.0003
P25	*	*	*	0.015	0.001	0.003
P26	*	*	*	*	*	*
P27	*	*	*	0.0018	*	*
P28	*	0.009	*	*	*	*
P29	*	*	0.34	0.017	0.0004	0.001
P30	*	0.0066	0.01	*	*	0.001
P31	*	*	*	*	*	0.001
P32	*	*	*	*	*	*
P33	*	0.01	*	*	*	0.0005
P34	0.012	*	0.01	*	0.04	*
P35	*	*	*	0.001	0.01	0.003
P36	*	0.0001	0.0008	*	*	0.68
P37	0.0002	*	*	*	*	*
P38	*	*	*	*	0.001	> 0.05
P39	*	*	0.005	*	*	*
P40	*	*	*	*	*	> 0.05

Table 8: Statistical tests comparing sensitivity analysis distributions in mode 1.

Initial/Param	KS Test	T-test (mean)	Mood's Median Test	*p<0.05 **p<0.01 ***p<0.001
A20 KD	1.03520e-74	1.5918e-33	2.9380e-12	***
A20 OE	1.8953e-140	2.4207e-19	7.8774e-91	***
cIAP KD	1.8136e-05	0.0008	4.3544e-06	***
cIAP OE	0.1371	0.7373	0.1871	n.s.
CYLD KD	4.1823e-81	4.3665e-12	2.0710e-40	***
CYLD OE	8.9175e-135	3.1246e-116	9.7633e-36	***
P3 decrease	6.3652e-06	0.23163	0.00114	**
P3 increase	3.5829e-65	1.69913e-35	2.6008e-55	***
P10 decrease	3.2075e-12	7.0654e-10	2.4850e-12	***
P10 increase	0.1371	0.4367	0.2205	n.s.
P11 decrease	0.1884	0.5369	0.2296	n.s.
P11 increase	2.69428e-12	2.4622e-09	1.7888e-11	***
P12 decrease	0.0	0.0	0.0	***
P12 increase	0.0	0.0	0.0	***
P13 decrease	1.349e-21	1.7172e-18	4.2564e-18	***
P13 increase	0.00026	0.0629	0.0046	**
P15 decrease	4.953e-135	1.0466e-115	1.8080e-38	***
P15 increase	5.704e-141	3.4649e-22	7.8774e-91	***
P16 decrease	0.9999	0.9135	0.9062	n.s.
P16 increase	0.9293	0.0382	0.6201	n.s.
P17 decrease	9.3784e-142	6.4303e-27	3.3023e-90	***
P17 increase	1.6714e-133	1.3129e-112	2.3516e-35	***
P18 decrease	9.6307e-09	0.0196	2.7160e-08	***
P18 increase	3.1826e-13	0.0382	8.2264e-10	***
P19 decrease	0.2301	0.0866	0.0624	n.s.
P19 increase	0.9999	0.6212	0.7415	n.s.

Table 9: Statistical tests comparing sensitivity analysis distributions in mode 2.

Initial/Param	KS Test	T-test (mean)	Mood's Median Test	*p<0.05 **p<0.01 ***p<0.001
A20 KD	7.4997e-86	2.1061e-12	9.7604e-18	***
A20 OE	1.2302e-126	1.4331e-142	3.3974e-26	***
CYLD KD	1.3967e-77	2.0629e-46	2.6768e-08	***
CYLD OE	7.9421e-151	2.7104e-33	1.9175e-82	***
LUBAC KD	7.6140e-12	6.6652e-09	9.4644e-13	***
LUBAC OE	0.0007	0.0016	0.0394	*
P3 decrease	1.4594e-16	2.4214e-07	2.8901e-09	***
P3 increase	4.3945e-74	5.5113e-71	1.5940e-69	***
P12 decrease	0.0	0.0	0.0	***
P12 increase	0.0	0.0	0.0	***
P13 decrease	6.9340e-22	1.5746e-19	6.9713e-23	***
P13 increase	0.0007	0.0015	0.0394	*
P15 decrease	9.3889e-153	4.2957e-54	1.2566e-81	***
P15 increase	1.2406e-125	3.8085e-140	9.3721e-26	***
P16 decrease	1.9767e-06	0.0119	1.72435e-07	***
P16 increase	1.0745e-08	5.0882e-06	2.9764e-08	***
P17 decrease	1.2302e-126	1.6897e-142	1.2203e-26	***
P17 increase	1.4937e-150	9.8983e-32	4.9150e-82	***
P18 decrease	0.2486	0.0464	0.6491	n.s.
P18 increase	0.2609	0.0031	0.3499	n.s.
P19 decrease	4.1713e-17	1.2320e-08	2.1749e-14	***
P19 increase	1.4708e-20	1.4987e-06	1.4057e-16	***
P20 decrease	0.04718	0.0002	0.0068	**
P20 increase	0.2252	0.0089	0.5655	n.s.

Table 10: Statistical tests comparing sensitivity analysis distributions in mode 3.

Initial/Param	KS Test	T-test (mean)	Mood's Median Test	*p<0.05 **p<0.01 ***p<0.001
C8 KD	0.8683	0.7359	0.3639	n.s.
C8 OE	3.0349e-08	5.2554e-05	4.2363e-09	***
RIP1 KD	0.1340	0.0206	0.1206	n.s.
RIP1 OE	0.0029	2.0104e-05	0.0003	**
TRADD KD	0.0	1.3698e-236	0.0	***
TRADD OE	1.0538e-113	1.2249e-95	6.8001e-77	***
P2 decrease	0.0211	0.1571	0.0084	**
P2 increase	1.6164e-10	8.6257e-09	4.5140e-08	***
P3 decrease	4.3928e-11	0.1162	1.2705e-09	***
P3 increase	6.1210e-93	9.7685e-37	1.8502e-67	***
P4 decrease	3.5056e-215	6.2288e-169	1.3867e-146	***
P4 increase	3.1778e-111	1.8375e-31	9.546e-73	***
P5 decrease	0.0070	0.4334	0.0011	**
P5 increase	0.0014	1.2829e-07	0.0095	**
P6 decrease	0.0026	1.7521e-06	0.0125	*
P6 increase	0.0063	0.2966	0.0008	***
P12 decrease	0.0	0.0	0.0	***
P12 increase	0.0	0.0	0.0	***
P13 decrease	5.0601e-21	1.0476e-11	1.3146e-16	***
P13 increase	7.1901e-05	0.2262	0.0003	***

Table 11: Statistical tests comparing sensitivity analysis distributions in mode 4.

Initial/Param	KS Test	T-test (mean)	Mood's Median Test	*p<0.05 **p<0.01 ***p<0.001
C8 KD	0.7435	0.4863	0.2410	n.s.
C8 OE	1.9702e-06	0.0069	1.3637e-05	***
LUBAC KD	5.1460e-05	0.0718	4.9082e-06	***
LUBAC OE	0.0798	0.5679	0.0477	*
RIP1 KD	0.6514	0.7076	0.1474	n.s.
RIP1 OE	0.2394	0.0778	0.0437	*
TRADD KD	0.0	1.5280e-90	0.0	***
TRADD OE	2.0240e-40	5.0538e-22	1.3349e-27	***
P4 decrease	6.7628e-99	3.4921e-38	2.5383e-72	***
P4 increase	6.4454e-39	0.0005	7.3915e-25	***
P12 decrease	0.0	0.0	0.0	***
P12 increase	0.0	9.8673e-157	0.0	***
P13 decrease	4.7652e-10	0.0143	1.0261e-10	***
P13 increase	0.1364	0.2948	0.0785	n.s.
P14 decrease	1.0	0.5686	0.9707	n.s.
P14 increase	1.0	0.1147	0.8261	n.s.

Data and computer code availability

The data analyzed in these studies were performed using custom Python code, as well as open-source software packages and previously published software. The GitHub repositories used are:

PySB: https://github.com/LoLab-VU/pysb.git

PyDREAM: https://github.com/LoLab-VU/PyDREAM.git

simplePSO: https://github.com/LoLab-VU/simplePSO.git

PyDyNo: https://github.com/LoLab-VU/pydyno.git

NERM repository: https://github.com/LoLab-VU/NERM.git

Notch repository: https://github.com/QuLab-VU/Notch_model_SCLC.git

Archetype Analysis: https://github.com/QuLab-VU/Groves-CellSys2021.git

Common model development for necroptosis and notch signaling

A set of mass action kinetic rules were developed to describe the interactions between proteins and track their concentration changes of various species over time. The necroptosis model is rule-based encoded in PySB, each rule encoding a different set of biochemical reactions in this network. PySB simplifies the error-prone task of enumerating equations describing interactions among multiple proteins into writing a “rule,” the notation which resembles that of biochemical reactions. For example, the rule of the ligand (*L*), binding to its receptor (*R*) is given by

$$Rule('L\_binds\_R', L(r = None) + R(l = None) \mid L(b = 1)\%R(b = 1), k_f, k_r)$$

encoding the reversible binding of this ligand binding to its receptor. $'L\_binds\_R'$ is the name of the rule, $L(r = None)$ is the ligand in the unbound state, $R(l = None)$ is the receptor in the unbound state, | indicates reversible binding, $L(b = 1)\%R(b = 1)$ is the ligand bound to the receptor, and $k_f$and k_r are the forward and reverse kinetic rate constants. The PySB framework automatically generates the Ordinary Differential Equations (ODEs) that define the concentration rate of change of the molecular species using the law of mass action kinetics (Chylek et al., 2014; Lawson et al., 2015; Le Novère and Endler, 2013). This law states that the rate of a chemical reaction is directly proportional to the concentration of reactants. PySB is open source and models are easily shareable, revisable, and extendable (Lopez et al., 2013).

Notch methods: Analyses of publicly available datasets

Bulk RNA-sequencing of human SCLC cell line data

A total of 120 SCLC cell lines were used for analysis of Bulk RNA-sequencing, including, 50 cell lines taken from the cancer cell line encyclopedia (CCLE) (Barretina et al., 2012), and 70 cell lines were taken from cBioPortal deposited by John Minna (Cerami et al., 2012; Gao et al., 2013). Participation in the national cancer institute SCLC consortium provided access to the cBioPortal. The overlap of 29 cell lines between the datasets are denoted with a “c” for CCLE or “m” for Minna to denote the appropriate source. Preprocessing of these datasets was conducted as indicated in (Groves et al., 2021). All genes and cell lines with NAs (missing values) were removed, as well as mitochondrial genes, then filtered and normalized independently and then batch corrected together (Johnson et al., 2007; Leek and Storey, 2007). The four SCLC TF factors that define broad subtypes— ASCL1 (A), NEUROD1 (N), YAP1 (Y), and POU2F3 (P)— were used

to align the two datasets to each other. The resulting batch-corrected dataset contained 120 samples and 15,950 genes.

Single-cell RNA-sequencing of human SCLC cell lines

From the bulk RNA-sequencing data above, eight cell lines were chosen for single-cell RNA-sequencing (Groves et al., 2021). Two cell lines were chosen from each neuroendocrine (NE) subtype: A: H69, CORL279; A2: DMS53, DMS454; N: H82, H524 and one cell line from each non-neuroendocrine (non-NE) subtype: P: H1048; Y: H841. These were chosen to approximate the distributions of subtypes that are seen in the bulk data, largely made up of NE subtypes. The cell lines ranged in their distance from their "assigned" archetype to better understand intermediate samples compared to those closer to their respective archetype. Preprocessing of these datasets was conducted as indicated in (Groves et al., 2021). Filtering was performed using Dropkick (Heiser et al., 2021), removing any cells or genes with low or no reads, then normalized, scaled, and the resulting dataset contained 16,108 cells and 20,446 genes. Spliced and unspliced reads were annotated and RNA expression dynamics of single cells were estimated by *Velocyto* (La Manno et al., 2018). SCLC human cell lines were validated by matching transcript abundance to the bulk RNA-seq data from CCLE. Single-cell RNA-seq counts were analyzed using the Python packages *Scanpy* (Wolf et al., 2018) and *scVelo* (Bergen et al., 2020). *Velocyto* generates loom files that can be used with *Scanpy* and *scVelo* for preprocessing and velocity calculations. *Scanpy* is utilized to read in the loom files as an *AnnData* object (anndata.readthedocs.io).

Preprocessing of mouse tumor (RPM) time-series data

A six point time-course genetically engineered mouse tumor with Hyperactivation of c-Myc ($Rb1^{fl/fl}$;$TP53^{fl/fl}$; Lox-Stop-Lox [LSL]-Myc^{T58A} ;RPM tumors) was preprocessed as indicated in from (Ireland et al., 2020). Filtering using *Scanpy* as indicated above, removed any cells or genes with low or no reads, and non-cancer populations such as immune and stromal cells. This resulted in 15,138 cells with 2,175 of these remaining cells predicted to be doublets. To ensure consistency with the original publication, these these potential doublets were not removed.

CHAPTER V

V. CONCLUSIONS AND FUTURE DIRECTIONS

SUMMARY

Advances in high-throughput technologies that can analyze cellular systems at multiple levels, combined with high-speed computing resources, has facilitated a transition in the research paradigm toward an integrated systems biology approach. However, despite significant progress in the field of systems biology, there is still much to discover in the underlying biochemical complexity of biological systems in the context of cancer and disease with the goal of identifying targets for personalized therapy. The work presented in this dissertation was performed to advance the field's understanding of signaling crosstalk within pathways that are known to regulate cell fate decisions in cancer and diseases, including cell death pathway, necroptosis, and the Notch signaling pathway using systems biology approaches. We present these findings using *Top-down*, and *Bottom-up* approaches in systems biology. These methodologies progress towards the goal of "whole-cell" modeling, which requires in depth understanding of all interconnected pathways from regulating cell survival, inflammation, cell death, proliferation, to learning how to mechanistically control cell fate decisions.

The methods we use throughout this work are detailed in Chapter IV. We discussed the *Bottom-up* model building methodologies, PySB (Lopez et al., 2013), a mathematical framework for building biochemical systems, PyDREAM (Shockley et al., 2018), a framework for model fitting, and PyDyNo (Ortega et al., 2021), a framework for identifying subnetworks of reactions that dominate the production or consumption of target species. Together, these *Bottom-up* approaches allowed us to model the

necroptosis signaling pathway in Chapter II, fit the biochemical model to experimental data, and identify four distinct modes of signal transduction that drive necroptosis execution. We then mapped back the identified modes to characterize cell types within each mode to show that necroptosis is tuned in a context-, species-, and cell type-dependent manner. We also discussed the *Top-down* data-driven approaches, using the publicly available -omics datasets from GEMM tumors (Ireland et al., 2020), bulk transcriptomics (Barretina et al., 2012; Cerami et al., 2012), and single cell transcriptomics in SCLC from our recent work (Groves et al., 2021). Additionally, using these *Top-down* approaches we were able to analyze the role of Notch signaling in SCLC across different biological scales in Chapter III. This included single cell gene expression in SCLC tumors, average gene expression across SCLC cells, and single-cell SCLC gene expression and identified specific Notch ligand and receptor pairings that are context-dependent within SCLC archetypes, and two potential targetable inhibitors of Notch signaling, HES6, and KDM1A (LSD1).

CONCLUSIONS

Necroptosis signaling

Programmed cell death has been studied for decades with a specific focus around apoptosis, however, in the last decade, what was originally thought to be an uncontrolled form of cell death (necrosis), has recently been identified as another form of programmed cell death, necroptosis (Seo et al., 2021; Vanlangenakker et al., 2012). In Chapter III, through an extensive review of the literature derived from decade's worth of experimental studies (Table 1), we built the first detailed biochemical model of TNF-induced necroptosis (Figure 7), fit to experimental data, and obtained 10,628 parameter sets that

all fit our experimental data well (Figure 8). This calibration yielded parameter probability distributions constrained by the experimental data and enabled us to compare the kinetic rate parameters and the inherent uncertainty in their values. These uncertainties are propagated to model predictions, and it is important to understand the mechanisms involved in the generation of different predictions to create testable hypotheses. Taking a dynamical systems analysis approach, we applied the PyDyNo framework to the necroptosis model and found that despite the many parameter sets that fit the experimental data, there are only four modes of signal execution that exist in the model network (Figure 11). Initially, we found varied ranges of variability for pMLKL production which influences TTD that was observed across the four modes (Figure 12), probing our curiosity to determine these underlying drivers. Targeting necroptosis by small molecule targets has emerged as a promising approach for both cancer and inflammatory diseases (Wu et al., 2020). It was of interest to determine if modulating factors existed across all modes of execution and their potential effect on TTD, which could represent novel therapeutic targets. Our model sensitivity analysis (initial conditions and rate parameters) revealed global and mode-specific modulators of necroptosis: Modes 1 and 2 were regulated through interactions involved in RIP1 ubiquitination, and modes 3 and 4 were modulated by factors regulating the balance between complex IIb degradation and necrosome formation (Figures 15 and 16).

When we statistically examined the differences across the four parameter distributions for each mode and each rate parameter, we identified two key parameters, RIP1 deubiquitination by A20 (P19) and CYLD (P20), which were interesting because in each mode, their distributions were in opposite directions (i.e., when P19 ↑, P20 was ↓ in

the same mode) across both parameters. This was intriguing, particularly because both proteins serve as deubiquitinating enzymes in cells, yet experimental studies had controversial results showing CYLD in some cases driving RIP1 deubiquitination and A20 in others. A mechanistic understanding for the experimental results remained an open question, so we encoded these interactions as a competitive binding for RIP1 in complex I to observe if the model would preferentially predict either A20 or CYLD (both with equal likelihood of binding) as drivers. We hypothesized that each mode may represent distinct differences in response to CYLD or A20 depletion, and hence, attain mode specific drivers. We then performed *in silico* KO experiments for CYLD and A20 within each mode (Figure 13B), revealing four distinct roles for CYLD and A20 (Table 4). Mode 1 was driven by A20, while CYLD counterintuitively inhibited TTD, mode 2 resulted in the inverse of mode 1, driven by CYLD, while A20 counterintuitively inhibited TTD, Mode 3 had the ability to be driven by either A20 or CYLD, and mode 4 was driven by CYLD with a dysfunctional role for A20 (i.e., A20KO $\rightarrow$ no change in TTD).

Given that numerous published experimental studies had shown that RIP1 deubiquitination in complex I is driven by A20, CYLD, or both, depending on cell type, we attempted to bring a consensus to the field of necroptosis by examining these studies individually to determine if we could place them in the context of our four modes of execution. For example, Wertz et al. (Wertz et al., 2004) showed that A20 can deubiquitinate RIP1 in human embryonic kidney (HEK) cells and mouse embryonic fibroblasts (MEFs). In contrast, Feoktistova et al. (Feoktistova et al., 2020) reported that deletion of A20 in human T lymphocyte (HTL) cells has no effect on necroptosis sensitivity. Moreover, Moquin et al. (Moquin et al., 2013) reported that RIP1

deubiquitination in MEFs is mediated by CYLD, but proposed it occurs in the necrosome rather than complex I, since knockdown of CYLD had no effect on RIP1 deubiquitination. Vanlangenakker et al. (Vanlangenakker et al., 2011a) showed in mouse fibrosarcoma (MFS) cells that RIP1 can be deubiquitinated by both A20 and CYLD but, while inhibition of CYLD protects cells from necroptosis, inhibiting A20, counterintuitively, increases sensitivity to necroptosis. They also observed no effect on necroptosis after knockdown of TRADD. Hitomi et al. (Hitomi et al., 2008) showed that increased CYLD expression reduces necroptosis in HTL cells. Similarly, Liu et al. (Liu et al., 2014) showed in hippocampal neurons (HCNs) that knockdown of CYLD blocks necroptosis and Wright et al. (Wright et al., 2007) showed that CYLD deubiquitinates RIP1 in human cervical adenocarcinoma (HCAC) cells.

To reconcile these contrasting reports, we associated with each experimental study one or more modes of necroptosis execution identified via our model analysis (Table 5). Specifically, the report by Wertz et al. (Wertz et al., 2004) that A20 deubiquitinates RIP1 in HEK cells and MEFs implies that knocking down A20 would lead to an increase in TTD, i.e., a decrease in sensitivity to necroptosis, which is consistent with mode 1 (Figure 13B). Conversely, the reports by Hitomi et al. (Hitomi et al., 2008), Liu et al. (Liu et al., 2014), and Wright et al. (Wright et al., 2007) all suggest that knocking down CYLD would increase TTD, which could be explained by either modes 2 or 4 (Figure 13B). The report by Vanlangenakker et al. (Vanlangenakker et al., 2011a) also suggests that knocking down CYLD would increase TTD but, importantly, includes additional data that excludes mode 4 as a possibility, i.e., KD of A20, counterintuitively, increases sensitivity to necroptosis and TRADD KD has no effect, which are only consistent with

mode 2 (Figure 13B and Figure 15–*second and bottom rows*). The observation by Feoktistova et al. (Feoktistova et al., 2020) that deletion of A20 has no effect on necroptosis sensitivity in HCAC cells is intriguing because it is consistent with both modes 3 and 4 (Figure 13B) and they used the same cell line (HeLa) as Wright et al. (Wright et al., 2007), who's observations are consistent with modes 2 and 4 (as mentioned above). This could indicate that HCAC cells (or HeLa cells, specifically) operate via mode 4, since both studies are consistent with this mode, or that the cells in these experiments are operating via different modes of necroptosis execution due to differences in context, i.e., genetic or epigenetic variations between samples or differences in experimental conditions between laboratories. Finally, the report by Moquin et al. (Moquin et al., 2013) is particularly interesting because their observation that CYLD binds to complex I but RIP1 ubiquitination is not affected in CYLD-deficient MEFs led them to conclude that RIP1 ubiquitination is regulated by CYLD in the necrosome, rather than complex I. However, our analysis shows these observations are consistent with mode 4, in which TTD increases for CYLD KO (Figure 13B) but there is no effect on TTD for CYLD KD < 90% (Figure 15B–*bottom row* and Figure 18B). Thus, the results of our *in silico* analyses, based on different parameterizations of a consensus model of necroptosis, explain a variety of incommensurate and counterintuitive experimental observations in the literature and provide an alternate explanation for a result that is seemingly inconsistent with prior studies.

Notch signaling in SCLC

The Notch signaling pathway is known to mediate cell fate decisions (Hori et al., 2013), and has been shown to be both tumor suppressive or oncogenic depending on the context

(Aster et al., 2017; Galluzzo and Bocchetta, 2014). In SCLC, loss-of-function *NOTCH* mutations and inhibitory effects of ectopic Notch activation indicate that Notch signaling is tumor suppressive (George et al., 2015; Koch and Radtke, 2007). In Chapter III, we take a *Top-down* approach to globally analyze three -omics datasets including a MYC-driven ($p53^{fl/fl}$;$Rb^{fl/fl}$; Lox-Stop-Lox [LSL]-Myc^{T58A}, RPM) mouse model of SCLC (Ireland et al., 2020), bulk transcriptomics from 120 SCLC cell lines (Barretina et al., 2012; Cerami et al., 2012), and single-cell transcriptomics from our current work (Groves et al., 2021).

We find within the RPM tumors in SCLC-A/-A2 specialists, we observed elevated expression of the four Notch ligands, *DLL1* (day 4), *DLL4* (day 7), *JAG1* (day 7), *JAG2* (day4) along with moderate expression of *NOTCH1-3* (days 4 & 7), suggesting that Notch is active within *ASCL1*$^{+}$ cells, however, due to the elevated expression of three of the Notch inhibitors, *DLL3*, *HES6* (both indirect Notch inhibitors), and *KDM1A* (*LSD1*), *NOTCH1-3* expression is reduced, while *NOTCH2* shows very low expression. KDM1A was recently identified (Augert et al., 2019) as a direct NOTCH1 inhibitor, and inhibiting KDM1A rescued NOTCH1 mRNA and NOTCH1 protein. This study did not examine the effect of KDM1A on the other Notch receptors, however, we hypothesize that Notch reduction in *ASCL1*+ cells could be rescued with the addition of the small molecule inhibitor of KDM1A they discovered providing another avenue for targeting NE cells in SCLC. As cells transitioned between SCLC-A/-A2/N specialists (NE), and SCLC-P/-Y specialists (non-NE) we saw decreased expression of Notch ligands and *NOTCH1-3* receptors, moderate expression of *JAG2*, and increased expression of *NOTCH2*, *RBPJ*, *HES1*, *REST*, *KDM1A*, and *SIRT1,* previously shown to directly inhibit the NICD (Xie et al., 2012), providing a potential explanation for the decreased expression of the other

Notch receptors. A possible mechanism for the role of NOTCH in conjunction with MYC driving NE cells to non-NE states, is a direct connection between *JAG2* binding to *NOTCH2* effectively activating its downstream targets, even in the presence of *KDM1A*. *SIRT1* and *KDM1A* and the Notch pathway make up about 50% of these cells, motivating the possibility that they may not be functioning within the same cells but combined account for all the cells. Most interestingly, in the later timepoints, SCLC-Y/-X specialist and generalist cells between days 14-21 are upregulated again in *NOTCH2*, *RBPJ*, *HES1*, and *REST,* however ligand expression is reducing potentiating the idea from (Ireland et al., 2020) that MYC and NOTCH cooperate with one another to drive SCLC progression in when ligand expression is reduced. An interesting note, in day 21 generalist cells (Figure 25B), we saw most highly expressed *JAG2*, *NOTCH2*, and *REST* genes (Figure 25G), where these cells were not enriched for archetype markers. This could be due to AA fitting or that these genes in particular are working together with MYC to progress SCLC outside of the identified archetypes.

Examining the SCLC-A/-A2 archetypes in the bulk transcriptomics (Figure 26), consistent with the RPM tumors we observed upregulation of the four Notch ligands, with the addition of DLL1 in SCLC-P, and steady JAG2 expression across all cells including unclustered H82 cells (Figure 26B). However, we see decreased NOTCH expression in SCLC-A/-A2, contrast to RPM early timepoints, with only upregulated NOTCH4 expression in ASCL1^{+} cells (Figure 26B). RBPJ MYC, MYCL were also upregulated in SCLC-A/-A2, which could suggest that the Notch ligands could be interacting specifically with NOTCH4 in these cells, effectively activating downstream targets. We also see upregulated expression of HES6 (except SCLC-Y), and KDM1A across all archetypes

(Figure 26D), further confirming their importance in regulating Notch activity in SCLC. Hyperactivation of MYC in the RPM tumors was proposed to cooperate with NOTCH to progress SCLC from NE to non-NE fates, however in the bulk transcriptomics MYC and Notch do not appear to be correlated, except for expression of NOTCH4. Within the SCLC-A2 archetype, as previously noted, HES1 expression is upregulated while Notch expression is downregulated (Wooten et al., 2019), however, we see upregulation of MAML and RBPJ, which is known to form a transcriptional activation complex with Notch to activate downstream target genes. MAML and RBPJ may be endogenously expressed in these cells while Notch expression is being inhibited by the upregulated expression of KDM1Aor SIRT1 (Figure 26D). H82 cells have been reported to express SCLC-N and SCLC-Y markers, existing between subtypes, and here we see that JAG2, NOTCH2, MYC, HES6, and KDM1A are the only highly expressed genes in these cells surrounding Notch signaling (Figure 26B-D). Additionally, MAML, RBPJ, REST, MYCL, DLL3, and SIRT1 are moderately expressed in these cells (Figure 26C,D). A potential mechanism underlying these expression profiles is that Jag2 and Notch2 are highly regulated together, potentially in conjunction with MYC or MYCL to form a complex with MAML, and RBPJ which results in activation of REST, while HES6 inhibits HES1 expression, and SIRT1 and KDM1A are specific targets of NOTCH1,3,4 and not NOTCH2.

As we moved towards single cell transcriptomic analysis (Figure 27A), AA identified four archetypes representative of SCLC-A, -A2, -N, and -Y (Figure 27B,C), however an SCLC-P archetype was not identified (Groves et al., 2021). DMS454 and DMS53 are classified as SCLC-A2 specialists, however their expression profiles regarding Notch signaling differed distinctly. DMS454 cells showed high expression of

DLL1 and DLL4, with low expression of NOTCH, while DSM53 cells had moderate to low expression of DLL1 and DLL4 in comparison. SIRT1 may be regulating the expression of NOTCH in DMS454 cells, however in DMS53 cells, increased DLL3 expression expectedly represses Notch signaling, yet we see increased expression of RBPJ, in the absence of Notch. The bulk transcriptomics also showed upregulated expression of RBPJ and MYCL together (Figure 27E), suggesting their expression may be correlated together, requiring further analysis to confirm this result. Notch expression was most upregulated in SCLC-Y, H841 specialist cells, with increased expression of HES1, however, decreased expression of Notch ligands, RBPJ, and MAML (Figure 27E). Consistently across each dataset we find a division between Notch receptor expression and previously reported regulation of Notch with RBPJ and MAML to form the active transcriptional complex (Castel et al., 2013; Miyamoto and Weinmaster, 2009). In the other non-NE cell line, H1048, SCLC-P specialist, we saw decreased expression of Notch ligands, except for moderate expression of JAG2, however increased expression of NOTCH1,2, and REST (Figure 27D,E). JAG2 may have an unexplored binding affinity for NOTCH1 or NOTCH2 in SCLC that can regulate Notch activation and downstream REST expression. H524 cells, SCLC-N specialists have overall decreased Notch ligand and receptor expression, MYC is the only gene highly expressed, consistent with previous studies reporting MYC upregulation in NEUROD1+ cells (Borromeo et al., 2016b; Patel et al., 2021). Together, our global analyses provide rationale, explanation, and hypotheses for the differentially expressed Notch ligands and receptors across SCLC, supporting our hypothesis that the combinatorial complexity between the ligand/receptor pairings play a significant role in SCLC progression.

FUTURE DIRECTIONS

In the remainder of this chapter, I will discuss future studies that can address questions developed from our findings. Several important topics remain in necroptosis, (i) Mechanistic regulation of necroptosis triggered by different stimuli, (ii) Small molecule targets for cancer treatment, (iii) Crosstalk with other cell death pathways, and (iv) MLKL permeabilization of the plasma membrane after phosphorylation not yet analyzed in our model. In Notch signaling and SCLC, (i) Tracking transition paths between tumors and cell lines, (ii) Mechanistic understanding of ligand/receptor combinatorial complexity, (iii) Small molecule targets for Notch signaling, and (iv) Crosstalk with other cell developmental pathways.

Future directions for necroptosis

Our biochemical necroptosis model was able to explain numerous contrasting and counterintuitive experimental results seen in different cell types, providing the first detailed systems understanding of necroptosis. Much work remains to determine the mechanisms of necroptosis crosstalk with other pathways, stimuli, MLKL permeabilization, which are all connected to identifying potential targets in necroptosis for cancer and disease. We have identified various avenues for model extension to incorporate other interactions known to be involved in necroptosis that we had simplified for the purpose of this study. For example, the model can be expanded to include additional proteins and necroptosis-associated receptors (Zhou and Yuan, 2014b) (e.g., TNFR2, CD95, Toll-like receptors) and ligands (Füllsack et al., 2019; Kearney et al., 2015; Strasser et al., 2009) (e.g., LPS, FasL, TRAIL), which directly target complex II and necrosome formation in contrast to the

initial formation of complex I. In our current model, we also simplified the interactions of cIAP, LUBAC, and RIP1 ubiquitination involved in complex I. It would be interesting to include both forms of cIAP (McComb et al., 2012) (i.e., cIAP1 and cIAP2), assembly of the LUBAC trimer complex (Haas et al., 2009), and different RIP1 ubiquitin chains (Samson et al., 2021) (i.e., M1, K48, K63). Within downstream formation of complex II, including additional biochemical events involved in the activation of C8 (Donepudi et al., 2003) (e.g., binding of pro-C8 to FADD, followed by oligomerization and cleavage), will be very interesting as the current model has simplified the cleavage and activation steps involving C8 and FLIP.

Along the RIP1-RIP3-MLKL axis we discussed, a more prominent area of study has focused on controlling the formation of the necrosome and MLKL permeabilization at the plasma membrane. The necrosome is controlled at the posttranslational level by phosphorylation and ubiquitination (Liu et al., 2016). Multiple studies show that during TNF-induced necroptosis, RIPK1, RIPK3, and MLKL relocate from the cytosol into discrete perinuclear clusters that are presumably necrosomes (Samson et al., 2021; Wang et al., 2014). In order to test in silico how small molecules impact necroptosis (Bolik et al., 2021; Chen et al., 2019) (e.g., ADAM17, CHIP, TAK1, necrostatins), detailing these interactions is very valuable. The model can also be extended to include downstream events involved in MLKL-mediated permeabilization of the plasma membrane (Samson et al., 2020; Wang et al., 2014) (e.g., Golgi-, microtubule-, and actin-dependent mechanisms), and most importantly, crosstalk with pro-survival (Vanden Berghe et al., 2015; Metzig et al., 2020) (e.g., NF-κB) and other programmed cell death (L. et al., 2012)

(e.g., apoptosis) pathways, and connections to the immune system (Gong et al., 2019) (e.g., antigen-induced proliferation of T cells).

Lastly, out of the four identified modes using the dynamical systems analysis framework, we were speculative as to why there was not an identified mode that was driven solely by A20 with no effect from CYLD. We identified two modes that are driven by A20 or CYLD, while their counterparts serve inhibitory roles, one mode that is driven by either enzyme, or the fourth mode that driven solely by CYLD, with a dysfunctional role for A20. This mode was most intriguing because we found there was a CYLD threshold, requiring more than 85% depletion of CYLD to influence TTD, while knocking out A20 had no effect on TTD. We hypothesized that the potential fifth mode that was not identified did not make up enough of the rate parameters to cluster into its own mode and that it may have been divided across the other modes. It would be interesting to repeat the model calibration with more iterations to see if we obtain the same number of modes.

Future directions for Notch in SCLC

As clinical trials begin to assess biomarkers of SCLC subtypes and potentially enroll patients based on these subtypes (Brcic et al., 2019; Gay et al., 2021; Morgensztern et al., 2019; Schwendenwein et al., 2021), it is critical to evaluate this phenotypic heterogeneity and understand in the context of tumor evolution to other subtypes. DLL3 is a pharmacological inhibitor that has been identified to increase Notch activation and progress SCLC towards non-NE phenotypes (Huang et al., 2019; Owen et al., 2019). DLL3 is also the only Notch ligand that exists to function as a *cis*-interaction inside cells, that is regulated by NE marker ASCL1 to inhibit Notch receptor activation. In addition to DLL3, our analysis showed and suggests that KDM1A (LSD1) inhibits NOTCH through

direct binding and a recent inhibitor was shown to repress this inhibitory function by LSD1 of NOTCH and rescue NOTCH activation (Augert et al., 2019). Along with DLL3 and KDM1A, HES6 was upregulated across each archetype, motivating the importance of future studies to identify potential HES6 inhibitors with the hope of decreasing ASCL1 expression and increased HES1 and Notch pathway activation to move SCLC cells towards non-NE fates.

To determine the transition paths of cells that have upregulated expression of these three inhibitors in SCLC progression, it would be interesting to apply *CellRank*, a recently developed approach to analyze gene expression (RNA) velocity. This framework will allow us to track whether a cell has progressed along multiple archetype "lineages." Within the RPM tumors, we can then approximate which cells transitioned from early timepoints in tumors to non-NE archetypes by day 21. *CellRank* can incorporate velocity information to fit to each timepoint and measure temporal dynamics and infer directionality and magnitude of gene expression change for future timepoints. It is interesting to note that each of these scales within SCLC biology that we examined still lack the proper temporal resolution to accurately track gene expression trends, and more importantly, the translation to proteins. Since transcription of genes occurs on the order of 10 minutes/gene (Shamir et al., 2016), and protein translation occurs on the order of 1 minute/protein (Shamir et al., 2016), it is highly likely that the timescale resolution over days is not accounting for a lot of useful information. Additionally, the absence of time within the bulk and single cell transcriptomics is crucial to truly determine the role that Notch plays in SCLC. Experimental time-course transcriptomic and proteomic studies will be indispensable to accurately track the progression of this lethal disease. In our most

recent efforts and ongoing analyses, moving forward with our mechanistic model we have developed to further study Notch signaling and SCLC progression, we are focused on including timescales to encompass transcription of genes and translation of those genes to proteins. This will provide us with the necessary information to determine how Notch ligand and receptor pairings as well as downstream activating and inhibitory events are contributing to the NE to non-NE cell fate decision.

CONCLUDING REMARKS

In conclusion, the research presented herein has provided new insights to understanding some of the many facets that contribute to cell fate decisions, specifically focused on elucidating mechanisms involved in necroptosis, and how notch signaling is involved in SCLC. Our work demonstrates that necroptosis is tuned in a cell type-, species-, and context-dependent manner driven by four distinct modes of execution. Additionally, we observe that the combinatorial complexity involved in the Notch ligand and receptor pairing has the potential to drive and determine NE to non-NE cell fates in SCLC. Taken together, these two pathways are fundamental to understanding a wide range of biological processes. Continued study of each of these signaling pathways may reveal distinct and novel ways to target cell or tumor death and manipulate a cells decision to commit to a given fate.

REFERENCES

Albeck, J.G., Burke, J.M., Spencer, S.L., Lauffenburger, D.A., and Sorger, P.K. (2008). Modeling a Snap-Action, Variable-Delay Switch Controlling Extrinsic Cell Death. PLOS Biol *6*, e299.

Aldridge, B.B., Burke, J.M., Lauffenburger, D.A., and Sorger, P.K. (2006). Physicochemical modelling of cell signalling pathways.

Aldridge, B.B., Saez-Rodriguez, J., Muhlich, J.L., Sorger, P.K., and Lauffenburger, D.A. (2009). Fuzzy Logic Analysis of Kinase Pathway Crosstalk in TNF/EGF/Insulin-Induced Signaling. PLOS Comput. Biol. *5*, e1000340.

Allen, F., and Maillard, I. (2021). Therapeutic Targeting of Notch Signaling: From Cancer to Inflammatory Disorders. Front. Cell Dev. Biol. *9*, 1262.

Alyass, A., Turcotte, M., and Meyre, D. (2015). From big data analysis to personalized medicine for all: Challenges and opportunities. BMC Med. Genomics *8*, 1–12.

Andrawes, M.B., Xu, X., Liu, H., Ficarro, S.B., Marto, J.A., Aster, J.C., and Blacklow, S.C. (2013). Intrinsic selectivity of Notch 1 for Delta-like 4 over Delta-like 1. J. Biol. Chem. *288*, 25477–25489.

Van Antwerp, D.J., Martin, S.J., Kafri, T., Green, D.R., and Verma, I.M. (1996). Suppression of TNF-α-induced apoptosis by NF-κB. Science (80-.). *274*, 787–789.

Ashyraliyev, M., Fomekong-Nanfack, Y., Kaandorp, J.A., and Blom, J.G. (2009). Systems biology: parameter estimation for biochemical models. FEBS J. *276*, 886–902.

Aster, J.C., Pear, W.S., and Blacklow, S.C. (2017). The Varied Roles of Notch in Cancer. Annu. Rev. Pathol. Mech. Dis. *12*, 245–275.

Augert, A., Eastwood, E., Ibrahim, A.H., Wu, N., Grunblatt, E., Basom, R., Liggitt, D., Eaton, K.D., Martins, R., Poirier, J.T., et al. (2019). Targeting NOTCH activation in small cell lung cancer through LSD1 inhibition. Sci. Signal. *12*.

Ayaz, F., and Osborne, B.A. (2014). Non-canonical Notch signaling in cancer and immunity. Front. Oncol. *4*.

Baine, M.K., Hsieh, M.S., Lai, W.V., Egger, J. V., Jungbluth, A.A., Daneshbod, Y., Beras, A., Spencer, R., Lopardo, J., Bodd, F., et al. (2020). SCLC Subtypes Defined by ASCL1, NEUROD1, POU2F3, and YAP1: A Comprehensive Immunohistochemical and Histopathologic Characterization. J. Thorac. Oncol. *15*, 1823–1835.

Barretina, J., Caponigro, G., Stransky, N., Venkatesan, K., Margolin, A.A., Kim, S., Wilson, C.J., Lehár, J., Kryukov, G. V., Sonkin, D., et al. (2012). The Cancer Cell Line Encyclopedia enables predictive modelling of anticancer drug sensitivity. Nat. 2012 4837391 *483*, 603–607.

Basak, S., and Hoffmann, A. (2008). Crosstalk via the NF-κB signaling system. Cytokine Growth Factor Rev. *19*, 187–197.

Belizário, J., Vieira-Cordeiro, L., and Enns, S. (2015). Necroptotic cell death signaling and execution pathway: Lessons from knockout mice. Mediators Inflamm. *2015*.

Bergen, V., Lange, M., Peidli, S., Wolf, F.A., and Theis, F.J. (2020). Generalizing RNA velocity to transient cell states through dynamical modeling. Nat. Biotechnol. 2020 3812 *38*, 1408–1414.

Vanden Berghe, T., Kaiser, W.J., Bertrand, M.J.M., and Vandenabeele, P. (2015). Molecular crosstalk between apoptosis, necroptosis, and survival signaling. Mol. Cell. Oncol. *2*.

Bolik, J., Krause, F., Stevanovic, M., Gandraß, M., Thomsen, I., Schacht, S.S., Rieser, E., Müller, M., Schumacher, N., Fritsch, J., et al. (2021). Inhibition of ADAM17 impairs endothelial cell necroptosis and blocks metastasis. J. Exp. Med. *219*, 219.

Borromeo, M.D., Savage, T.K., Kollipara, R.K., He, M., Augustyn, A., Osborne, J.K., Girard, L., Minna, J.D., Gazdar, A.F., Cobb, M.H., et al. (2016a). ASCL1 and NEUROD1 Reveal Heterogeneity in Pulmonary Neuroendocrine Tumors and Regulate Distinct Genetic Programs. Cell Rep. *16*, 1259–1272.

Borromeo, M.D., Savage, T.K., Kollipara, R.K., He, M., Augustyn, A., Osborne, J.K., Girard, L., Minna, J.D., Gazdar, A.F., Cobb, M.H., et al. (2016b). ASCL1 and NEUROD1 Reveal Heterogeneity in Pulmonary Neuroendocrine Tumors and Regulate Distinct Genetic Programs. Cell Rep. *16*, 1259–1272.

Brägelmann, J., Böhm, S., Guthrie, M.R., Mollaoglu, G., Oliver, T.G., and Sos, M.L. (2017). Family matters: How MYC family oncogenes impact small cell lung cancer. Cell Cycle *16*, 1489.

Brcic, L., Kuchler, C., Eidenhammer, S., Pabst, D., Quehenberger, F., Gazdar, A.F., and

Popper, H. (2019). Comparison of four DLL3 antibodies performance in high grade neuroendocrine lung tumor samples and cell cultures. Diagn. Pathol. *14*.

Bruggeman, F.J., and Westerhoff, H. V. (2007). The nature of systems biology. Trends Microbiol. *15*, 45–50.

Carney, D.N., Gazdar, A.F., Bepler, G., Guccion, J.G., Marangos, P.J., Moody, T.W., Zweig, M.H., and Minna, J.D. (1985). Establishment and Identification of Small Cell Lung Cancer Cell Lines Having Classic and Variant Features. Cancer Res. *45*.

Carrera, J., and Covert, M.W. (2015). Special Issue: Quantitative Cell Biology Forum Why Build Whole-Cell Models?

Carswell, E.A., Old, L.J., Kassel, R.L., Green, S., Fiore, N., and Williamson, B. (1975). An endotoxin-induced serum factor that causes necrosis of tumors. Proc. Natl. Acad. Sci. U. S. A. *72*, 3666–3670.

Castel, D., Mourikis, P., Bartels, S.J.J., Brinkman, A.B., Tajbakhsh, S., and Stunnenberg, H.G. (2013). Dynamic binding of RBPJ is determined by Notch signaling status. Genes Dev. *27*, 1059–1071.

Cerami, E., Gao, J., Dogrusoz, U., Gross, B.E., Sumer, S.O., Aksoy, B.A., Jacobsen, A., Byrne, C.J., Heuer, M.L., Larsson, E., et al. (2012). The cBio Cancer Genomics Portal: An Open Platform for Exploring Multidimensional Cancer Genomics Data. Cancer Discov. *2*, 401–404.

Chapman, G., Sparrow, D.B., Kremmer, E., and Dunwoodie, S.L. (2011). Notch inhibition by the ligand DELTA-LIKE 3 defines the mechanism of abnormal vertebral segmentation in spondylocostal dysostosis. Hum. Mol. Genet. *20*, 905–916.

Chen, R., and Snyder, M. (2012). Systems Biology: Personalized Medicine for the Future? Curr. Opin. Pharmacol. *12*, 623.

Chen, J., Kos, R., Garssen, J., and Redegeld, F. (2019). Molecular Insights into the Mechanism of Necroptosis: The Necrosome As a Potential Therapeutic Target.

Chen, W.W., Niepel, M., and Sorger, P.K. (2010). Classic and contemporary approaches to modeling biochemical reactions. Genes Dev. *24*, 1861–1875.

Cho, Y.S. (2018). The role of necroptosis in the treatment of diseases. BMB Rep. *51*, 219–224.

Cho, Y.S., Challa, S., Moquin, D., Genga, R., Ray, T.D., Guildford, M., and Chan, F.K.-M.M. (2009). Phosphorylation-Driven Assembly of the RIP1-RIP3 Complex Regulates Programmed Necrosis and Virus-Induced Inflammation. Cell *137*, 1112–1123.

Choi, M.E., Price, D.R., Ryter, S.W., and Choi, A.M.K. (2019). Necroptosis: A crucial pathogenic mediator of human disease. JCI Insight *4*.

Chylek, L.A., Harris, L.A., Tung, C.-S., Faeder, J.R., Lopez, C.F., and Hlavacek, W.S. (2014). Rule-based modeling: a computational approach for studying biomolecular site dynamics in cell signaling systems. Wiley Interdiscip. Rev. Syst. Biol. Med. *6*, 13–36.

Claxton, S., and Fruttiger, M. (2004). Periodic Delta-like 4 expression in developing retinal arteries. Gene Expr. Patterns *5*, 123–127.

Cook, D.P., and Wrana, J.L. (2022). A specialist-generalist framework for epithelial-mesenchymal plasticity in cancer. Trends in Cancer.

Crabtree, J.S., Singleton, C.S., and Miele, L. (2016). Notch signaling in neuroendocrine tumors. Front. Oncol. *6*, 94.

Csete, M.E., and Doyle, J.C. (2002). Reverse engineering of biological complexity. Science (80-.). *295*, 1664–1669.

D'Souza, B., Miyamoto, A., and Weinmaster, G. (2008). The many facets of Notch ligands. Oncogene *27*, 5148.

Dai, Q., Andreu-Agullo, C., Insolera, R., Wong, L.C., Shi, S.H., and Lai, E.C. (2013). BEND6 is a nuclear antagonist of Notch signaling during selfrenewal of neural stem cells. Dev. *140*, 1892–1902.

Dallas, M.H., Varnum-Finney, B., Delaney, C., Kato, K., and Bernstein, I.D. (2005). Density of the Notch ligand Delta1 determines generation of B and T cell precursors from hematopoietic stem cells. J. Exp. Med. *201*, 1361–1366.

Dammert, M.A., Brägelmann, J., Olsen, R.R., Böhm, S., Monhasery, N., Whitney, C.P., Chalishazar, M.D., Tumbrink, H.L., Guthrie, M.R., Klein, S., et al. (2019). MYC paralog-dependent apoptotic priming orchestrates a spectrum of vulnerabilities in small cell lung cancer. Nat. Commun. 2019 101 *10*, 1–11.

Declercq, W., Vanden Berghe, T., and Vandenabeele, P. (2009). RIP Kinases at the Crossroads of Cell Death and Survival. Cell *138*, 229–232.

Degterev, A., Huang, Z., Boyce, M., Li, Y., Jagtap, P., Mizushima, N., Cuny, G.D., Mitchison, T.J., Moskowitz, M.A., and Yuan, J. (2005). Chemical inhibitor of nonapoptotic cell death with therapeutic potential for ischemic brain injury. Nat. Chem. Biol. *1*, 112–119.

Delaney, G., Jacob, S., Featherstone, C., and Barton, M. (2005). The role of radiotherapy in cancer treatment. Cancer *104*, 1129–1137.

Dondelinger, Y., Darding, M., Bertrand, M.J.M., and Walczak, H. (2016). Poly-ubiquitination in TNFR1-mediated necroptosis. Cell. Mol. Life Sci. *73*, 2165–2176.

Donepudi, M., Sweeney, A. Mac, Briand, C., and Grütter, M.G. (2003). Insights into the Regulatory Mechanism for Caspase-8 Activation. Mol. Cell *11*, 543–549.

Dora, D., Rivard, C., Yu, H., Bunn, P., Suda, K., Ren, S., Lueke Pickard, S., Laszlo, V., Harko, T., Megyesfalvi, Z., et al. (2020). Neuroendocrine subtypes of small cell lung cancer differ in terms of immune microenvironment and checkpoint molecule distribution. Mol. Oncol. *14*, 1947–1965.

Draber, P., Kupka, S., Reichert, M., Draberova, H., Lafont, E., de Miguel, D., Spilgies, L., Surinova, S., Taraborrelli, L., Hartwig, T., et al. (2015). LUBAC-Recruited CYLD and A20 Regulate Gene Activation and Cell Death by Exerting Opposing Effects on Linear Ubiquitin in Signaling Complexes. Cell Rep. *13*, 2258–2272.

Etemadi, N., Chopin, M., Anderton, H., Tanzer, M.C., Rickard, J.A., Abeysekera, W., Hall, C., Spall, S.K., Wang, B., Xiong, Y., et al. (2015). TRAF2 regulates TNF and NF-κB signalling to suppress apoptosis and skin inflammation independently of sphingosine kinase. Elife *4*.

Eydgahi, H., Chen, W.W., Muhlich, J.L., Vitkup, D., Tsitsiklis, J.N., and Sorger, P.K. (2013). Properties of cell death models calibrated and compared using Bayesian approaches. Mol. Syst. Biol. *9*, 644.

Feltham, R., Vince, J.E., and Lawlor, K.E. (2017). Caspase-8: not so silently deadly. Clin. Transl. Immunol. *6*, e124.

Feng, S., Yang, Y., Mei, Y., Ma, L., Zhu, D., Hoti, N., Castanares, M., and Wu, M. (2007). Cleavage of RIP3 inactivates its caspase-independent apoptosis pathway by removal of kinase

domain. Cell. Signal. *19*, 2056–2067.

Feoktistova, M., Geserick, P., Kellert, B., Dimitrova, D.P., Langlais, C., Hupe, M., Cain, K., MacFarlane, M., Häcker, G., and Leverkus, M. (2011). CIAPs Block Ripoptosome Formation, a RIP1/Caspase-8 Containing Intracellular Cell Death Complex Differentially Regulated by cFLIP Isoforms. Mol. Cell *43*, 449–463.

Feoktistova, M., Makarov, R., Brenji, S., Schneider, A.T., Hooiveld, G.J., Luedde, T., Leverkus, M., Yazdi, A.S., and Panayotova-Dimitrova, D. (2020). A20 Promotes Ripoptosome Formation and TNF-Induced Apoptosis via cIAPs Regulation and NIK Stabilization in Keratinocytes. Cells 2020, Vol. 9, Page 351 *9*, 351.

Füllsack, S., Rosenthal, A., Wajant, H., and Siegmund, D. (2019). Redundant and receptor-specific activities of TRADD, RIPK1 and FADD in death receptor signaling. *10*, 1–19.

Furuta, M., Sakakibara-Konishi, J., Kikuchi, H., Yokouchi, H., Nishihara, H., Minemura, H., Harada, M., Yamazaki, S., Akie, K., Fujita, Y., et al. (2019). Analysis of DLL3 and ASCL1 in Surgically Resected Small Cell Lung Cancer (HOT1702). Oncologist *24*.

Gabadinho, A., Ritschard, G., Müller, N.S., and Studer, M. (2011). Analyzing and Visualizing State Sequences in R with TraMineR. J. Stat. Softw. *40*, 1–37.

Galluzzo, P., and Bocchetta, M. (2014). Notch signaling in lung cancer. Http://Dx.Doi.Org/10.1586/Era.10.158 *11*, 533–540.

Gao, J., Aksoy, B.A., Dogrusoz, U., Dresdner, G., Gross, B., Sumer, S.O., Sun, Y., Jacobsen, A., Sinha, R., Larsson, E., et al. (2013). Integrative analysis of complex cancer genomics and clinical profiles using the cBioPortal. Sci. Signal. *6*.

Gay, C.M., Stewart, C.A., Park, E.M., Diao, L., Groves, S.M., Heeke, S., Nabet, B.Y., Fujimoto, J., Solis, L.M., Lu, W., et al. (2021). Patterns of transcription factor programs and immune pathway activation define four major subtypes of SCLC with distinct therapeutic vulnerabilities. Cancer Cell *39*, 346-360.e7.

Gazdar, A.F., Carney, D.N., Nau, M.M., and Minna, J.D. (1985). Characterization of Variant Subclasses of Cell Lines Derived from Small Cell Lung Cancer Having Distinctive Biochemical, Morphological, and Growth Properties. Cancer Res. *45*.

Gazdar, A.F., Bunn, P.A., and Minna, J.D. (2017). Small-cell lung cancer: What we know, what

we need to know and the path forward (Nature Publishing Group).

George, J., Lim, J.S., Jang, S.J., Cun, Y., Ozretia, L., Kong, G., Leenders, F., Lu, X., Fernández-Cuesta, L., Bosco, G., et al. (2015). Comprehensive genomic profiles of small cell lung cancer. Nature *524*, 47–53.

Gillies, R.J., Verduzco, D., and Gatenby, R.A. (2012). Evolutionary dynamics of carcinogenesis and why targeted therapy does not work. Nat. Rev. Cancer *12*, 487–493.

Gong, Y., Fan, Z., Luo, G., Yang, C., Huang, Q., Fan, K., Cheng, H., Jin, K., Ni, Q., Yu, X., et al. (2019). The role of necroptosis in cancer biology and therapy.

Grootjans, S., Vanden Berghe, T., and Vandenabeele, P. (2017). Initiation and execution mechanisms of necroptosis: an overview. Cell Death Differ. 2017 247 *24*, 1184–1195.

Groves, S.M., Ireland, A., Liu, Q., Simmons, A.J., Lau, K., Iams, W.T., Tyson, D., Lovly, C.M., Oliver, T.G., and Quaranta, V. (2021). Cancer Hallmarks Define a Continuum of Plastic Cell States between Small Cell Lung Cancer Archetypes. BioRxiv 2021.01.22.427865.

Gurung, P., Man, S.M., and Kanneganti, T.-D. (2015). A20 is a regulator of necroptosis. Nat. Immunol. *16*, 596–597.

Haas, T.L., Emmerich, C.H., Gerlach, B., Schmukle, A.C., Cordier, S.M., Rieser, E., Feltham, R., Vince, J., Warnken, U., Wenger, T., et al. (2009). Recruitment of the linear ubiquitin chain assembly complex stabilizes the TNF-R1 signaling complex and is required for TNF-mediated gene induction. Mol. Cell *36*, 831–844.

Hanahan, D. (2022). Hallmarks of Cancer: New Dimensions. Cancer Discov. *12*, 31–46.

Hanahan, D., and Weinberg, R.A. (2000). The hallmarks of cancer. Cell *100*, 57–70.

Hanahan, D., and Weinberg, R.A.A. (2011). Hallmarks of cancer: the next generation. Cell *144*, 646–674.

Harris, L.A.L.A., Nobile, M.S.M.S., Pino, J.C.J.C., Lubbock, A.L.R.A.L.R., Besozzi, D., Mauri, G., Cazzaniga, P., and Lopez, C.F.C.F. (2017). GPU-powered model analysis with PySB/cupSODA. Bioinformatics *33*, 3492–3494.

Hausser, J., Szekely, P., Bar, N., Zimmer, A., Sheftel, H., Caldas, C., and Alon, U. (2019). Tumor diversity and the trade-off between universal cancer tasks. Nat. Commun. 2019 101 *10*,

1–13.

He, K.-L., and Ting, A.T. (2002). A20 Inhibits Tumor Necrosis Factor (TNF) Alpha-Induced Apoptosis by Disrupting Recruitment of TRADD and RIP to the TNF Receptor 1 Complex in Jurkat T Cells. Mol. Cell. Biol. *22*, 6034–6045.

He, S., Wang, L., Miao, L., Wang, T., Du, F., Zhao, L., and Wang, X. (2009). Receptor Interacting Protein Kinase-3 Determines Cellular Necrotic Response to TNF-α. Cell *137*, 1100–1111.

Heiser, C.N., Wang, V.M., Chen, B., Hughey, J.J., and Lau, K.S. (2021). Automated quality control and cell identification of droplet-based single-cell data using dropkick. Genome Res. *31*, 1742–1752.

Hitomi, J., Christofferson, D.E., Ng, A., Yao, J., Degterev, A., Xavier, R.J., and Yuan, J. (2008). Identification of a Molecular Signaling Network that Regulates a Cellular Necrotic Cell Death Pathway. Cell *135*, 1311–1323.

Hori, K., Sen, A., and Artavanis-Tsakonas, S. (2013). Notch signaling at a glance. J. Cell Sci. *126*, 2135–2140.

Horn, F., and Jackson, R. (1972). General mass action kinetics. Arch. Ration. Mech. Anal. *47*, 81–116.

Hsu, H., Shu, H.-B.B., Pan, M.-G.G., and Goeddel, D. V. (1996a). TRADD–TRAF2 and TRADD–FADD Interactions Define Two Distinct TNF Receptor 1 Signal Transduction Pathways. Cell *84*, 299–308.

Hsu, H., Huang, J., Shu, H.B., Baichwal, V., and Goeddel, D. V. (1996b). TNF-dependent recruitment of the protein kinase RIP to the TNF receptor-1 signaling complex. Immunity *4*, 387–396.

Hua, F., Cornejo, M.G., Cardone, M.H., Stokes, C.L., and Lauffenburger, D.A. (2005). Effects of Bcl-2 levels on Fas signaling-induced caspase-3 activation: molecular genetic tests of computational model predictions. J. Immunol. *175*, 985–995.

Huang, R.S.P., Holmes, B.F., Powell, C., Marati, R. V., Tyree, D., Admire, B., Streator, A., Hanlon Newell, A.E., Perez, J., Dalvi, D., et al. (2019). Delta-like Protein 3 Prevalence in Small Cell Lung Cancer and DLL3 (SP347) Assay Characteristics. Arch. Pathol. Lab. Med. *143*, 1373–

1377.

Huang, Y.H., Klingbeil, O., He, X.Y., Wu, X.S., Arun, G., Lu, B., Somerville, T.D.D., Milazzo, J.P., Wilkinson, J.E., Demerdash, O.E., et al. (2018). POU2F3 is a master regulator of a tuft cell-like variant of small cell lung cancer. Genes Dev. *32*, 915–928.

Hucka, M., Finney, A., Sauro, H.M., Bolouri, H., Doyle, J.C., Kitano, H., Arkin, A.P., Bornstein, B.J., Bray, D., Cornish-Bowden, A., et al. (2003). The systems biology markup language (SBML): a medium for representation and exchange of biochemical network models. Bioinformatics *19*, 524–531.

Hurtado, C., Safarova, A., Smith, M., Chung, R., Bruyneel, A.A.N., Gomez-Galeno, J., Oswald, F., Larson, C.J., Cashman, J.R., Ruiz-Lozano, P., et al. (2019). Disruption of NOTCH signaling by a small molecule inhibitor of the transcription factor RBPJ. Sci. Reports 2019 91 *9*, 1–9.

Ideker, T., Thorsson, V., Ranish, J.A., Christmas, R., Buhler, J., Eng, J.K., Bumgarner, R., Goodlett, D.R., Aebersold, R., and Hood, L. (2001). Integrated genomic and proteomic analyses of a systematically perturbed metabolic network. Science (80-.). *292*, 929–934.

Ildefonso, G. V, Metzig, M.O., Hoffmann, A., Harris, L.A., and Lopez, C.F. (2022). Distinct execution modes of a biochemical necroptosis model explain cell type-specific responses and variability to cell-death cues. BioRxiv 2022.02.25.481705.

Indraccolo, S., Minuzzo, S., Masiero, M., Pusceddu, I., Persano, L., Moserle, L., Reboldi, A., Favaro, E., Mecarozzi, M., Di Mario, G., et al. (2009). Cross-talk between tumor and endothelial cells involving the Notch3-Dll4 interaction marks escape from tumor dormancy. Cancer Res. *69*, 1314–1323.

Ireland, A.S., Micinski, A.M., Kastner, D.W., Guo, B., Wait, S.J., Spainhower, K.B., Conley, C.C., Chen, O.S., Guthrie, M.R., Soltero, D., et al. (2020). MYC Drives Temporal Evolution of Small Cell Lung Cancer Subtypes by Reprogramming Neuroendocrine Fate. Cancer Cell *38*, 60-78.e12.

Iyengar, R., Zhao, S., Chung, S.W., Mager, D.E., and Gallo, J.M. (2012). Merging systems biology with pharmacodynamics. Sci. Transl. Med. *4*, 126–133.

Jensen, H.J. (1998). Self-Organized Criticality: Emergent Complex Behavior in Physical and Biological Systems.

Kageyama, R., and Ohtsuka, T. (1999). The Notch-Hes pathway in mammalian neural development. Cell Res. *9*, 179–188.

Karr, J.R., Takahashi, K., and Funahashi, A. (2015). The principles of whole-cell modeling. Curr. Opin. Microbiol. *27*, 18–24.

Karr, J.R., Sanghvi, J.C., Macklin, D.N., Gutschow, M. V, Jacobs, J.M., Bolival, B., Assad-Garcia, N., Glass, J.I., and Covert, M.W. (2018). A Whole-Cell Computational Model Predicts Phenotype from Genotype. Cell *150*, 389–401.

Kearney, C.J., Cullen, S.P., Tynan, G.A., Henry, C.M., Clancy, D., Lavelle, E.C., and Martin, S.J. (2015). Necroptosis suppresses inflammation via termination of TNF-or LPS-induced cytokine and chemokine production. Cell Death Differ. *22*, 1313–1327.

Kearns, J.D., Basak, S., Werner, S.L., Huang, C.S., and Hoffmann, A. (2006). IkappaBepsilon provides negative feedback to control NF-kappaB oscillations, signaling dynamics, and inflammatory gene expression. J. Cell Biol. *173*, 659–664.

Keating, S.M., Waltemath, D., König, M., Zhang, F., Dräger, A., Chaouiya, C., Bergmann, F.T., Finney, A., Gillespie, C.S., Helikar, T., et al. (2020). SBML Level 3: an extensible format for the exchange and reuse of biological models. Mol. Syst. Biol. *16*, e9110.

Kim, T.K. (2015). T test as a parametric statistic. Korean J. Anesthesiol. *68*, 540.

Kitano, H. (2002). Systems biology: A brief overview (American Association for the Advancement of Science).

Ko, J., Winslow, M.M., and Sage, J. (2021). Mechanisms of small cell lung cancer metastasis. EMBO Mol. Med. *13*, e13122.

Koch, U., and Radtke, F. (2007). Notch and cancer: A double-edged sword. Cell. Mol. Life Sci. *64*, 2746–2762.

Kochen, M.A., and Lopez, C.F. (2020). A Probabilistic Approach to Explore Signal Execution Mechanisms With Limited Experimental Data. Front. Genet. *11*, 686.

Kolczyk, K., and Conradi, C. (2016). Challenges in horizontal model integration. BMC Syst. Biol. *10*, 28.

Kopan, R. (2012). Notch Signaling. Cold Spring Harb. Perspect. Biol. *4*.

Kovalenko, A., Chable-Bessia, C., Cantarella, G., Israël, A., Wallach, D., and Courtois, G. (2003). The tumour suppressor CYLD negatively regulates NF-κB signalling by deubiquitination. Nature *424*, 801–805.

L., O., Z., S., S., Z., F.-T., W., T.-T., Z., B., L., J.-K., B., Ouyang, L., Shi, Z., Zhao, S., et al. (2012). Programmed cell death pathways in cancer: a review of apoptosis, autophagy and programmed necrosis. Cell Prolif. *45*, 487–498.

L, M., K, K., L, O., AM, S., F, U., CP, A., K, A., D, B., U, R.-F., A, F., et al. (2016). NOTCH, ASCL1, p53 and RB alterations define an alternative pathway driving neuroendocrine and small cell lung carcinomas. Int. J. Cancer *138*, 927–938.

Lake, R.J., Tsai, P.F., Choi, I., Won, K.J., and Fan, H.Y. (2014). RBPJ, the Major Transcriptional Effector of Notch Signaling, Remains Associated with Chromatin throughout Mitosis, Suggesting a Role in Mitotic Bookmarking. PLOS Genet. *10*, e1004204.

Lander, E.S., Linton, L.M., Birren, B., Nusbaum, C., Zody, M.C., Baldwin, J., Devon, K., Dewar, K., Doyle, M., Fitzhugh, W., et al. (2001). Initial sequencing and analysis of the human genome. Nat. 2001 4096822 *409*, 860–921.

Lawrence, C.P., and Chow, S.C. (2005). FADD deficiency sensitises Jurkat T cells to TNF-α-dependent necrosis during activation-induced cell death. FEBS Lett. *579*, 6465–6472.

Lawson, M.J., Petzold, L., and Hellander, A. (2015). Accuracy of the Michaelis–Menten approximation when analysing effects of molecular noise. J. R. Soc. Interface *12*.

Leonetti, A., Facchinetti, F., Minari, R., Cortellini, A., Rolfo, C.D., Giovannetti, E., and Tiseo, M. (2019). Notch pathway in small-cell lung cancer: from preclinical evidence to therapeutic challenges. Cell. Oncol. *42*, 261–273.

Li, M., and Beg, A.A. (2000). Induction of necrotic-like cell death by tumor necrosis factor alpha and caspase inhibitors: novel mechanism for killing virus-infected cells. J. Virol. *74*, 7470–7477.

Lim, J.S., Ibaseta, A., Fischer, M.M., Cancilla, B., O'Young, G., Cristea, S., Luca, V.C., Yang, Di., Jahchan, N.S., Hamard, C., et al. (2017). Intratumoural heterogeneity generated by Notch signalling promotes small-cell lung cancer. *545*, 360–364.

Liu, S., Wang, X., Li, Y., Xu, L., Yu, X., Ge, L., Li, J., Zhu, Y., and He, S. (2014). Necroptosis Mediates TNF-Induced Toxicity of Hippocampal Neurons. Biomed Res. Int. *2014*.

Liu, X., Shi, F., Li, Y., Yu, X., Peng, S., Li, W., Luo, X., and Cao, Y. (2016). Post-translational modifications as key regulators of TNF-induced necroptosis. Cell Death Dis. *7*, e2293.

Liu, Z., Brunskill, E., Varnum-Finney, B., Zhang, C., Zhang, A., Jay, P.Y., Bernstein, I., Morimoto, M., and Kopan, R. (2015). The intracellular domains of Notch1 and Notch2 are functionally equivalent during development and carcinogenesis. Dev. *142*, 2452–2463.

Lobov, I.B., Renard, R.A., Papadopoulos, N., Gale, N.W., Thurston, G., Yancopoulos, G.D., and Wiegand, S.J. (2007). Delta-like ligand 4 (Dll4) is induced by VEGF as a negative regulator of angiogenic sprouting. Proc. Natl. Acad. Sci. U. S. A. *104*, 3219–3224.

Lopez, C.F., Muhlich, J.L., Bachman, J.A., and Sorger, P.K. (2013). Programming biological models in Python using PySB. Mol. Syst. Biol. *9*, 646.

Lork, M., Verhelst, K., and Beyaert, R. (2017). CYLD, A20 and OTULIN deubiquitinases in NF-κB signaling and cell death: So similar, yet so different. Cell Death Differ. *24*, 1172–1183.

Lu, T.T., Onizawa, M., Hammer, G.E., Turer, E.E., Yin, Q., Damko, E., Agelidis, A., Shifrin, N., Advincula, R., Barrera, J., et al. (2013). Dimerization and Ubiquitin Mediated Recruitment of A20, a Complex Deubiquitinating Enzyme. Immunity *38*, 896–905.

Von Luxburg, U. (2007). A tutorial on spectral clustering. Stat. Comput. 2007 174 *17*, 395–416.

La Manno, G., Soldatov, R., Zeisel, A., Braun, E., Hochgerner, H., Petukhov, V., Lidschreiber, K., Kastriti, M.E., Lönnerberg, P., Furlan, A., et al. (2018). RNA velocity of single cells. Nat. 2018 5607719 *560*, 494–498.

Marini, F., and Walczak, B. (2015). Particle swarm optimization (PSO). A tutorial. Chemom. Intell. Lab. Syst. *149*, 153–165.

Mayer, P., Mayer, B., and Mayer, G. (2012). Systems biology: building a useful model from multiple markers and profiles. Nephrol. Dial. Transplant. Off. Publ. Eur. Dial. Transpl. Assoc. - Eur. Ren. Assoc. *27*, 3995–4002.

McComb, S., Cheung, H.H., Korneluk, R.G., Wang, S., Krishnan, L., and Sad, S. (2012). cIAP1 and cIAP2 limit macrophage necroptosis by inhibiting Rip1 and Rip3 activation. Cell Death Differ. *19*, 1791–1801.

McIlwain, D.R., Berger, T., and Mak, T.W. (2013). Caspase Functions in Cell Death and

Disease. Cold Spring Harb. Perspect. Biol. *5*, a008656.

Meder, L., Büttner, R., and Odenthal, M. (2017). Notch signaling triggers the tumor heterogeneity of small cell lung cancer (AME Publishing Company).

Meng, M.-B., Wang, H.-H., Cui, Y.-L., Wu, Z.-Q., Shi, Y.-Y., Zaorsky, N.G., Deng, L., Yuan, Z.-Y., Lu, Y., Wang, P., et al. (2016). Necroptosis in tumorigenesis, activation of anti-tumor immunity, and cancer therapy. Oncotarget *7*, 57391–57413.

Metzig, M.O., Tang, Y., Mitchell, S., Taylor, B., Foreman, R., Wollman, R., and Hoffmann, A. (2020). An incoherent feedforward loop interprets NFκB/RelA dynamics to determine TNF-induced necroptosis decisions. Mol. Syst. Biol. *16*, e9677.

Micheau, O., and Tschopp, J. (2003). Induction of TNF receptor I-mediated apoptosis via two sequential signaling complexes. Cell *114*, 181–190.

Micheau, O., Thome, M., Schneider, P., Holler, N., Tschopp, J., Nicholson, D.W., Briand, C., and Grütter, M.G. (2002). The Long Form of FLIP Is an Activator of Caspase-8 at the Fas Death-inducing Signaling Complex. J. Biol. Chem. *277*, 45162–45171.

Miele, L. (2006). Notch signaling. Clin. Cancer Res. *12*, 1074–1079.

Milo, R., Jorgensen, P., Moran, U., Weber, G., and Springer, M. (2009). BioNumbers—the database of key numbers in molecular and cell biology. Nucleic Acids Res. *38*, D750–D753.

Miyamoto, A., and Weinmaster, G. (2009). Notch Signal Transduction: Molecular and Cellular Mechanisms. Encycl. Neurosci. 1259–1268.

Mohtashami, M., Shah, D.K., Nakase, H., Kianizad, K., Petrie, H.T., and Zúñiga-Pflücker, J.C. (2010). Direct comparison of Dll1- and Dll4-mediated Notch activation levels shows differential lymphomyeloid lineage commitment outcomes. J. Immunol. *185*, 867–876.

Molnár, T., Mázló, A., Tslaf, V., Szöllősi, A.G., Emri, G., and Koncz, G. (2019). Current translational potential and underlying molecular mechanisms of necroptosis. Cell Death Dis. *10*, 1–21.

Moquin, D.M., McQuade, T., and Chan, F.K.-M.M. (2013). CYLD Deubiquitinates RIP1 in the TNFα-Induced Necrosome to Facilitate Kinase Activation and Programmed Necrosis. PLoS One *8*, e76841.

Morgensztern, D., Besse, B., Greillier, L., Santana-Davila, R., Ready, N., Hann, C.L., Glisson, B.S., Farago, A.F., Dowlati, A., Rudin, C.M., et al. (2019). Efficacy and safety of rovalpituzumab tesirine in third-line and beyond patients with DLL3-expressing, relapsed/refractory small-cell lung cancer: Results from the phase II TrINITY study. Clin. Cancer Res. *25*, 6958–6966.

Moriwaki, K., and Chan, F.K.-M. (2013). RIP3: a molecular switch for necrosis and inflammation. Genes Dev. *27*.

Moriwaki, K., Bertin, J., Gough, P.J., Orlowski, G.M., and Chan, F.K. (2015). Differential roles of RIPK1 and RIPK3 in TNF-induced necroptosis and chemotherapeutic agent-induced cell death. Cell Death Dis. *6*, e1636.

Moriya, H. (2015). Quantitative nature of overexpression experiments. Mol. Biol. Cell *26*, 3932.

Mortlock, R.D., Georgia, S.K., and Finley, S.D. (2021). Dynamic Regulation of JAK-STAT Signaling Through the Prolactin Receptor Predicted by Computational Modeling. Cell. Mol. Bioeng. *14*, 15–30.

Murphy, J.M.M., Czabotar, P.E.E., Hildebrand, J.M.M., Lucet, I.S.S., Zhang, J.-G.G., Alvarez-Diaz, S., Lewis, R., Lalaoui, N., Metcalf, D., Webb, A.I.I., et al. (2013). The Pseudokinase MLKL Mediates Necroptosis via a Molecular Switch Mechanism. Immunity *39*, 443–453.

Najafov, A., Mookhtiar, A.K., Luu, H.S., Ordureau, A., Pan, H., Amin, P.P., Li, Y., Lu, Q., and Yuan, J. (2019). TAM Kinases Promote Necroptosis by Regulating Oligomerization of MLKL. Mol. Cell *75*, 457-468.e4.

Nandagopal, N., Santat, L.A., LeBon, L., Sprinzak, D., Bronner, M.E., and Elowitz, M.B. (2018). Dynamic Ligand Discrimination in the Notch Signaling Pathway. Cell *172*, 869-880.e19.

Nandagopal, N., Santat, L.A., and Elowitz, M.B. (2019). Cis-activation in the Notch signaling pathway. Elife *8*.

Nelson, B.R., Hartman, B.H., Ray, C.A., Hayashi, T., Bermingham-McDonogh, O., and Reh, T.A. (2009). Acheate-scute like 1 (Ascl1) is required for normal Delta-like (Dll) gene expression and Notch signaling during retinal development. Dev. Dyn. *238*, 2163.

Nelson, D.E., Ihekwaba, A.E.C., Elliott, M., Johnson, J.R., Gibney, C.A., Foreman, B.E., Nelson, G., See, V., Horton, C.A., Spiller, D.G., et al. (2004). Oscillations in NF-κB Signaling Control the Dynamics of Gene Expression. Science (80-.). *306*, 704–708.

Nikoletopoulou, V., Markaki, M., Palikaras, K., and Tavernarakis, N. (2013). Crosstalk between apoptosis, necrosis and autophagy. Biochim. Biophys. Acta - Mol. Cell Res. *1833*, 3448–3459.

Le Novère, N., and Endler, L. (2013). Using chemical kinetics to model biochemical pathways. Methods Mol. Biol. *1021*, 147–167.

Ntziachristos, P., Lim, J.S., Sage, J., and Aifantis, I. (2014). From fly wings to targeted cancer therapies: a centennial for notch signaling. Cancer Cell *25*, 318–334.

O'Donnell, M.A., and Ting, A.T. (2011). RIP1 comes back to life as a cell death regulator in TNFR1 signaling. FEBS J. *278*, 877–887.

Oberst, A., Dillon, C.P., Weinlich, R., McCormick, L.L., Fitzgerald, P., Pop, C., Hakem, R., Salvesen, G.S., and Green, D.R. (2011). Catalytic activity of the caspase-8–$FLIP_L$ complex inhibits RIPK3-dependent necrosis. Nature *471*, 363–367.

Ortega, O.O., Wilson, B.A., Pino, J.C., Irvin, M.W., Garbett, S.P., Lopez, C.F., Ildefonso, G.V., Garbett, S.P., and Lopez, C.F. (2021). Probability-based mechanisms in biological networks with parameter uncertainty. BioRxiv 2021.01.26.428266.

Ouadah, Y., Rojas, E.R., Riordan, D.P., Capostagno, S., Kuo, C.S., and Krasnow, M.A. (2019). Rare Pulmonary Neuroendocrine Cells Are Stem Cells Regulated by Rb, p53, and Notch. Cell *179*, 403-416.e23.

Owen, D.H., Giffin, M.J., Bailis, J.M., Smit, M.A.D., Carbone, D.P., and He, K. (2019). DLL3: An emerging target in small cell lung cancer. J. Hematol. Oncol. *12*, 1–8.

Pasparakis, M., and Vandenabeele, P. (2015). Necroptosis and its role in inflammation. Nature *517*, 311–320.

Patel, A.S., Yoo, S., Kong, R., Sato, T., Sinha, A., Karam, S., Bao, L., Fridrikh, M., Emoto, K., Nudelman, G., et al. (2021). Prototypical oncogene family Myc defines unappreciated distinct lineage states of small cell lung cancer. Sci. Adv. *7*.

Pedrosa, A.R., Trindade, A., Fernandes, A.C., Carvalho, C., Gigante, J., Tavares, A.T., Diéguez-Hurtado, R., Yagita, H., Adams, R.H., and Duarte, A. (2015). Endothelial jagged1 antagonizes Dll4 regulation of endothelial branching and promotes vascular maturation downstream of Dll4/Notch1. Arterioscler. Thromb. Vasc. Biol. *35*, 1134–1146.

Petzold, L. (1983). Automatic selection of methods for solving stiff and nonstiff systems of ordinary differential equations. SIAM J. Sci. Stat. Comput. *4*, 136–148.

Pobezinskaya, Y.L., and Liu, Z. (2012). The role of TRADD in death receptor signaling. Cell Cycle *11*, 871–876.

Poirier, J.T., Dobromilskaya, I., Moriarty, W.F., Peacock, C.D., Hann, C.L., and Rudin, C.M. (2013). Selective tropism of Seneca Valley virus for variant subtype small cell lung cancer. J. Natl. Cancer Inst. *105*, 1059–1065.

Roca, C., and Adams, R.H. (2007). Regulation of vascular morphogenesis by Notch signaling. Genes Dev. *21*, 2511–2524.

Rohrs, J.A., Siegler, E.L., Wang, P., and Finley, S.D. (2020). ERK Activation in CAR T Cells Is Amplified by CD28-Mediated Increase in CD3ζ Phosphorylation. IScience *23*, 101023.

Rokach, L., and Maimon, O. (2005). Clustering Methods. Data Min. Knowl. Discov. Handb. 321–352.

Ronan, T., Qi, Z., Naegle, K.M., Jain, A.K., Murty, M.N., Flynn, P.J., Xu, R., Wunsch, D.C., Andreopoulos, B., An, A., et al. (2016). Avoiding common pitfalls when clustering biological data. Sci. Signal. *9*, re6.

Rousseeuw, P.J. (1987). Silhouettes: A graphical aid to the interpretation and validation of cluster analysis. J. Comput. Appl. Math. *20*, 53–65.

Rubin, M.A., Bristow, R.G., Thienger, P.D., Dive, C., and Imielinski, M. (2020). Impact of Lineage Plasticity to and from a Neuroendocrine Phenotype on Progression and Response in Prostate and Lung Cancers. Mol. Cell *80*, 562–577.

Rudin, C.M., Poirier, J.T., Byers, L.A., Dive, C., Dowlati, A., George, J., Heymach, J. V., Johnson, J.E., Lehman, J.M., MacPherson, D., et al. (2019). Molecular subtypes of small cell lung cancer: a synthesis of human and mouse model data. Nat. Rev. Cancer *19*, 289–297.

Sai, K., Parsons, C., House, J.S., Kathariou, S., and Ninomiya-Tsuji, J. (2019). Necroptosis mediators RIPK3 and MLKL suppress intracellular Listeria replication independently of host cell killing. J. Cell Biol. *218*, 1994–2005.

Sainson, R.C.A., and Harris, A.L. (2008). Regulation of angiogenesis by homotypic and

heterotypic notch signalling in endothelial cells and pericytes: from basic research to potential therapies. Angiogenesis *11*, 41–51.

Samson, A.L., Zhang, Y., Geoghegan, N.D., Gavin, X.J., Davies, K.A., Mlodzianoski, M.J., Whitehead, L.W., Frank, D., Garnish, S.E., Fitzgibbon, C., et al. (2020). MLKL trafficking and accumulation at the plasma membrane control the kinetics and threshold for necroptosis. *11*.

Samson, A.L., Garnish, S.E., Hildebrand, J.M., and Murphy, J.M. (2021). Location, location, location: A compartmentalized view of TNF-induced necroptotic signaling. Sci. Signal. *14*, 6178.

Sasnauskiene, A., Jonusˇiene, V., Kriksˇtaponiene, A., Butkyte, S., Dabkevicˇiene, D., Kanopiene, D., Kazbariene, B., and Didzˇiapetriene, J. (2014). NOTCH1, NOTCH3, NOTCH4, and JAG2 protein levels in human endometrial cancer. Medicina (Kaunas). *50*, 14–18.

Schulz, M., Uhlendorf, J., Klipp, E., and Liebermeister, W. (2006). SBMLmerge, a system for combining biochemical network models. Genome Inform. *17*, 62–71.

Schwendenwein, A., Megyesfalvi, Z., Barany, N., Valko, Z., Bugyik, E., Lang, C., Ferencz, B., Paku, S., Lantos, A., Fillinger, J., et al. (2021). Molecular profiles of small cell lung cancer subtypes: Therapeutic implications. Mol. Ther. - Oncolytics *20*, 470–483.

Seo, J., Nam, Y.W., Kim, S., Oh, D.B., and Song, J. (2021). Necroptosis molecular mechanisms: Recent findings regarding novel necroptosis regulators. Exp. Mol. Med. 2021 536 *53*, 1007–1017.

Sevimoglu, T., and Arga, K.Y. (2014). The role of protein interaction networks in systems biomedicine. Comput. Struct. Biotechnol. J. *11*, 22–27.

Shamir, M., Bar-On, Y., Phillips, R., and Milo, R. (2016). Characteristic rates and timescales in cell biology. Cell *164*, 1302-1302.e1.

Shih, V.F.-S., Kearns, J.D., Basak, S., Savinova, O. V, Ghosh, G., and Hoffmann, A. (2017). Proceedings of the National Academy of Sciences. Proc. Natl. Acad. Sci.

Shockley, E.M., Vrugt, J.A., Lopez, C.F., and Valencia, A. (2018). PyDREAM: high-dimensional parameter inference for biological models in python. Bioinformatics *34*, 695–697.

Simonson, S.J.S., Wu, Z.H., and Miyamoto, S. (2007). CYLD: A DUB with Many Talents. Dev. Cell *13*, 601–603.

Simpson, K.L., Stoney, R., Frese, K.K., Simms, N., Rowe, W., Pearce, S.P., Humphrey, S., Booth, L., Morgan, D., Dynowski, M., et al. (2020). A biobank of small cell lung cancer CDX models elucidates inter- and intratumoral phenotypic heterogeneity. Nat. Cancer 2020 14 *1*, 437–451.

Singla, J., and White, K.L. (2021). A community approach to whole-cell modeling. Curr. Opin. Syst. Biol. *26*, 33–38.

Somasundaram, K., Reddy, S.P., Vinnakota, K., Britto, R., Subbarayan, M., Nambiar, S., Hebbar, A., Samuel, C., Shetty, M., Sreepathi, H.K., et al. (2005). Upregulation of ASCL1 and inhibition of Notch signaling pathway characterize progressive astrocytoma. Oncogene 2005 2447 *24*, 7073–7083.

Song, M., and Finley, S.D. (2020). ERK and Akt exhibit distinct signaling responses following stimulation by pro-angiogenic factors. Cell Commun. Signal. *18*, 1–19.

Spencer, S.L., Gaudet, S., Albeck, J.G., Burke, J.M., and Sorger, P.K. (2009). Non-genetic origins of cell-to-cell variability in TRAIL-induced apoptosis. Nature *459*, 428–432.

Sprinzak, D., and Blacklow, S.C. (2021). Annual Review of Biophysics Biophysics of Notch Signaling.

Sriuranpong, V., Borges, M.W., Ravi, R.K., Arnold, D.R., D., N.B., and Ball W., D. (2001). Notch Signaling Induces Cell Cycle Arrest in Small Cell Lung Cancer Cells. Cancer Res. *61*, 3200–3205.

Stelling, J., Sauer, U., Szallasi, Z., Doyle, F.J., and Doyle, J. (2004). Robustness of cellular functions. Cell *118*, 675–685.

Stokes, L., and Lauffenburger, D.A. (2022). Model Predictions Molecular Genetic Tests of Computational Signaling-Induced Caspase-3 Activation: Effects of Bcl-2 Levels on Fas.

Strasser, A., Jost, P.J., and Nagata, S. (2009). The many roles of FAS receptor signaling in the immune system. Immunity *30*, 180–192.

Studer, M., and Ritschard, G. (2016). What matters in differences between life trajectories: a comparative review of sequence dissimilarity measures. J. R. Stat. Soc. Ser. A Stat. Soc. *179*, 481–511.

Sun, S.C. (2020). A20 restricts inflammation via ubiquitin binding. Nat. Immunol. *21*, 362–364.

Sun, L., Wang, H., Wang, Z., He, S., Chen, S., Liao, D., Wang, L., Yan, J., Liu, W., Lei, X., et al. (2012). Mixed lineage kinase domain-like protein mediates necrosis signaling downstream of RIP3 kinase. Cell *148*, 213–227.

Sundstrøm, S., Bremnes, R.M., Kaasa, S., Aasebø, U., Hatlevoll, R., Dahle, R., Boye, N., Wang, M., Vigander, T., Vilsvik, J., et al. (2002). Cisplatin and etoposide regimen is superior to cyclophosphamide, epirubicin, and vincristine regimen in small-cell lung cancer: results from a randomized phase III trial with 5 years' follow-up. J. Clin. Oncol. *20*, 4665–4672.

T, O., M, I., G, G., S, N., F, G., and R, K. (1999). Hes1 and Hes5 as notch effectors in mammalian neuronal differentiation. EMBO J. *18*, 2196–2207.

Tavassoly, I., Goldfarb, J., and Iyengar, R. (2018). Systems biology primer: the basic methods and approaches. Essays Biochem. *62*, 487–500.

Taxman, D.J., Livingstone, L.R., Zhang, J., Conti, B.J., Iocca, H.A., Williams, K.L., Lich, J.D., Ting, J.P.Y., and Reed, W. (2006). Criteria for effective design, construction, and gene knockdown by shRNA vectors. BMC Biotechnol. *6*, 7.

Taylor, P., Takeuchi, H., Sheppard, D., Chillakuri, C., Lea, S.M., Haltiwanger, R.S., and Handford, P.A. (2014). Fringe-mediated extension of O-linked fucose in the ligand-binding region of Notch1 increases binding to mammalian Notch ligands. Proc. Natl. Acad. Sci. U. S. A. *111*, 7290–7295.

Tiberi, L., Van Den Ameele, J., Dimidschstein, J., Piccirilli, J., Gall, D., Herpoel, A., Bilheu, A., Bonnefont, J., Iacovino, M., Kyba, M., et al. (2012). BCL6 controls neurogenesis through Sirt1-dependent epigenetic repression of selective Notch targets. Nat. Neurosci. 2012 1512 *15*, 1627–1635.

Tsuchiya, Y., Nakabayashi, O., and Nakano, H. (2015). FLIP the Switch: Regulation of Apoptosis and Necroptosis by cFLIP. Int. J. Mol. Sci. *16*, 30321–30341.

Tveriakhina, L., Schuster-Gossler, K., Jarrett, S.M., Andrawes, M.B., Rohrbach, M., Blacklow, S.C., and Gossler, A. (2018). The ectodomains determine ligand function in vivo and selectivity of DLL1 and DLL4 toward NOTCH1 and NOTCH2 in vitro. Elife *7*.

Uhlén, M., Björling, E., Agaton, C., Szigyarto, C.A.K., Amini, B., Andersen, E., Andersson, A.C.,

Angelidou, P., Asplund, A., Asplund, C., et al. (2005). A human protein atlas for normal and cancer tissues based on antibody proteomics. Mol. Cell. Proteomics *4*, 1920–1932.

Uhlén, M., Fagerberg, L., Hallström, B.M., Lindskog, C., Oksvold, P., Mardinoglu, A., Sivertsson, Å., Kampf, C., Sjöstedt, E., Asplund, A., et al. (2015). Tissue-based map of the human proteome. Science (80-.). *347*.

Vandenabeele, P., Galluzzi, L., Vanden Berghe, T., and Kroemer, G. (2010a). Molecular mechanisms of necroptosis: an ordered cellular explosion. Nat. Rev. Mol. Cell Biol. *11*, 700–714.

Vandenabeele, P., Declercq, W., Van Herreweghe, F., and Berghe, T. Vanden (2010b). The role of the kinases RIP1 and RIP3 in TNF-induced necrosis. Sci. Signal. *3*.

Vanlangenakker, N., Bertrand, M.J.M., Bogaert, P., Vandenabeele, P., and Vanden Berghe, T. (2011a). TNF-induced necroptosis in L929 cells is tightly regulated by multiple TNFR1 complex I and II members. Cell Death Dis. *2*, e230.

Vanlangenakker, N., Vanden Berghe, T., Bogaert, P., Laukens, B., Zobel, K., Deshayes, K., Vucic, D., Fulda, S., Vandenabeele, P., and Bertrand, M.J.M.M. (2011b). cIAP1 and TAK1 protect cells from TNF-induced necrosis by preventing RIP1/RIP3-dependent reactive oxygen species production. Cell Death Differ. *18*, 656–665.

Vanlangenakker, N., Vanden Berghe, T., and Vandenabeele, P. (2012). Many stimuli pull the necrotic trigger, an overview. Cell Death Differ. *19*, 75–86.

Vercammen, D., Vandenabeele, P., Beyaert, R., Declercq, W., and Fiers, W. (1997). Tumour necrosis factor-induced necrosis versus anti-Fas-induced apoptosis in L929 cells. Cytokine *9*, 801–808.

Virtanen, P., Gommers, R., Oliphant, T.E., Haberland, M., Reddy, T., Cournapeau, D., Burovski, E., Peterson, P., Weckesser, W., Bright, J., et al. (2020). SciPy 1.0: fundamental algorithms for scientific computing in Python. Nat. Methods *17*, 261–272.

Vrugt, J.A. (2016). Markov chain Monte Carlo simulation using the DREAM software package: Theory, concepts, and MATLAB implementation. Environ. Model. Softw. *75*.

Vrugt, J.A., and Ter Braak, C.J.F. (2011). DREAM(D): An adaptive Markov Chain Monte Carlo simulation algorithm to solve discrete, noncontinuous, and combinatorial posterior parameter

estimation problems. Hydrol. Earth Syst. Sci. *15*, 3701–3713.

Wajant, H., and Siegmund, D. (2019). TNFR1 and TNFR2 in the control of the life and death balance of macrophages. Front. Cell Dev. Biol. *7*.

Wallach, D. (1984). Preparations of lymphotoxin induce resistance to their own cytotoxic effect. J. Immunol.

Wang, C.Y., Mayo, M.W., Korneluk, R.G., Goeddel, D. V, and Baldwin, A.S. (1998). NF-kappaB antiapoptosis: induction of TRAF1 and TRAF2 and c-IAP1 and c-IAP2 to suppress caspase-8 activation. Science *281*, 1680–1683.

Wang, H., Sun, L., Su, L., Rizo, J., Liu, L., Wang, L.-F.F., Wang, F.-S.S., and Wang, X. (2014). Mixed Lineage Kinase Domain-like Protein MLKL Causes Necrotic Membrane Disruption upon Phosphorylation by RIP3. Mol. Cell *54*, 133–146.

Wang, X., Guo, Y., Liu, L., Wei, J., Zhang, J., Xie, T., Dong, J., Li, J., Xing, P., and Yang, L. (2021). YAP1 protein expression has variant prognostic significance in small cell lung cancer (SCLC) stratified by histological subtypes. Lung Cancer *160*, 166–174.

Wegner, K.W., Saleh, D., and Degterev, A. (2017). Complex Pathologic Roles of RIPK1 and RIPK3: Moving Beyond Necroptosis. Trends Pharmacol. Sci. *38*, 202–225.

Werner, S.L., Kearns, J.D., Zadorozhnaya, V., Lynch, C., O'Dea, E., Boldin, M.P., Ma, A., Baltimore, D., and Hoffmann, A. (2008). Encoding NF-κB temporal control in response to TNF: distinct roles for the negative regulators IκBα and A20. Genes Dev. *22*, 2093–2101.

Wertz, I.E., O'Rourke, K.M., Zhou, H., Eby, M., Aravind, L., Seshagiri, S., Wu, P., Wiesmann, C., Baker, R., Boone, D.L., et al. (2004). De-ubiquitination and ubiquitin ligase domains of A20 downregulate NF-κB signalling. Nature *430*, 694–699.

West-Eberhard, M.J. (1989). Phenotypic Plasticity and the Origins of Diversity. Annu. Rev. Ecol. Syst. *20*, 249–278.

West-Eberhard, M.J. (2008). Phenotypic Plasticity. Encycl. Ecol. Five-Volume Set 2701–2707.

Westhoff, B., Colaluca, I.N., D'Ario, G., Donzelli, M., Tosoni, D., Volorio, S., Pelosi, G., Spaggiari, L., Mazzarol, G., Viale, G., et al. (2009). Alterations of the Notch pathway in lung cancer. Proc. Natl. Acad. Sci. U. S. A. *106*, 22293–22298.

Wolf, F.A., Angerer, P., and Theis, F.J. (2018). SCANPY: Large-scale single-cell gene expression data analysis. Genome Biol. *19*, 1–5.

Wooten, D.J., Groves, S.M., Tyson, D.R., Liu, Q., Lim, J.S., Albert, R., Lopez, C.F., Sage, J., and Quaranta, V. (2019). Systems-level network modeling of Small Cell Lung Cancer subtypes identifies master regulators and destabilizers. PLoS Comput. Biol. *15*, e1007343.

Wright, A., Reiley, W.W., Chang, M., Jin, W., Lee, A.J., Zhang, M., and Sun, S.C. (2007). Regulation of Early Wave of Germ Cell Apoptosis and Spermatogenesis by Deubiquitinating Enzyme CYLD. Dev. Cell *13*, 705–716.

Wu, Y., Dong, G., and Sheng, C. (2020). Targeting necroptosis in anticancer therapy: mechanisms and modulators (Chinese Academy of Medical Sciences).

Xie, H., Boland, J.M., Maleszewski, J.J., Aubry, M.C., Yi, E.S., Jenkins, S.M., Koepplin, J.W., Terra, S.B.S.P., Mansfield, A.S., and Roden, A.C. (2019). Expression of delta-like protein 3 is reproducibly present in a subset of small cell lung carcinomas and pulmonary carcinoid tumors. Lung Cancer *135*, 73–79.

Xie, M., Liu, M., and He, C.S. (2012). SIRT1 regulates endothelial Notch signaling in lung cancer. PLoS One *7*.

Xiu, M. xi, Liu, Y. meng, and Kuang, B. hai (2020). The oncogenic role of Jagged1/Notch signaling in cancer. Biomed. Pharmacother. *129*, 110416.

Xu, Q., Choksi, S., and Liu, Z. (2018). Switching from TNF-induced inflammation to death signaling. Mol. Cell. Oncol. *5*, e1392402.

Yan, M., and Plowman, G.D. (2007). Delta-like 4/Notch signaling and its therapeutic implications. Clin. Cancer Res. *13*, 7243–7246.

Zhang, W., Girard, L., Zhang, Y.A., Haruki, T., Papari-Zareei, M., Stastny, V., Ghayee, H.K., Pacak, K., Oliver, T.G., Minna, J.D., et al. (2018). Small cell lung cancer tumors and preclinical models display heterogeneity of neuroendocrine phenotypes. Transl. Lung Cancer Res. *7*, 32–49.

Zheng, L., Bidere, N., Staudt, D., Cubre, A., Orenstein, J., Chan, F.K., and Lenardo, M. (2006). Competitive control of independent programs of tumor necrosis factor receptor-induced cell death by TRADD and RIP1. Mol. Cell. Biol. *26*, 3505–3513.

Zhou, W., and Yuan, J. (2014a). SnapShot: Necroptosis. Cell *158*, 464-464.e1.

Zhou, W., and Yuan, J. (2014b). Necroptosis in health and diseases. Semin. Cell Dev. Biol. *35*, 14–23.

(2008). Kolmogorov–Smirnov Test. Concise Encycl. Stat. 283–287.